

NASA CR-127490

**HYPERSONIC WING TEST STRUCTURE
DESIGN, ANALYSIS, AND FABRICATION**

P. P. Plank and F. A. Penning
Martin Marietta Corporation
Denver, Colorado

CASE FILE
COPY

August 1973

Final Report

Handwritten: 8/15/73

Prepared for

NATIONAL AERONAUTICS AND SPACE ADMINISTRATION
Washington, D. C. 20546

FOREWORD

This report is submitted in accordance with the requirements of Paragraph 12.4.4 of the Statement of Work to Contract NAS4-1845.

Approved for Release by NSA on 08-25-2013 pursuant to E.O. 13526

CONTENTS

	<u>Page</u>
SUMMARY	1
INTRODUCTION	2
DESIGN CRITERIA	4
HYPERSONIC RESEARCH AIRPLANE CONCEPT AND MISSION	4
Configuration, Propulsion, and Weights	4
Vehicle Design Criteria	6
Vehicle Performance	8
STRUCTURAL CONCEPT FOR THE WING	11
AREA OF DETAILED EVALUATION --WING TEST STRUCTURE	15
STRUCTURAL DESIGN CONSTRAINTS	16
MATERIALS	17
René 41	18
TDNiCr	18
Insulation Materials	22
Minimum Gage	24
ENVIRONMENTAL ANALYSIS	25
AERODYNAMIC HEATING ANALYSIS	25
Methodology and Flow Field Model	25
Wing Heating and Fuselage Temperatures	27
VEHICLE LOAD ANALYSIS	27
WING OPTIMIZATION PROCEDURES AND RESULTS	31
GENERAL PROCEDURE	31
ASSUMPTIONS	31
ANALYSIS METHODS	32
Computer Program for Panel Optimization	32
Shear Webs	33
Spar and Rib Caps	33
Heat Shields	35

	<u>Page</u>
ANALYSIS RESULTS	37
Temperature and TPS Arrangement	37
Critical Loads and Structural Geometry	37
Effect of Spacing on Weight	46
Aeroelastic Analysis	48
Creep Analysis	50
WING TEST STRUCTURE DESIGN AND ANALYSIS	51
DESCRIPTION OF STRUCTURE	51
TEST STRUCTURE LOAD ANALYSIS	53
Finite Element Model	53
Loads Analysis	53
DETAIL DESIGN OF WING STRUCTURE	58
Beaded Panel Optimization	58
Caps	60
Webs	60
Splices	61
Heat Shields	61
Fasteners	62
TEST FIXTURE DESIGN	62
Support Test Structure	62
Tension Section	65
Ball-Ended Linkages	65
Thermal Protection	66
Vertical Load Application	66
Horizontal Load Application	66
WING STRUCTURE FABRICATION	68
GENERAL APPROACH	68
TOOLING	70
Tooling for Details	70
Subassembly Tooling	70

	<u>Page</u>
Final Assembly Tooling	76
FABRICATION OF DETAILS AND SUBASSEMBLIES	76
Beaded Panels	76
Heat Shields	79
Ribs and Spars	85
Details and Miscellaneous Subassemblies	90
FINAL ASSEMBLY	92
QUALITY ASSURANCE	102
CONCLUSIONS	103
APPENDIX A - - PANEL TESTS AND FABRICATION	105
APPENDIX B - - JOINT TESTS	125
APPENDIX C - - FORMING ORTHOTROPIC PANELS	135
APPENDIX D - - NEW TECHNOLOGY	142
REFERENCES	143 thru 145

FIGURE

1	Hypersonic Research Airplane Configuration Concept	5
2	Altitude, Mach Number, and Dynamic Pressure	9
3	Time History, Nominal Research Mission	10
4	Time History, Loads Maneuver	11
5	Time History, Launch Maneuver	13
6	Hypersonic Wing Test Structure using Beaded Panels	14
7	Effect of Temperature on Tensile Properties of René 41 in the 1033°K (1400°F) Aged Condition	19
8	Effect of Exposure at 1144°K (1600°K) on the Ultimate Tensile Strength of 0.51 to 1.27 mm (0.020 to 0.050 in.) René 41 Sheet	19
9	Effect of Temperatures on the Elastic Modulus of René 41	20
10	Effect of Temperature on the Thermal Properties of René 41	20
11	Tensile Behavior of TDNiCr	23
12	Wing Node Points for Aerodynamic Heating	26
13	Net Aerodynamic Pressures for the Total Vehicle	29

<u>FIGURE</u>		<u>Page</u>
14	Wing Test Section Limit Design Pressures	30
15	Beaded Panel Details	34
16	Configuration of Corrugated Webs	34
17	Rib Cap or Spar Cap Details with Corrugated Shear Web . .	36
18	Heat Shield Details	36
19	Primary Structure Temperatures for Beaded Panels	38
20	Heat Shield Temperatures	38
21	Fuselage Isotherms	39
22	Computer Plotted NASTRAN Model of Undeformed Structure . .	41
23	Mechanical Normal Stress Resultant in Structural Panels along BL 1.372 m (54.00 in.) for Noted Loading Conditions.	42
24	Thermal Normal Stress Resultant in Structural Panels be- tween BL 1.372 and 2.480 m (54.00 and 97.64 in.) for Noted Loading Conditions	42
25	Critical Panels for Three Design Iterations	45
26	Strength Interaction Curve for Beaded Panels for Final De- sign	47
27	Wing Weight (\bar{t}) for Final Design as a Function of Rib Spacing	47
28	Wing Weight (\bar{t}) for Final Design as a Function of Spar Spac- ing	49
29	Comparison of Airplane and Test Structure Planforms	52
30	NASTRAN Plot of Wing Test Structure, Transition Section, and Support Structure	54
31	Test Structure and Panel and Grid Point Numbers and Test Load Points	56
32	Panel Line Loads, N_y , for the Airplane and Test Structure	57
33	Strength Interaction Curve for Test Structure Panels	59
34	Design Configuration of Rib and Spar Caps	60
35	Test Structure Installation, Hypersonic Wing	63
36	Loading Points for Wing Test Structure	64
37	Manufacturing Flow, Wing Test Structure	69
38	Lower Half of Aluminum Beaded Panel Forming Die Showing Stripper Springs	71

<u>FIGURE</u>		<u>Page</u>
39	Plastic Inserts Installed to Form Different Length Beads .	71
40	EDM Graphite Electrode Tooling and Tool Mounting Plate Used to Machine Steps in René 41 Doublers	72
41	Heat Shield Forming Die Showing Machined Closeout Dimpled Corrugation Terminations	73
42	Heat Shield Forming Die with Fiberglass Inserts	73
43	Bottom and Top Half of the Web Forming Die Set in a 100- Ton Dake Press, with Formed Piece on the Lower Die	74
44	Master Weld Fixture for Rib and Spar Assemblies Shown Ready to Weld	74
45	Assortment of Chill and Backup Bars to Make Various Rib and Spar Subassemblies for Master Weld Fixture	75
46	Optical Line Tracer Template Set Up for Precision Sinewave Weld	75
47	Final Assembly Fixture Structure Looking at Station and Butt Line Jig Points of Lower Wing Surface as Viewed from the Leading Edge Outboard	77
48	Final Assembly Structure Looking at Station Plane Locators as Viewed from the Inboard Section	77
49	Manufacturing Flow for René 41 Beaded Panels	78
50	Beaded Panel Forming Die in 22-MN (5 x 10 ⁶ -lb) Press . . .	79
51	Doubler Stepped Thickness Obtained by EDM Operation . . .	80
52	Spot Welding of Doubler to Beaded Panel	80
53	Heat Shield Standoff Clips in Position on the Beaded Panel	81
54	Manufacturing Sequences to Produce Heat Shield Assemblies.	82
55	Formed Heat Shield in Forming Die	83
56	Typical René 41 Heat Shield as Aged	84
57	Completed TDNiCr Heat Shields before Oxidation Treatment .	84
58	Manufacturing Sequence of Rib and Spar Assemblies	86
59	Formed Web Used in Spar Assembly	87
60	Locating the Trimline of the Web for the Opposite Cap in in the Sinewave Weld Assembly	88
61	Open View of the Master Weld Fixture Showing the Clamping Arrangement Necessary to Fitup the Opposite Cap for Welding	88

<u>FIGURE</u>		<u>Page</u>
62	Set of Cap and Web Subassemblies	89
63	Set of Leading Edge Rib Assemblies As-Welded and Aged .	89
64	Assortment of Fasteners Used in Final Assembly	91
65	Chem-Mill Sequence of Standoff Clips	91
66	Completed Leading Edge Insulation Blanket	92
67	Final Assembly Operation	93
68	Wing Substructure After Riveting Attachment Angles Common to the Rib and Spar Assemblies	95
69	Multiple Use Drill Plate in Position with Power Air Feed Drill Used to Drill Panel Holes through the Rib and Spar Caps	95
70	Operator Installing Fasteners Through Nut Plate Strips Behind Spar Cap	96
71	Operator Drilling Mounting Holes	96
72	Bottom Side of Wing Showing Progressive Sequence of Assembly	97
73	Wing Structure Showing all Structural Beaded Panels In- stalled and Some Heat Shield Standoff Clips in Place . .	97
74	Closeup of Structural Beaded Panel Showing Tie-Straps, Heat Shield Standoff Clips, and Hat Section for the TD- NiCr Panels.	98
75	Upper Surface of the Wing Showing Heat Shields Installed and the Vertical Load Fittings	99
76	Lower Surface of the Leading Edge Outboard	99
77	Overall View of Wing Test Structure Attached To Support Test Fixture at FRC	100
78	Vertical Loading Devices	100
79	Cross Section of Wing and Support Structure	101
80	Detail View of Support Test Structure, Water-Cooled Attach- ment Fittings, and Wing Transition Section	101

<u>TABLE</u>		
I	WEIGHT SUMMARY OF HYPERSONIC RESEARCH AIRPLANE CONCEPT .	7
II	CREEP TEST RESULTS OF TDNiCr	21
III	CHARACTERISTICS OF INSULATION MATERIALS	24

<u>TABLE</u>		<u>Page</u>
IV	MINIMUM GAGE SELECTION	24
V	LOAD CONDITIONS	28
VI	ULTIMATE DESIGN LOADS AND THICKNESSES	44
VII	CONFIGURATIONS OF BEADED PANELS FOR FINAL DESIGN	45
VIII	ULTIMATE LOADS AND MARGINS OF SAFETY OF COMPRESSION BEADED PANELS FOR COMBINED MECHANICAL AND THERMAL LOADS, 2.5-g MANEUVER	59

FINAL REPORT

HYPERSONIC WING TEST STRUCTURE

DESIGN, ANALYSIS, AND EVALUATION

By P. P. Plank and F. A. Penning

Martin Marietta Corporation
Denver, Colorado

SUMMARY

An investigation was conducted to provide the analyses, data, and hardware required to experimentally validate the beaded panel concept and demonstrate its usefulness as a basis for design of a Hypersonic Research Airplane (HRA) wing.

Combinations of the beaded panel structure, heat shields, channel caps, and corrugated webs for ribs and spars were analyzed for the wing of a specified HRA to operate at Mach 8 with a life-span of 150 flights. Detailed analyses were conducted in accordance with established design criteria and included aerodynamic heating and load predictions, transient structural thermal calculations, extensive NASTRAN computer modeling, and structural optimization.

After geometry was established for the total wing, part of the wing, 7.9 m^2 (85 ft^2), was designed, fabricated, and assembled into a test structure to be used for experimentally verifying the structural adequacy of the beaded panel design concept. The super-alloy René 41 was used for the primary structure and most of the heat shields; dispersion-strengthened TDNiCr was used for the lower surface heat shields outboard of the 30% chord line [temperatures above 1255°K (1800°F)].

Optimum beaded panel tests at 922°K (1200°F) were performed to verify panel performance. Close agreement of predicted and actual critical loads permitted use of design procedures and equations for the beaded panel concept without modification.

Joint tests were performed and included cap shear and compression, panel fasteners to spar and rib caps, heat shield clips, web-to-web connections, and tensile stresses across the cap welds.

On completion, the wing test structure and associated loading fixture were delivered to NASA Flight Research Center for test.

INTRODUCTION

A large number of structural concepts for hypersonic aircraft has evolved from NASA-related studies in recent years. Specifically, a study contract that evaluated a number of wing-structural concepts for application to a Mach 8 Hypersonic Cruise Vehicle (ref. 1) was completed during 1970 for the NASA Langley Research Center; the study selected the spanwise-stiffened beaded semimonocoque wing-box panel as the best concept based on least total system cost.

Additional work was necessary to demonstrate this concept. The effort, being reported now, generated the data and hardware required to experimentally validate the beaded panel concept and demonstrate its usefulness as a basis for design of the Hypersonic Research Airplane (HRA) wing. The hypersonic wing test structure and the compatible test fixture developed during this effort will be used as a basis for a NASA-conducted program to develop a flight-loads measurement system prototype. This will include:

- 1) Design evaluation by comparing experimental to analytical (NASTRAN) data;
- 2) Flight conditions measurement system to evaluate
 - a) Flight-loads instrumentation,
 - b) Temperature calibration and simulation;
- 3) Structural concept evaluation by tests simulating design conditions.

The following steps using the beaded skin panel concept comprised the investigation: (1) the load and temperature environment was determined for the specified HRA mission; (2) the wing structural configuration was optimized to least weight; (3) a wing test structure representative of this optimum configuration was designed and constructed; and (4) a fixture was designed and

constructed to support the wing test structure during tests at the NASA Flight Research Center to its calculated flight-loading and temperature environment.

Only the most significant results of the study are presented in this report. The details of analyses, fabrication, and substantiation of results were provided as detailed task reports.

Contributors to this final report and to the Hypersonic Wing Test Structure Evaluation program are acknowledged:

Trajectory Analysis	J. L. Isaacs
Materials	C. F. Fiftal L. W. Loechel
Aerodynamic Heating	O. M. Hanner
Thermal Analysis	D. G. Herbener
Aerodynamic Loads	T. Hughes
Aeroelastic Analysis	J. R. Baratono
Structural Analysis	H. H. Hotchkiss Dr. D. H. Seitz
Structural Design	R. L. Gaide
Testing	G. G. Brun H. L. Draper W. E. Jones
Fabrication	N. L. Arbon L. S. Dabkowski M. D. Howard M. W. Meyer A. E. Muhl W. A. Ramer E. J. Rupert G. E. Uhland T. E. Young

DESIGN CRITERIA

Requirements for the analysis of the structure for the wing of a specified Hypersonic Research Airplane (HRA) are defined in this section in terms of vehicle configuration, vehicle performance, structural criteria, area of detailed evaluation, and materials.

HYPERSONIC RESEARCH AIRPLANE CONCEPT AND MISSION

Configuration, Propulsion, and Weights

The configuration of the HRA concept, as generated by NASA-FRC and shown in figure 1, is a single-place design with horizontal takeoff and landing capability. The airplane, designed for Mach 8 flight, is 30.8 m (101 ft) long, has a wing span of 11.6 m (38 ft) and is a discrete wing-body with a single vertical tail. It has an estimated gross weight of 32 923 kg (72 582 lb).

The fuselage is basically circular in cross section, with semimonocoque primary structure, and is insulated. Two lower corner areas are added for wing attachment, to provide a flat lower surface, to increase fuselage volume, and to provide a longitudinal carrythrough area. All fuel tanks are nonintegral. The forward tank is the larger tank and contains liquid hydrogen. The aft tank contains hydrocarbon fuel.

The wing and vertical tail are the hot, radiating-type structure fabricated primarily from superalloys. The wing is a low-mounted clipped double delta design with leading edge sweep angles of 85 and 70°. The forward strake delta extends from FS 6.401 to 17.678 m (252 to 696 in.) with wing carrythrough structure aft of FS 15.240 m (600 in.). The aft basic delta wing extends from FS 17.678 m (696 in.) to the wing trailing edge. The basic delta is a symmetrical 30/70 Hex (modified) air foil section, 4% thick with a leading edge radius of 1.905 cm (0.75 in.). The wing carrythrough structure extends under all of the basic wing and is located below the fuel tanks. Total wing planform area, extending from FS 6.401 m (252 in.) to the trailing edge, is estimated to be 145.6 sq m (1567 sq ft).

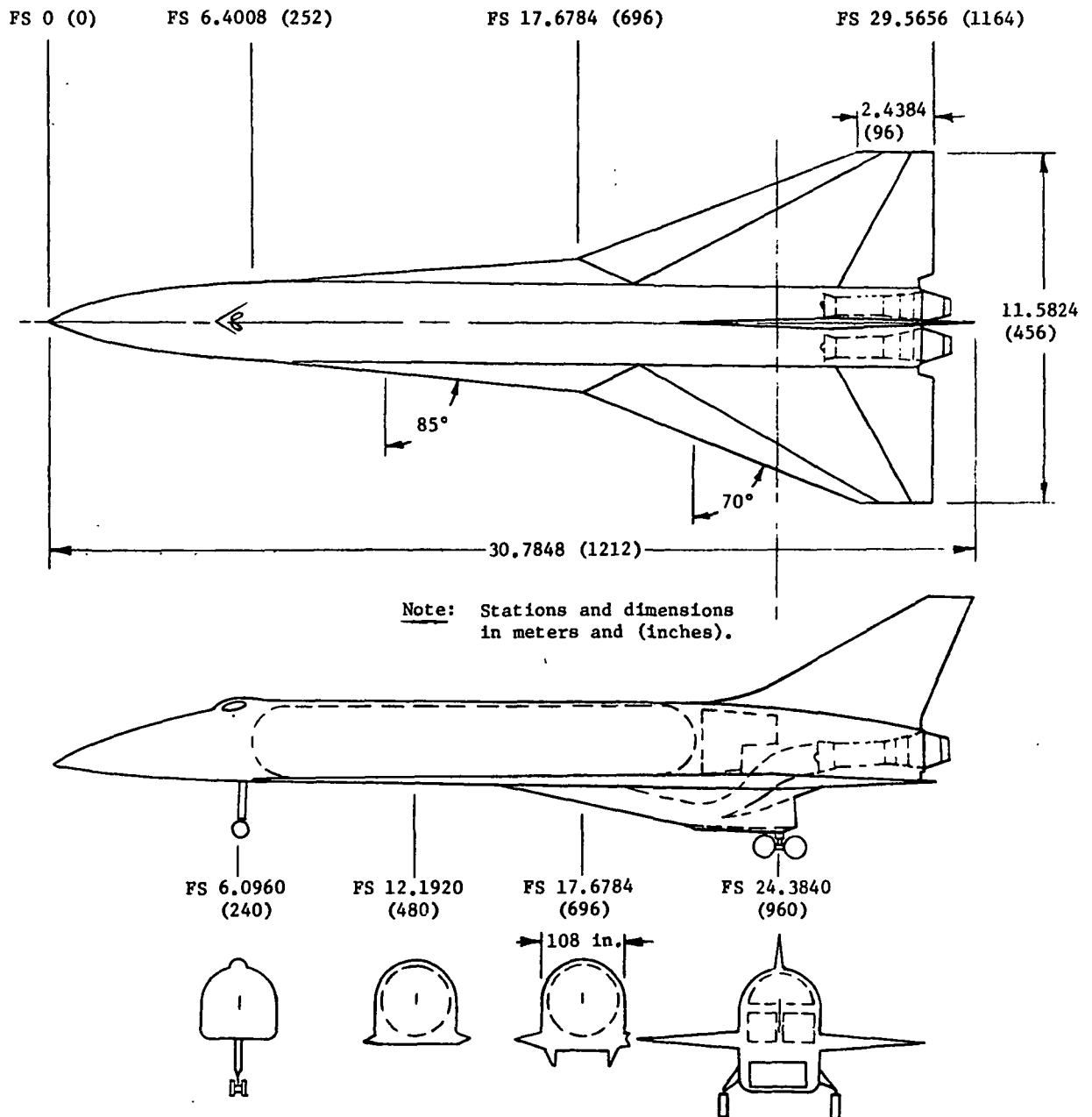


Figure 1 Hypersonic Research Airplane Configuration Concept

For this study, the wing design does not include any twist, angle of incidence, or dihedral.

The main landing gear is attached and stowed below the wing plane and outboard of the inlet/ramjet components. Items beyond the scope of this work are the special considerations required for landing gear, engine module, etc.

The propulsion system comprises separate turbofanjets and ramjets with a common two-dimensional inlet. The two turbofanjets, located in the aft fuselage bay, operate on hydrocarbon fuel from Mach 0 to 2.8. Two hydrogen burning ramjets, located beneath the center wing section, operate from Mach 0.8 to 8.0. The inlet is a mixed compression, fixed capture area design with variable ramp geometry. Actuators for the variable ramps and inlet ducting for the turbofanjets extend into or through the center wing section.

A weight summary for this HRA concept is given in table I. Incremental component weights are shown in the left-hand weight column, subtotals are shown in the center column. Appropriate percentages of total weight are shown in the right-hand column. The wing, estimated to weigh 4843 kg (10 677 lb), includes the basic delta wing, control surfaces, carrythrough structure, and the forward strake delta wing.

Component weights are proportioned in accordance with the concept configuration. Aerodynamic center positions are estimated in sufficient depth to provide a representative wing loading for analysis.

Vehicle Design Criteria

Service life of the wing of the HRA concept will be 100 flight hours, based on 150 total flights per airplane, and will include the following flights:

- 1) 110 flights with five minutes cruise at Mach 8 (nominal research mission);
- 2) 30 flights with a -0.5-g pushover, 2.5-g pullup loads maneuver at Mach 8 (design condition);
- 3) 10 flights with a Mach 8, 2-g launch maneuver (design condition).

TABLE I
WEIGHT SUMMARY OF HYPERSONIC RESEARCH AIRPLANE CONCEPT

Component	Weight, kg (lb)			Percent weight
	Unit	Component	Total	
Structure		13 072.5 (28 820)		39.7
Fuselage	3 606.1 (7 950)			
Wing + elevons	4 843.0 (10 677)			
Vertical tail	563.4 (1 242)			
Landing gear	1 584.4 (3 493)			
Fuel tanks + insulation	1 341.7 (2 958)			
Thermal protection system	1 134.0 (2 500)			
Propulsion		6 350.3 (14 000)		19.3
Turbofan jets (2)	2 721.6 (6 000)			
Inlet + diffuser	2 721.6 (6 000)			
Convertible scramjet	907.2 (2 000)			
Subsystems, miscellaneous components		2 886.2 (6 363)		8.8
Research instrumentation		635.0 (1 400)		1.9
Empty weight			22 944.0 (50 583)	69.7
Pilot		104.3 (230)		0.3
Propellant		9 874.3 (21 769)		30.0
JP residuals	155.1 (342)			
Taxi (2 minutes)	18.1 (40)			
Run up (1 minute)	522.5 (1 152)			
LH ₂ residuals	140.2 (309)			
LH ₂ boiloff	38.1 (84)			
JP mission fuel	4 477.4 (9 871)			
LH ₂ mission fuel	4 522.7 (9 971)			
Pilot and propellant			9 978.6 (21 999)	30.3
Total weight			32 922.6 (72 582)	100.0

The design limit load factors for design purposes are:

- 1) Normal acceleration = 2.5 to -1.0 g;
- 2) Longitudinal acceleration = 1.0 to -2.0 g;
- 3) Lateral acceleration = +0.5 g.

The maximum design dynamic pressure shall not exceed 83.79 kN/m² (1750 psf).

The aircraft shall not exceed a maximum angle of attack of 12° nor a minimum angle of attack of -2°.

Vehicle Performance

A nominal research mission profile is shown by the solid lines in figure 2. This profile consists of a horizontal takeoff at 103 m/sec (200 knots), a subsonic climb to a 73.2-km (24 000-ft) transonic altitude, and an acceleration at a constant 47.88 kN/m² (1000 psf) dynamic pressure along the profile shown to Mach 8 at an altitude of 30.8 km (101 000 ft) indicated by Point A. Five minutes cruise flight is performed at Mach 8 at altitudes of 30.8 to 35.4 km (101 000 to 116 000 ft). Descent is accomplished along a constant 23.94 kN/m² (500 psf) dynamic pressure profile. A time history for this nominal research flight is shown in figure 3.

Wing design includes a pushover-pullup loads maneuver as shown by the dashed line profile in figure 2, from Points A to C. This maneuver requires a 3-minute transition maneuver performed from the initial cruise condition to the initial loads maneuver condition. This transition maneuver is performed in such a way that it is not a design condition, and the aircraft has obtained radiation equilibrium temperatures before performing the loads maneuver. The loads maneuver consists of a -0.5-g pushover and 2.5-g pullup so that the maximum dynamic pressure during the maneuver meets the vehicle's 83.79-kN/m² (1750-psf) dynamic pressure design condition. At the completion of the loads maneuver, the vehicle is decelerated in level flight for 6 minutes to intercept the nominal descent trajectory at Mach 5.3. This point of interception is Point C in figures 2 through 4.

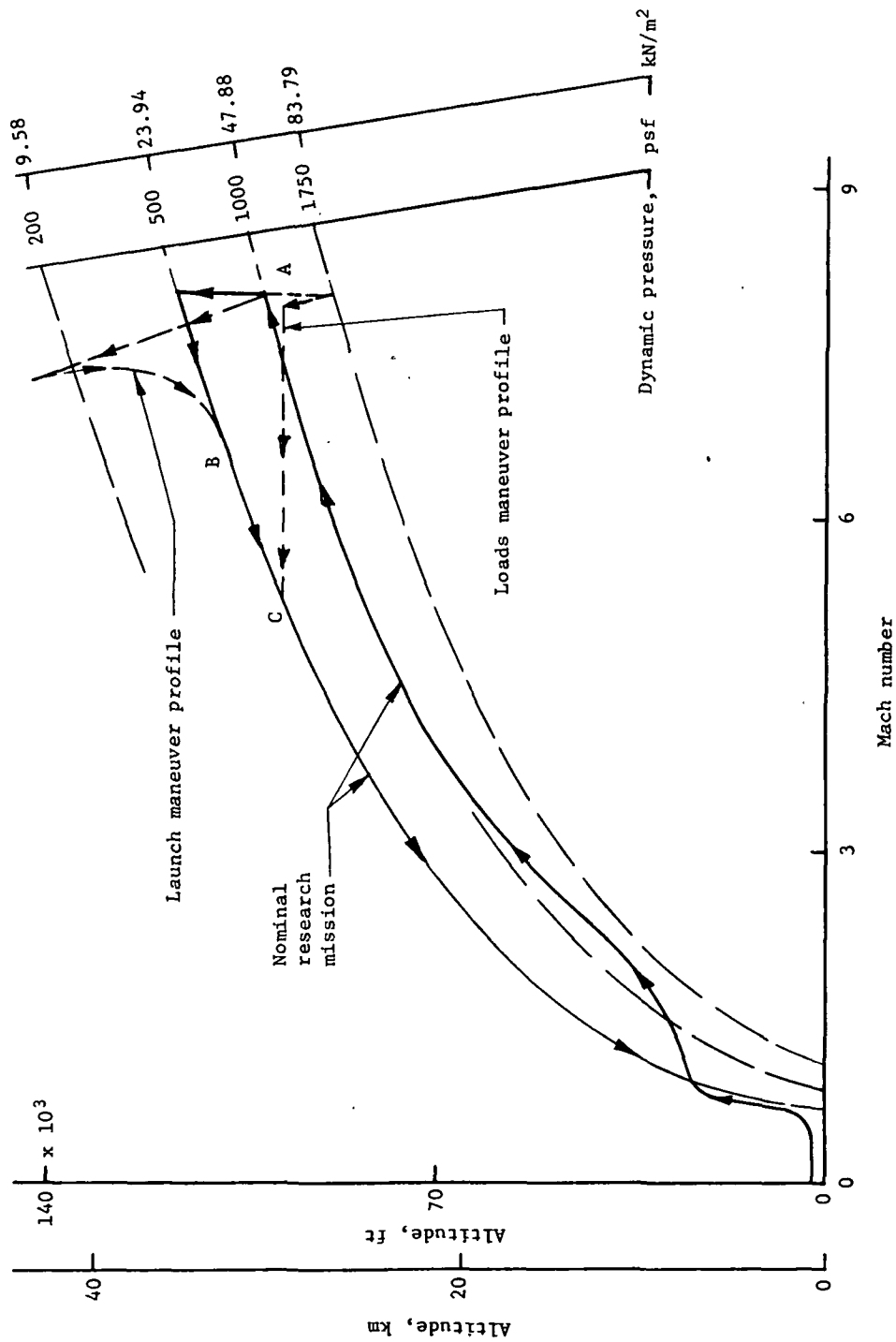
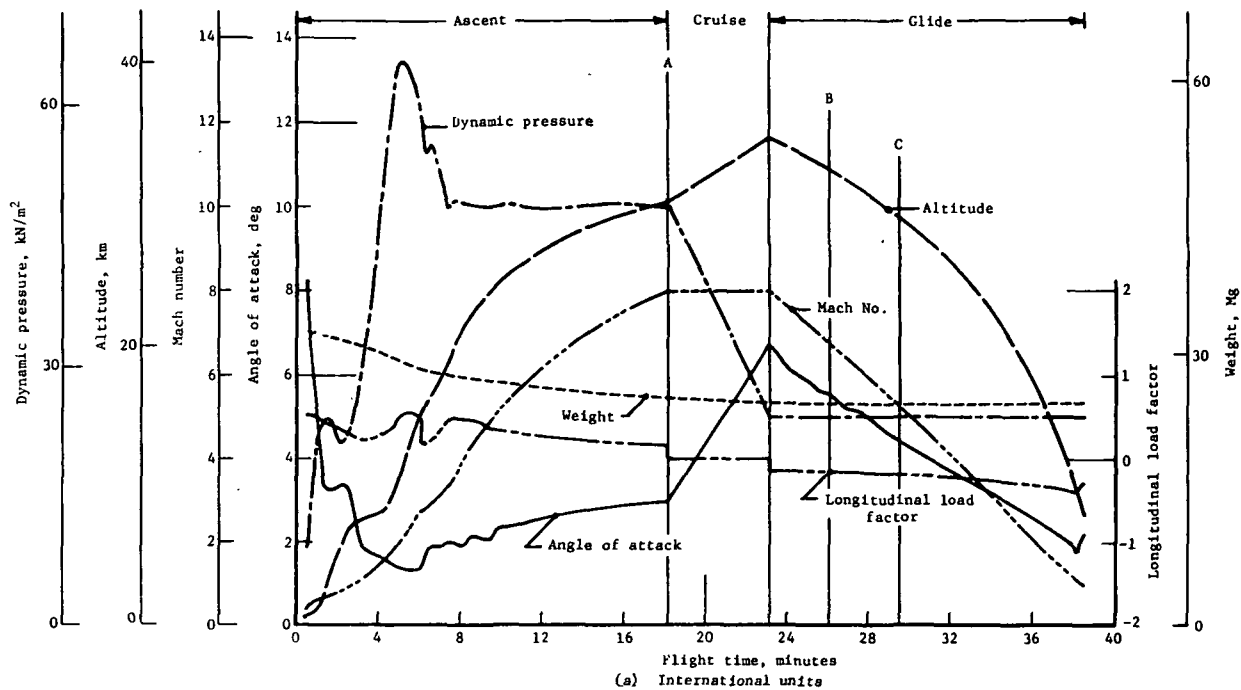


Figure 2 Altitude, Mach Number, and Dynamic Pressure

Legend:

- A Transition maneuver start point (from nominal ascent to loads or launch maneuvers)
- B Glide slope return point for launch maneuver (time from ground = 23.33 minutes)
- C Glide slope return point for loads maneuver (time from ground = 27.7 minutes)



Legend:

- A Transition maneuver start point (from nominal ascent to loads or launch maneuvers)
- B Glide slope return point for launch maneuver (time from ground = 23.33 minutes)
- C Glide slope return point for loads maneuver (time from ground = 27.7 minutes)

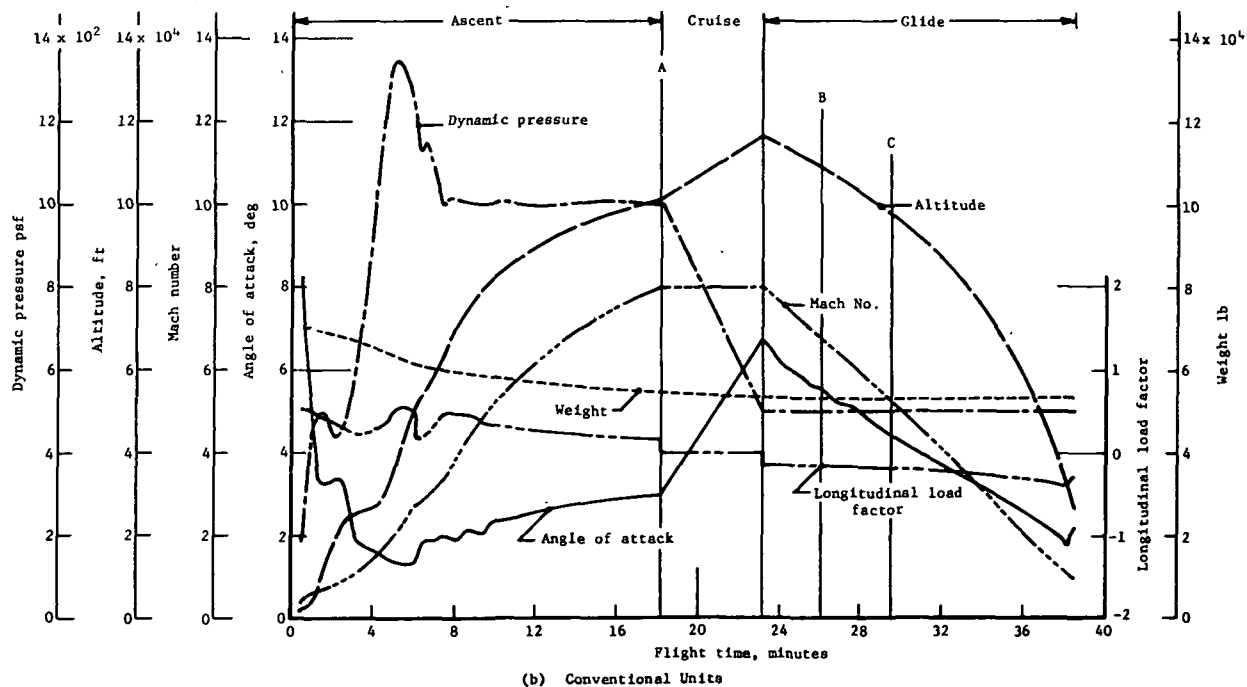
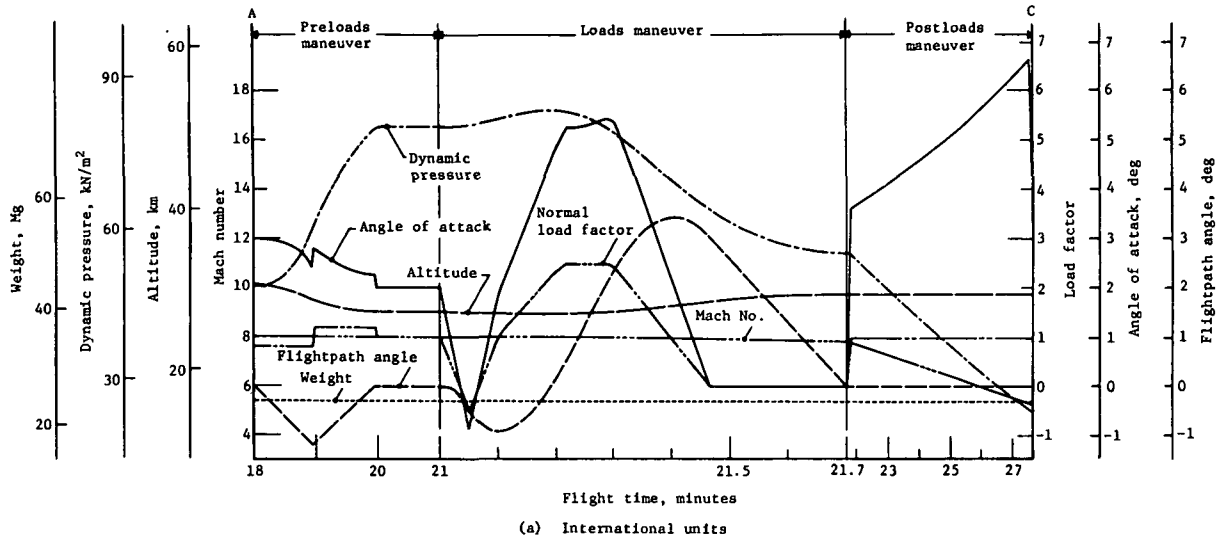


Figure 3 Time History, Nominal Research Mission

Legend:

- A Transition maneuver start point (from nominal ascent to loads or launch maneuvers)
C Glide slope return point for loads maneuver (time from ground = 27.7 minutes)



Legend:

- A Transition maneuver start point (from nominal ascent to loads or launch maneuvers)
C Glide slope return point for loads maneuver (time from ground = 27.7 minutes)

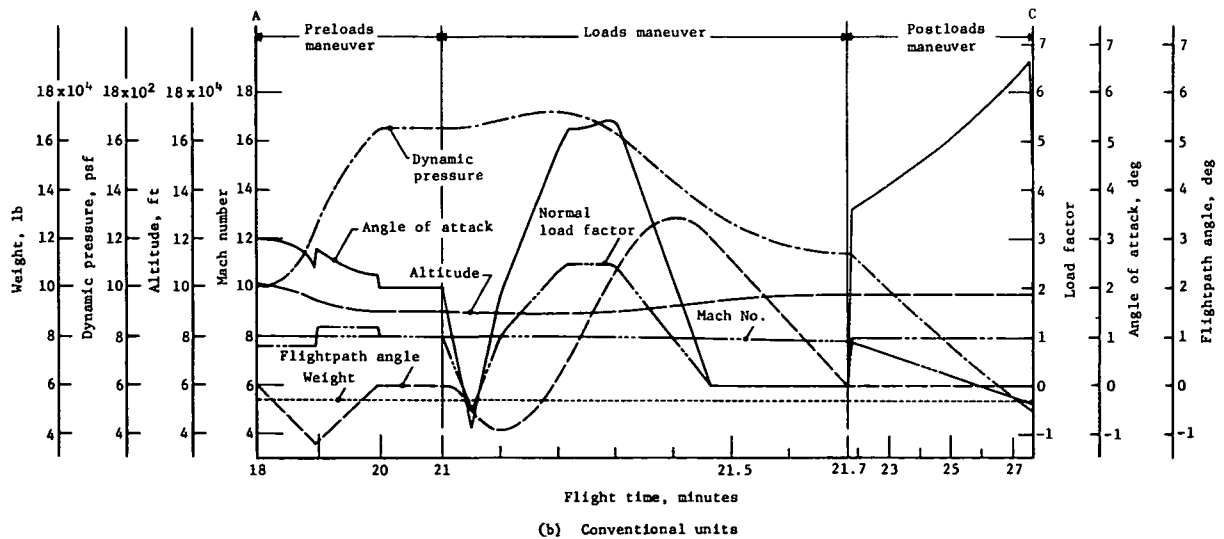


Figure 4 Time History, Loads Maneuver

A typical launch maneuver for one flight in 15 for a parallel staged vehicle is shown by dashed lines in figure 2 and is considered in the wing design. This maneuver, initiated at an altitude of 30.8 km (101 000 ft) and Mach 8, includes a 2-minute prelaunch launch maneuver starting at Point A of figures 2, 3, and 5. After the 2 minutes, the aircraft does a pullup limited to a normal load factor of 2 g and a maximum angle of attack of 12° . The aircraft then coasts to an altitude of 43.3 km (142 000 ft), and achieves an equilibrium glide at Mach 6.75 on the nominal research mission descent profile shown by Point B of figures 2, 3, and 5. The time history for this launch maneuver is shown in figure 5.

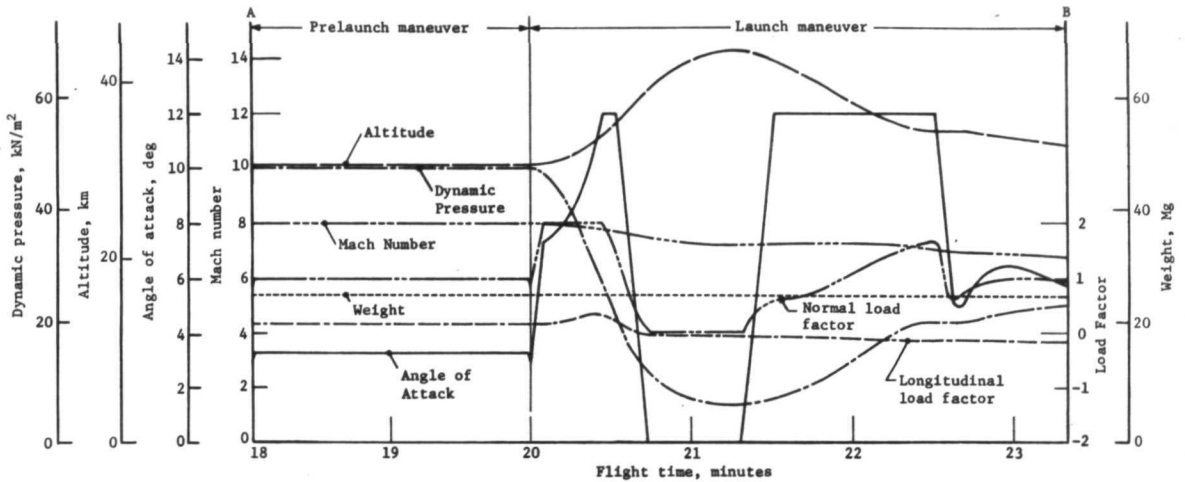
STRUCTURAL CONCEPT FOR THE WING

Previous studies of structural concepts applicable to hypersonic airplanes have demonstrated the feasibility of an all-metallic structure of superalloys. A related NASA-sponsored study (refs. 1 and 2) selected spanwise-stiffened beaded panels for the wing of a Mach 8 cruise vehicle as the best concept based on least total system cost. An orthogonal wing box structure having spars normal to the vehicle centerline incorporating beaded panels is shown in figure 6. Spanwise stiffened beaded panels are covered by chordwise beaded heat shields. The heat shields, a nonablative thermal protection system, decrease in-plane wing temperature gradients and thermal stress for minimum weight. Insulation is used as required to limit structural member temperatures, and to prevent excessive thermal stresses. Ribs and spars have corrugated webs welded to upper and lower caps.

In detail, the spanwise-stiffened semimonocoque beaded panel concept consists of a series of adjacent up and down circular arc corrugations. The beads are terminated to a flat end compatible with the rib attachments by decreasing the bead radius so the bead-flat intersection describes an ellipse. End closures are added to stiffen the flat ends sufficiently to prevent local crippling at the bead ends.

Legend:

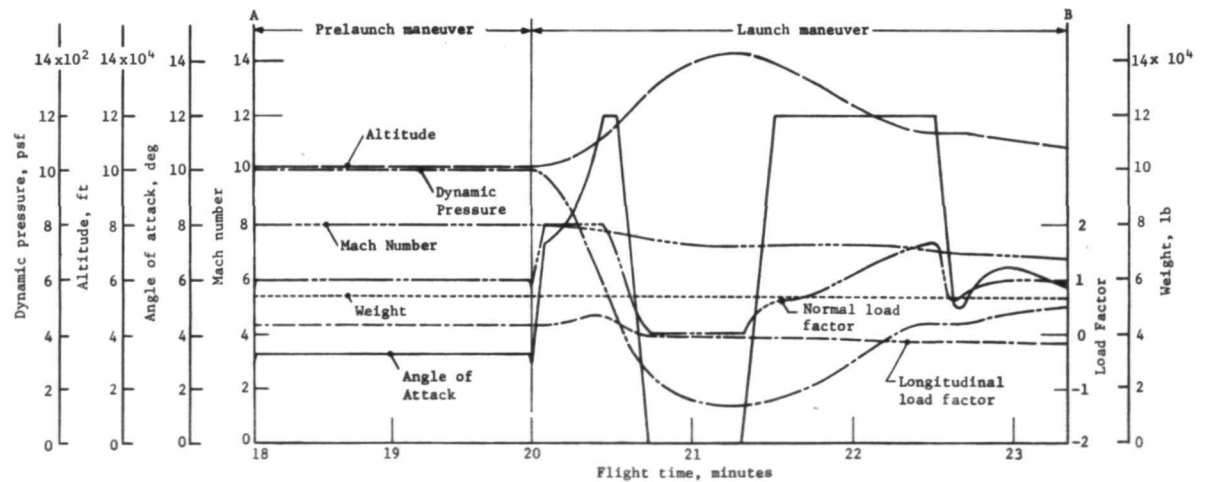
- A Transition maneuver start point (from nominal ascent to loads or launch maneuvers)
 B Glide slope return point for launch maneuver (time from ground = 23.33 minutes)



(a) International units

Legend:

- A Transition maneuver start point (from nominal ascent to loads or launch maneuvers)
 B Glide slope return point for launch maneuver (time from ground = 23.33 minutes)



(b) Conventional units

Figure 5 History, Launch Maneuver

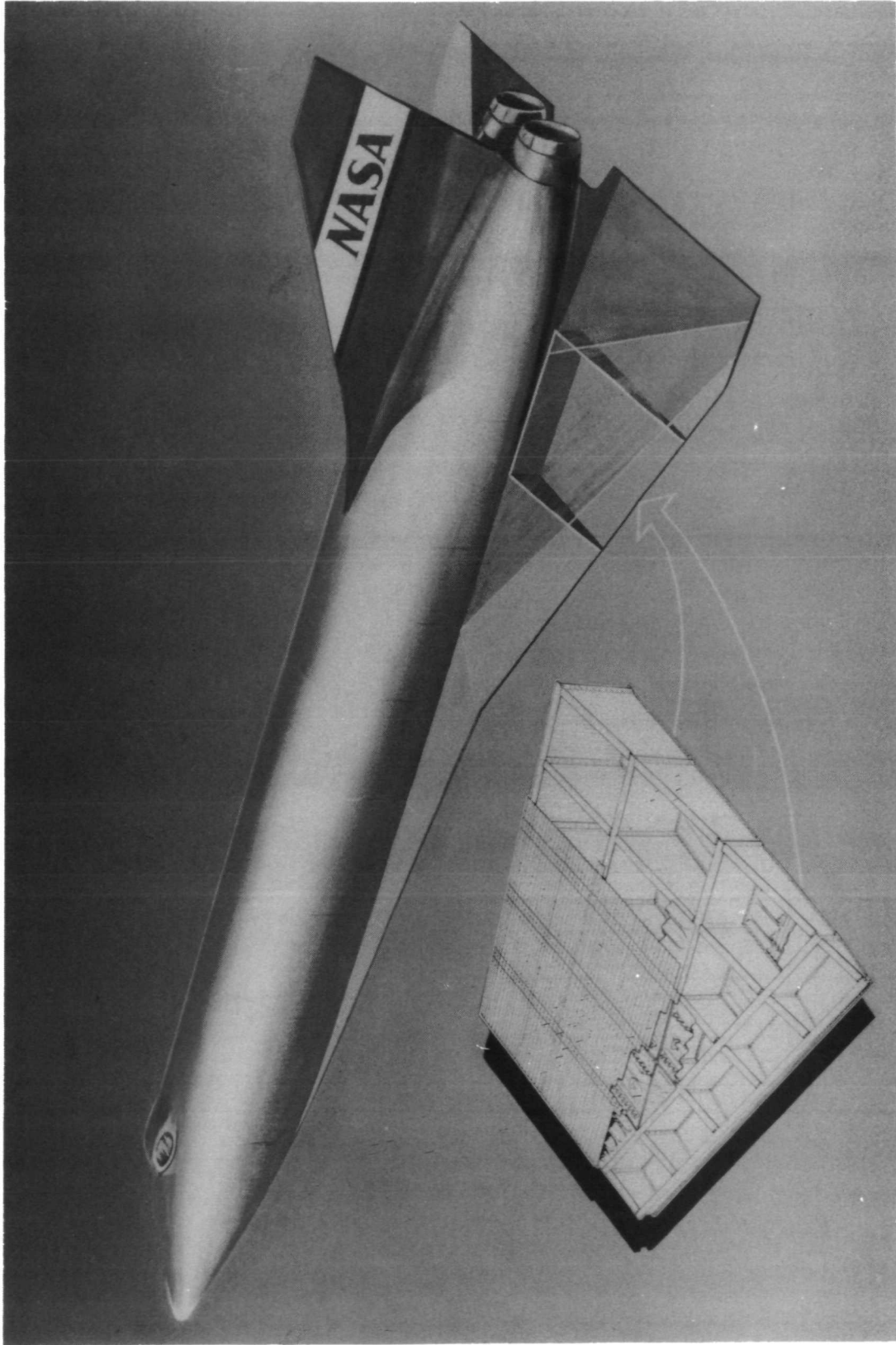


Figure 6 Hypersonic Wing Test Structure using Beaded Panels

AREA OF DETAILED EVALUATION--WING TEST STRUCTURE

The portion of the wing for which the detailed analysis and design and fabrication tasks were performed is centered on FS 24.384 m (960 in.) of figure 1 and was specified to cover a minimum planform area of 7.9 sq m (85 sq ft). This area is representative of the wing primary structure as well as the thermal protection system of heat shield panels and insulation. The test structure was constructed to represent this area. The rib and spar spacing for the entire wing and, therefore, the test structure was uniform and orthogonal with ribs parallel to the aircraft centerline. Airfoil thickness defines the plane of the heat shield panels.

Five bays of panels (six spars) were specified in the chordwise direction to cover the 7.9 sq m (85 sq ft), resulting in a spar spacing of 50.8 cm (20 in.). The structure spans from the fuselage attachments to the wing leading-edge spar, but does not contain the leading edge. The number of panels in the spanwise direction depends on rib spacing exclusive of leading edge close-outs.

Upper and lower surfaces of the wing are covered by structural panels for each wing box. A wing box is the volume enclosed by adjacent ribs and spars. These panels were identical except for the following:

- 1) Panels with minor geometrical differences due to changes in wing depth;
- 2) Panels located along lines of wing surface discontinuities;
- 3) Panels unique to a particular location such as areas adjacent to the leading edge.

The panel optimization, rib and spar design, and heat shield selection were based on least total wing weight for the critical panel location. The entire wing and all the fuselage were used in the analysis to determine mechanical and thermal stresses. Least weight was found by converging on the lightest, adequate design using the method of analyzing successive redesigns.

STRUCTURAL DESIGN CONSTRAINTS

The test structure was designed using a hot-wing with a nonintegral tank fuselage; the wing carrythrough structure is continuous under the fuselage, but detachable at the wing fuselage intersection. It does not include the irregularities of an actual vehicle that are difficult to accurately analyze. The design neither makes specific provisions for the landing gear or engine module attachment nor accounts for local heating effects caused by these components. However, the control system forces required to accomplish the maneuvers are included as load distributions along the trailing edges. Drag augmentation and high-lift devices were not considered.

The load and launch maneuvers in combination with the baseline trajectory were used to determine limit loads due to pressure, inertia, and thermal effects.

The HRA wing test specimen was designed for 150 flights. All flights include the baseline trajectory, and 30 of the 150 flights include a load maneuver and 10 other flights include a launch maneuver.

The leading edges of the HRA wing test specimen were neither designed nor constructed for this effort. They were assumed to be segmented, 3.8-cm (1.5-in.) diameter, and constructed of a material that would not require replacement more than once for each 10 flights. Loads caused by the leading edges were included in the design analysis, and, although no leading edges were constructed or tested, provisions for applying these loads to the test structure were included in both the design and the hardware.

The test structure (including heat shields) was designed for the life of the vehicle, and therefore, requires no refurbishment. However, all panels were designed detachable; this allows them to be replaced in case of damage and provides access to all areas of the structure for instrumentation installation.

For design purposes, the wing cavity was assumed to be vented to the upper surface so the internal pressure lag was equal to, but did not exceed 3.45 kN/m^2 (0.5 psi) during any of the maneuvers.

Limit load was defined as 1.3 times the sum of loads incurred during the load or launch maneuver, whichever was greater, and the thermal stress calculated for this condition. Temperatures used in the stress analysis were those calculated for that maneuver. A 1.5 factor of safety was used to determine ultimate loads from the design limit loads.

Material design-limit stresses were temperature dependent and were restricted to 0.2% yield or 2/3 of ultimate strength, whichever was least.

Compression members with material properties corrected for local temperatures were designed to prevent instability in all modes for all load conditions including thermal stress. Beaded panels were designed for elastic buckling with any local buckling occurring at loads at least 10 percent greater than for overall stability.

A permanent deformation of 0.5% due to creep was considered to be the life of the vehicle.

The heat shields of the thermal protection system were designed for a flutter factor of safety of 1.3 on dynamic pressure at all times and for all trajectories.

The criterion for boundary-layer noise was $0.007q$, where q is dynamic pressure, except for areas that are subject to shock impingement and/or other flow irregularities that cause excess noise; the criterion for the latter areas was $0.022q$.

MATERIALS

The basic material for the wing structure and heat shields was René 41. TDNiCr was used for heat shields in areas adjacent to the low surface leading edges as required by René 41 temperature limits [above 1255°K (1800°F)]. All other material components (e.g., brackets, fasteners) were made compatible with these basic materials.

René 41

René 41 can be used in two separate heat-treated conditions, both of which consist of a solution treatment followed by an age. The 1033°K (1400°F) aged condition has the higher ambient temperature strengths and also higher elevated temperature creep and tensile strengths than has the 1172°K (1650°F) aged condition to about 1033°K (1400°F). When used above 1033°K (1400°F) for long times, the 1172°K (1650°F) aged condition overages, and losses in strength occur. However, short-time exposures, on the order of 1/2 hr or less, can be made to temperatures above 1033°K (1400°F) without incurring significant strength losses.

The structural panels do not exceed 1061°K (1450°F) (as shown by the isotherms for the 2.5-g maneuver) and total exposure times at this temperature are less than 1/2 hr. The 1033°K (1400°F) aged condition is not degraded in this environment. The cruise mode represents approximately 10 hr of operation at 1033°K (1400°F) and does not produce significant property degradation to the 1033°K (1400°F) aged condition. The 1033°K (1400°F) aged condition was selected because the thermal environment permitted use of this more advantageous heat treat.

For the heat shields, an exposure of 1255°K (1800°F) for 1/2 hr during 2.5-g maneuver, and 1172°K (1600°F) for approximately 10 hr during cruise is experienced. A 10% reduction in properties results for 10 hr exposure at 1144°K (1600°F).

Design properties of René 41 in the 1033°K (1400°F) aged condition used for structural and thermal analyses are shown in figures 7 through 10, in which F_{tu} is the ultimate tensile strength, F_{ty} is the tensile yield stress, C is the thermal capacity, α is the coefficient of thermal expansion, and k is the coefficient of thermal conductivity.

TDNiCr

A limited test evaluation of TDNiCr was conducted to establish criteria for allowable creep deformation. The material evaluated was supplied by NASA-Lewis and was part of the 1972 NASA sheet rolling program. The material was 0.025 cm (0.010 in.) thick from heat number 3711 (Fansteel) and consisted of various small-size sheets, which requiring splicing them to make a heat shield.

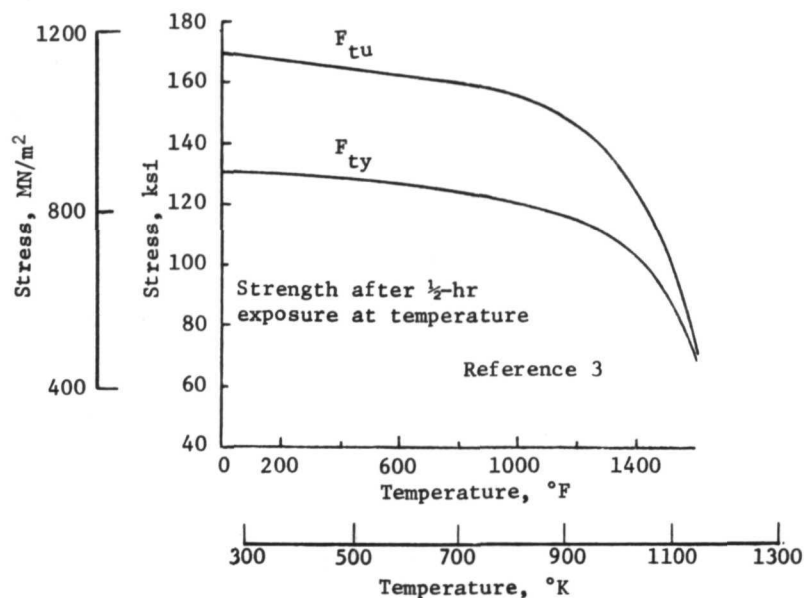


Figure 7 Effect of Temperature on Tensile Properties of René 41 in the 1033°K (1400°F) Aged Condition

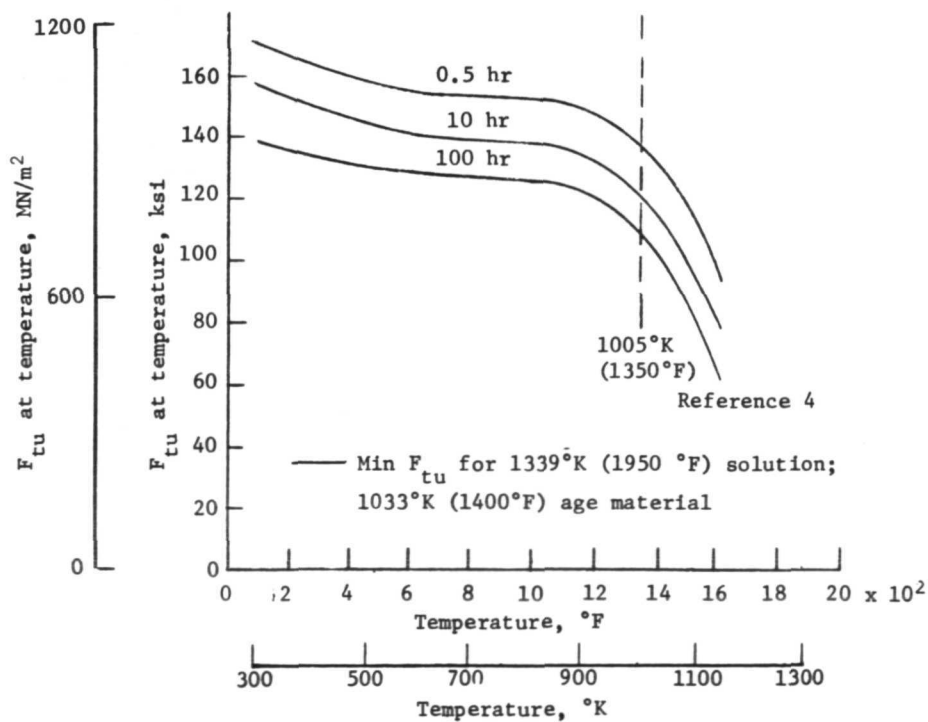


Figure 8 Effect of Exposure at 1144°K (1600°F) on the Ultimate Tensile Strength of 0.51 to 1.27 mm (0.020 to 0.050 in.) René 41 Sheet

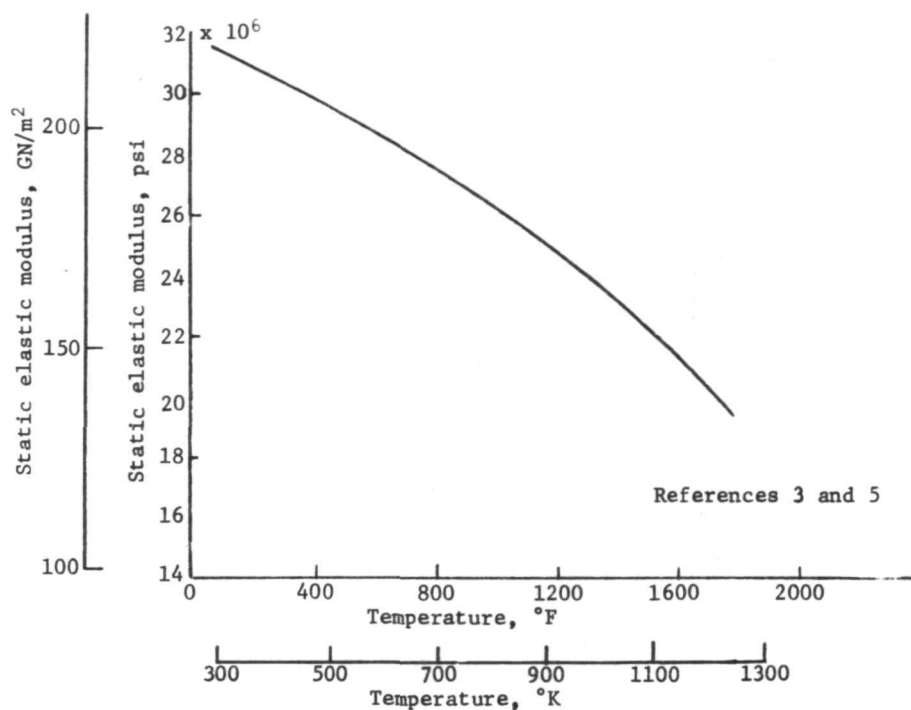


Figure 9 Effect of Temperatures on the Elastic Modulus of René 41

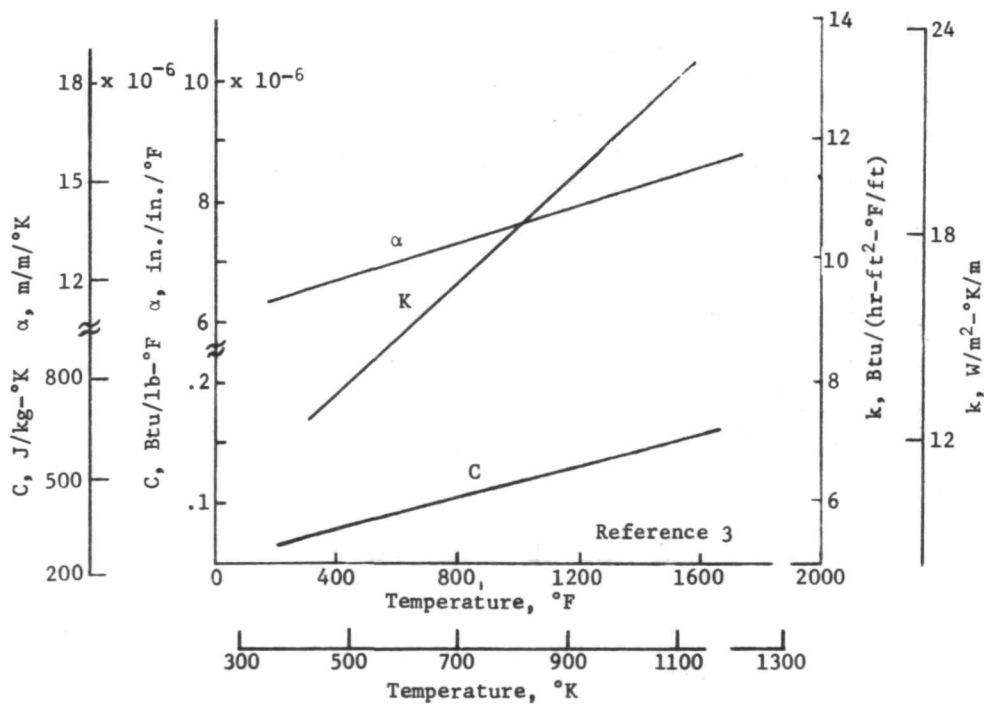


Figure 10 Effect of Temperature on the Thermal Properties of René 41

The original program was to subject specimens to creep deformations on the order of 0.2% strain at 1255°K (1800°F) and determine the tensile strength of the specimens as a function of temperature. By this method, allowable creep and tensile stresses can be developed.

After the first few tests, it became apparent that the erratic behavior and very low ductility of the material at elevated temperature precluded this approach to determining design allowables. Table II summarizes these tests. The first specimen tested (6) failed on loading to 55.16 MN/m² (8 ksi) at 1366°K (2000°F). This stress value is 13.79 MN/m² (2 ksi) lower than the specification minimum and 41.37 MN/m² (6 ksi) lower than the producer certified strength.

TABLE II
CREEP TEST RESULTS OF TDNiCr

Spec	Temper- ature, °K (°F)	Stress, MN/m ² (ksi)	Time, minutes	Total creep strain	RT tests	
					F _{tu} , MN/m ² (ksi)	Strain, %
6	1366 (2000)	55 (8)	Failed on loading		---	---
1	1366 (2000)	28 (4)	400	0.0002		
	1366 (2000)	41 (6)	200	0.0003		
	1366 (2000)	48 (7)	230	0.0004		
	1366 (2000)	52 (7½)	210	0.0005		
	1366 (2000)	55 (8)	Failed on loading			
2	1255) (1800)	41 (6)	690	0.0010	119.3 (17.3)	0.12
7	1255 (1800)	41 (6)	4 cycles of 30 min ea = 120	0.0012	118.6 (17.2)	0.075

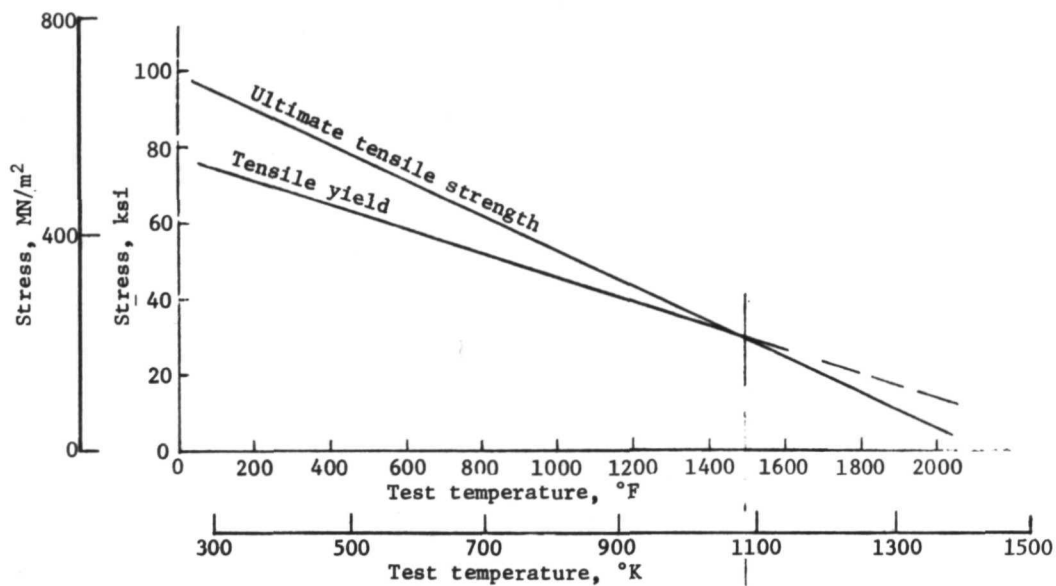
It became apparent that there was essentially no margin between the fracture strength and the stress at which negligible creep would occur [at least at 1366°K (2000°F)]. Further, it was apparent that the ductility was so low as to preclude obtaining 0.2% creep as desired.

The results of the tests on the specimens of table II clearly indicated that essentially no creep could be allowed in TDNiCr if fracture was to be prevented. Accordingly, it was determined that there was no merit in performing further creep testing and it was decided that the remaining specimens would be used to establish static strength allowables. Tensile tests were made at 294, 811, 1033, 1255, and 1366°K (70, 1000, 1400, 1800, and 2000°F).

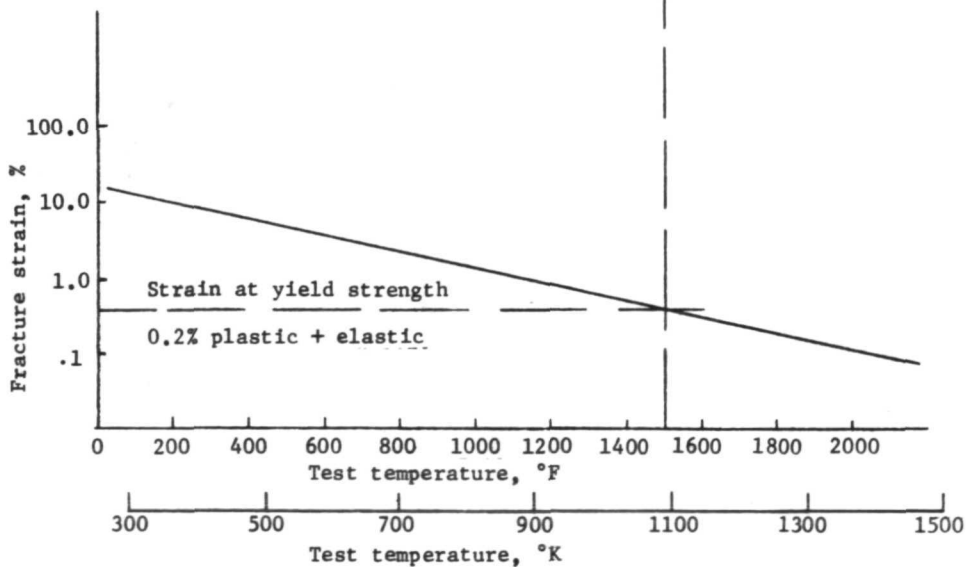
The results of these tests are shown in figure 11. In figure 11(a) it can be seen that the strength decreases with temperature as is expected and decreases by an amount typical of other test results that have been reported. This figure also shows that the yield strength and ultimate strength curves intersect at about 1089°K (1500°F). Beyond this temperature, the ductility of TDNiCr is less than the 0.2% plastic strain normally defined as the yield strength strain. Consequently, no yield strength values were obtained at 1255 or 1366°K (1800 or 2000°F). The fracture strain obtained from these tests is plotted in figure 11(b). The 0.2% strain level intersects the ductility curve at about 1089°K (1500°F). The practical significance of this low ductility is that great care must be exercised in the application of TDNiCr at elevated temperatures, particularly in regions of stress concentration if failures are to be prevented; i.e., the ductility of the material must not be exceeded, even locally. Static strength allowables for this program were obtained by using the data in figure 11(a).

Insulation Materials

Various insulation materials have been considered for insulating the wing forward of the 30% chord. Table III shows the candidate insulation material characteristics.



(a) Ultimate and yield strengths



(b) Fracture strains

Figure 11 Tensile Behavior of TDNiCr

TABLE III
CHARACTERISTICS OF INSULATION MATERIALS

Insulation	Density, kg/m ³ (lb/ft ³)	Maximum vitization temperatures, °K (°F)
Dyna Flex	96 (6)	1811 (2800)
Micro-Quartz	96 (6)	1366 (2000)
Dyna-Quartz	99 (6.2)	1783 (2750)
Min-K-2000	320 (20)	1644 (2500)

The Dyna-Quartz is brittle and, therefore, has doubtful resistance to vibration loads. Of the remaining candidates, Micro-Quartz was selected because it has the lowest $k\rho$ (thermal conductivity x density), which indicates lowest weight. Also, the Micro-Quartz is adaptable to the mechanical and thermal environment [maximum temperature of 1366°K (2000°F)]. Data are taken from reference 6.

Minimum Gage

Table IV presents minimum metallic material thicknesses that have been selected for the concepts evaluation. The basis of selection is suitability to fabrication processes and to damage resistance.

TABLE IV
MINIMUM GAGE SELECTION

Structural concept	Element	Minimum thickness, mm (in.)
Beaded panel	Skin	0.762 (0.030)
Ribs and spars		
Caps	Flanged sheet metal	0.762 (0.030)
Webs	Corrugation	0.381 (0.015)
Heat Shield	Skin	0.254 (0.010)

ENVIRONMENTAL ANALYSIS

AERODYNAMIC HEATING ANALYSIS

A thin-skin, transient aerodynamic heating analysis was conducted at selected points on the fuselage and wing heat shield for the Hypersonic Research Airplane (HRA). The analysis consisted of theoretical predictions of the nominal aerodynamic heating environment as introduced by each of the three trajectories--nominal research mission, loads maneuver, and launch maneuver. No arbitrary heating multipliers were used to increase the incident heating rates. Modifications to the external surface view factors to space were included in the analysis because of the blockage caused by the presence of the wing/fuselage/nacelle structures. A numerical analysis defining the aerodynamic heating environment was accomplished by the use of the aerodynamic heating program of reference 7.

Methodology and Flow Field Model

The methods used in the analysis were Eckert's laminar and Spalding-Chi turbulent with von Karman's expression for the Reynolds analogy factor. The general methods approach and application were according to references 8 and 9. The flow was processed through an oblique, attached shock with isentropic compression or expansion to local pressures.

The wing was assumed to have a chordwise flow field as evidenced by the streamline paths in references 10 through 13. The local flow conditions were calculated on the basis of a wedge shock and wedge pressures (ref. 14). Crossflow (streamline divergence) for a 70° swept sharp leading edge delta wing was included. Pressures on the windward side were based on the local surface angle plus the angle of attack. Pressures on lee-side surfaces were based on a Prandtl-Meyer expansion. The turn angle was limited to 7.6° maximum to prevent an overexpansion for attached flow and for correlation with flight data (refs. 15 and 16).

The fuselage flow model used conical shock with wedge pressures. Windward-side pressures were based on the local surface angle plus angle of attack. Lee-side pressures were assumed to be ambient.

Because of the vehicle geometry, flight regime, and the relatively small angles of attack (12° maximum) the following boundary layer transition criterion was used (ref. 17). Transition onset was assumed to occur at a local inviscid flow Reynolds number of 1×10^6 . A transitional flow model after Yakura and Masaaki (ref. 18) was used with a ratio of fully turbulent to onset equal to 2.0. Attempts to use the transition model of reference 9 on the wing lee-side (with Prandtl-Meyer expansion) resulted in reverse chord-wise transition as a result of the reduced local pressures and re-initiation of the flow length for momentum thickness Reynolds number determination.

A point analysis was performed at 84 locations (nodes) on the fuselage and wing heat shield surface. There were 60 nodes shown in figure 12 on the aft delta wing surface (30 bottom and 30 directly opposite on the top), four nodes on the chine (two bottom and two directly opposite on the top) and 17 nodes on the fuselage, and three nodes on the nacelle. The view factors were obtained from reference 15 for the wing upper surface and calculated by a summation of components using reference 19 for the wing lower surface and fuselage. A check, using this procedure, gave values to within ± 0.01 of those in reference 15.

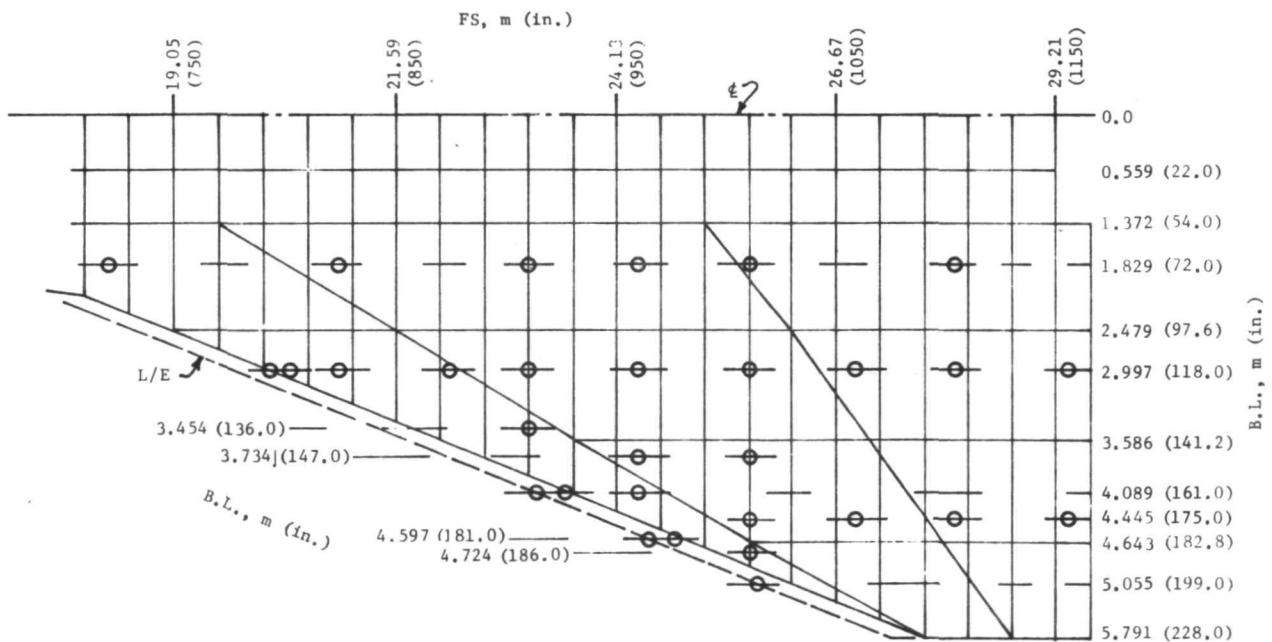


Figure 12 Wing Node Points for Aerodynamic Heating (Points Directly Above and Below Each Other)

The analysis determined radiation equilibrium temperatures for the 84 node points; an emissivity of 0.8 was used. Fuselage nodes considered an equivalent thickness of 0.064 cm (0.025 in.) René 41 to account for skin and backup structure. Wing nodes considered only the 0.031 cm (0.012 in.) René 41 heat shield.

Wing Heating and Fuselage Temperatures

The program output consisted of both printed and card punched data. The primary (and most prolific) output was the printed data consisting of node temperatures, convective heat transfer, and flow field data at specific flight time intervals. To expedite the wing internal thermal analysis, selected heat transfer data (recovery enthalpy, node temperatures, and heating rates) were card punched concurrently for input to the structural and internal radiation analysis of the wing. Radiation equilibrium temperature distributions on the fuselage, obtained from the output of the program of reference 7, are illustrated as isotherms in the wing optimization section of this report. These fuselage temperatures were used for every wing optimization iteration; however, the wing temperatures were modified with each iteration. The resulting wing isotherms for the final wing iteration are shown in the wing optimization section of this report.

Cold wall heating rates and recovery enthalpy required for internal thermal analysis were obtained from the punched output. For a particular trajectory, the recovery enthalpy curves were essentially the same for all the nodes on the wing. Cold wall heating rates, however, required individual curves for each node depending on the onset of turbulence.

VEHICLE LOAD ANALYSIS

Unit load distributions were derived for the four conditions specified in table V and include inertia, thrust, elevon, and aerodynamic loading. In addition, normal and axial balance were determined with the resultant thrust vector running approximately through the vehicle center of gravity. Rigid load analyses were conducted for the four conditions of table V.

TABLE V
LOAD CONDITIONS

Flight parameter	Flight condition			
	Loads maneuver		Cruise 1.0 g	Launch maneuver 2.0 g
	Pushover -0.5 g	Pullout 2.5 g		
Normal load factor, g	-0.5	2.5	1.0	2.0
Axial load factors, g	0	0	0	0.23
Angle of attack, deg	-0.90	5.35	4.85	8.50
Mach	8	8	8	8
Dynamic pressure, kN/m ² (psf)	79.48 (1660)	84.27 (1670)	35.91 (750)	40.70 (850)
Altitude, km (ft)	27.43 (90 000)	27.43 (90 000)	33.19 (108 500)	31.70 (104 000)
Gross weight, kg (lb)	24 500 (54 000)	24 500 (54 000)	24 500 (54 000)	24 500 (54 000)

Net pressure loadings for the total vehicle are shown in figure 13. Limit design panel pressures on the wing test structure area are presented in figure 14 for the four design conditions. Design of the panels was governed by the most critical combination of pressures. Ultimate pressure is 1.5 times limit design pressure. The wing cavity was assumed to be vented to the upper surface so that the internal pressure lag is equal to, but does not exceed 3.45 kN/m² (0.5 psi) during any of the maneuvers. In addition, lower surface TPS panels are vented to 3.45 kN/m² (0.5 psi). Consequently, limit design pressure is ± 3.45 kN/m² (0.5 psi) for upper surface structural panels and all of the TPS panels. Limit design pressures on the lower structural panels for positive angle of attack are simply equal to the net lower surface pressures--this assumes the cavity has been vented to absolute zero pressure.

A fatigue spectrum was established and initially defined in terms of airplane normal load factors. The spectrum included the four maneuvers and the loadings normally expected in service (i.e., gust, maneuver, taxi, and landing impact). By considering the maximum stress levels and the number of occurrences it was determined by using S-N curves for René 41 that there was no fatigue problem.

Surface area	Design condition							
	-0.5 g		1.0 g		2.0 g		2.5 g	
	kN/m ²	psi	kN/m ²	psi	kN/m ²	psi	kN/m ²	psi
1	1.758	0.255	1.896	0.275	3.372	0.489	4.633	0.672
2	1.758	0.255	2.096	0.304	3.572	0.518	5.068	0.735
3	1.758	0.255	2.096	0.304	3.572	0.518	5.068	0.735
4	2.972	0.431	3.634	0.527	6.081	0.882	8.798	1.276
5	1.731	0.251	1.869	0.271	3.158	0.458	4.682	0.679
6	0.634	0.092	0.938	0.136	1.779	0.258	2.503	0.363
7	1.738	0.252	2.117	0.307	3.661	0.531	5.302	0.769
8	1.738	0.252	2.206	0.320	3.841	0.557	5.588	0.809
9	1.731	0.251	2.372	0.344	4.171	0.605	6.012	0.872
10	1.717	0.249	2.689	0.390	4.820	0.699	6.840	0.992
11	4.413	0.640	0.717	0.104	0.462	0.067	1.448	0.210
12	2.234	0.324	0.248	0.036	0.290	0.042	0.565	0.082
13	1.076	0.156	0.069	0.010	0.214	0.031	0.221	0.032
14	4.564	0.662	0.627	0.091	0.469	0.068	1.351	0.196
15	2.296	0.333	0.262	0.038	0.310	0.045	0.621	0.090
16	1.083	0.157	0.083	0.012	0.228	0.033	0.255	0.037
17	2.482	0.360	0.758	0.110	0.931	0.135	1.758	0.255
18	2.482	0.360	0.758	0.110	0.931	0.135	1.758	0.255
19	2.158	0.313	0.758	0.110	0.931	0.135	1.758	0.255
20	4.930	0.715	0.758	0.110	0.931	0.135	1.758	0.255

Note: 1. Ramp and duct pressures not included.
2. Pressures are positive into the wing surface.

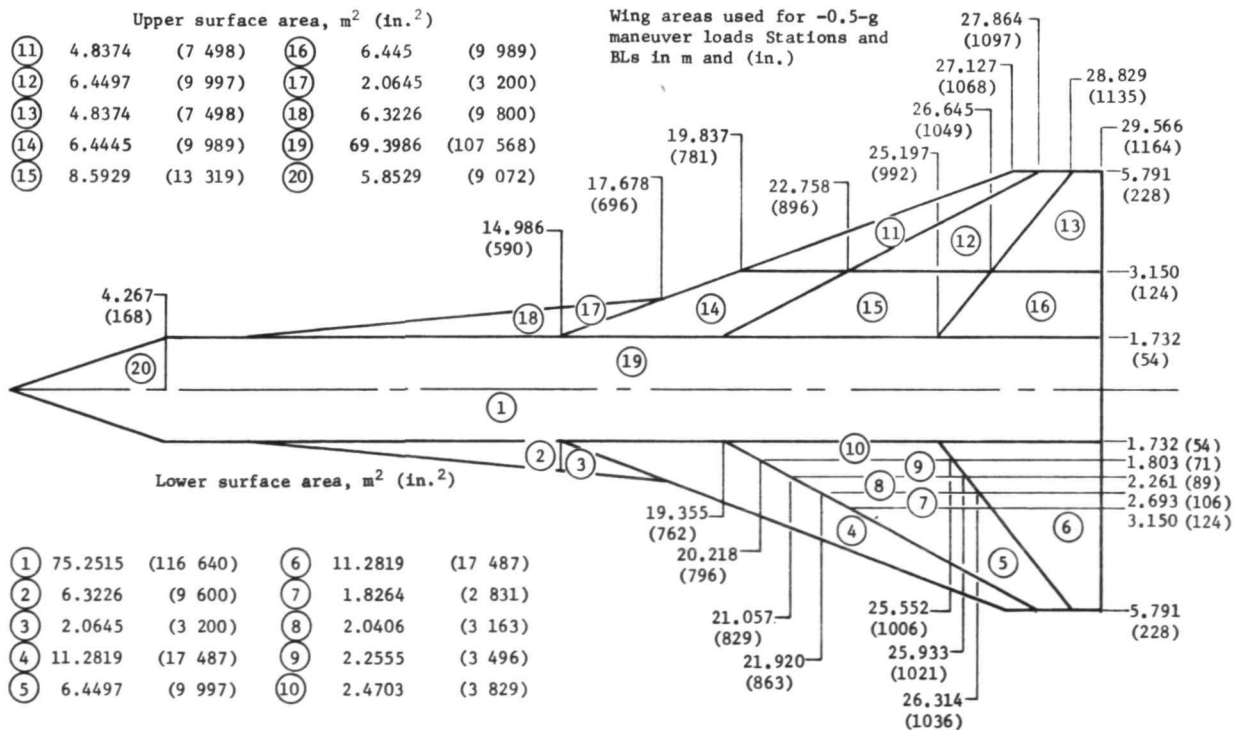


Figure 13 Net Aerodynamic Pressures for the Total Vehicle

Surface	Panel no.	Loads maneuver pushover -0.5 g		Loads maneuver pullup 2.5 g		Cruise 1.0 g		Launch maneuver	
		kN/m ²	psi	kN/m ²	psi	kN/m ²	psi	kN/m ²	psi
Lower surface structural panels	1	-4.130	-0.599	6.840	0.992	2.689	0.390	4.820	0.699
	2	-4.123	-0.598	6.012	0.872	2.372	0.344	4.171	0.605
	3	-4.116	-0.597	5.578	0.809	2.206	0.320	3.841	0.557
	4	-4.116	-0.597	5.302	0.769	2.117	0.307	3.661	0.531
	5	-4.068	-0.590	4.682	0.679	1.869	0.271	3.158	0.458
	6	-5.157	-0.748	8.798	1.276	3.634	0.527	6.081	0.882
Upper surface structural panels and all heat shields	1 ↑ ↓ 8	<div>← ±3.448 (±0.50) →</div>							
Positive pressures act into the wing surface.									

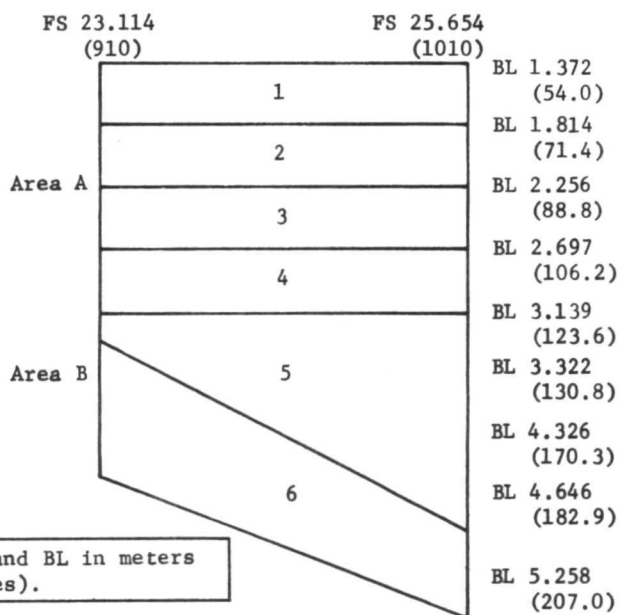


Figure 14 Wing Test Section Limit Design Pressures

WING OPTIMIZATION PROCEDURES AND RESULTS

GENERAL PROCEDURE

The wing optimization procedure consisted of an initial analysis of the wing followed by two iterations, with modifications between iterations, based on previous results. During each iteration, investigations of wing weight, versus spar spacing and versus rib spacing, and thermal protection system (TPS) were performed. The wing weight was represented by \bar{w} (volume per unit area) in plotting the weight trends. The initial structural sizes were selected on the basis of hand calculations based on preliminary loads. The iterations were performed by NASTRAN analysis of the entire vehicle. The internal loads, calculated by the NASTRAN procedure, were used in the analysis of individual components such as the beaded panels, rib and spar caps, and rib and spar webs. The $2\frac{1}{2}$ -g ultimate load case with its corresponding temperature distribution and resulting thermal stresses was found to be critical for design and used in the iterative procedure.

ASSUMPTIONS

The several assumptions were as follows:

- 1) The internal wing load intensities, calculated by NASTRAN, were assumed to remain constant regardless of variations in rib or spar spacings. For example, the load carried by spar cap or spar web was assumed to increase linearly with increasing spar spacing.
- 2) The region of the wing that determined the optimization included that portion that was fabricated as the test specimen.
- 3) The most severely loaded element of each type, whether on the top or bottom of the wing, was used throughout the wing region considered in the weight studies.

- 4) The critical beaded structural panel was selected from among the rectangular panels, excluding triangles and trapezoids, and was the one whose loading required the greatest strength and, therefore, the greatest material thickness.
- 5) The nominal mechanical and thermal loads, as calculated by the NASTRAN analyses of the airplane wing, were multiplied by factors of 1.95 and 1.5, respectively, for conversion from nominal to ultimate loads.
- 6) The ultimate venting pressure on an upper beaded panel was 5.171 kN/m^2 (0.75 psi). The equivalent ultimate pressure on a lower panel was 11.377 kN/m^2 (1.65 psi). This corresponds to the bending stresses and deflections produced on the beaded panel from the heat shield point loads [ultimate pressure on a lower heat shield is 5.171 kN/m^2 (0.75 psi)].
- 7) The radius of the panel bead was not restricted during the panel optimization calculations.
- 8) The width of the flat between beads on the beaded panel was maintained constant during panel optimizations.
- 9) A temperature difference of 5.6°K (10°F) was assumed to exist between the crest and trough of the beads.
- 10) An oxidation allowance of 0.0025 cm (0.001 in.) was added to the metal thickness.

ANALYSIS METHODS

Computer Program for Panel Optimization

The analytical procedures for the beaded panel optimization were coded into the OPTBEAD program. (The beaded panel details are shown in fig. 15.) The program has two options. The basic option is the procedure used in the selections of acceptable designs. This option identifies acceptable combinations of radius and thickness for the loads on a panel of a given length and width. The optimum configuration is that having the least weight from among the several acceptable configurations that the OPTBEAD program prints out.

The analytical option prints out various stresses, use factors, and deflections, regardless of the adequacy of the R and t combination, for any load and panel size.

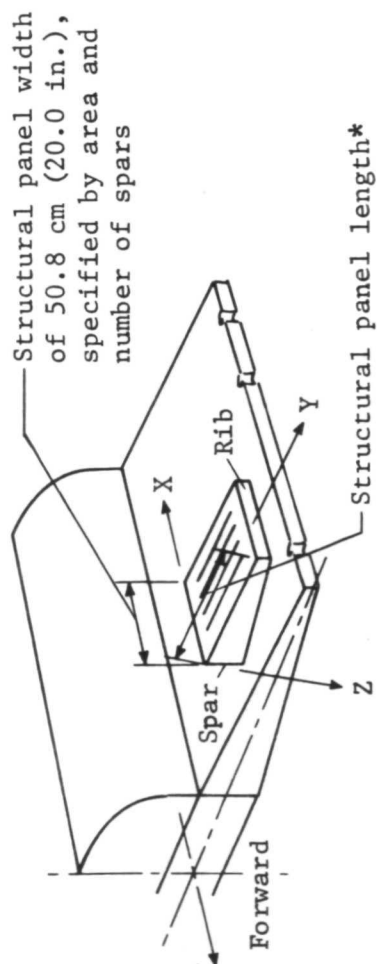
The panel optimization for the weight evaluation proceeds in the following manner. The loads for the panels are input as data. Ranges of bead radius and bead thickness are selected to cover the combinations required for strength and stability needed for rib and spar spacings. If the spar or rib spacings vary by equal increments, the automatic incrementing is used. If successive spacings do not vary by equal increments, only the initial and first-incremented length is automatically analyzed. The computer print-out is surveyed, for each panel size, for the configuration resulting in the least weight.

Shear Webs

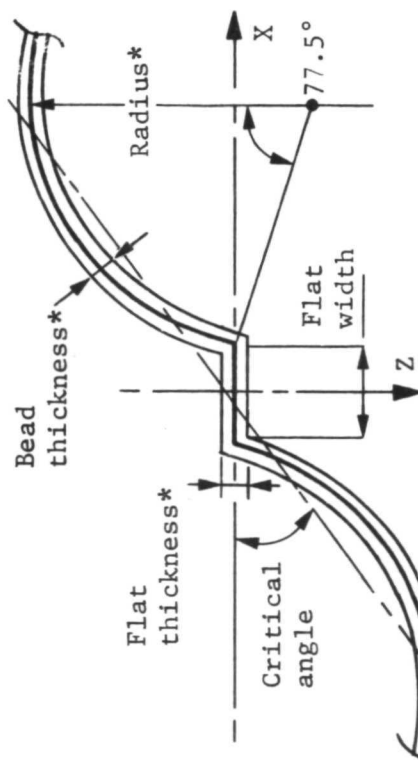
Circular arc corrugations were used for the rib and spar shear webs (fig. 16). The wing region under consideration was surveyed for the largest combined ultimate mechanical and thermal shear stress from the results of NASTRAN. The deeper end of the rib or spar was used because the stability strength was least where the web was deepest. Design curves for René 41 were determined. The corresponding radius to thickness ratio for the final value of depth to thickness gave the optimum radius of the circular arc corrugations for the specified load, temperature, and metal thickness. In cases where minimum gages dictated the metal thickness, a range of radii, rather than a single value, were permissible.

Spar and Rib Caps

The analysis method was used with a modification to bring the analytical method into agreement with the results of compression tests performed on cap specimens at 1033°K (1400°F) and at room temperature (fig. 17). The analysis method was modified to calculate the strength allowables by shifting the analytical curve to reflect the test data. The curve was found to be closely approximated by a function of thickness squared. It was assumed that the length of the cross section remained fixed and that the thickness varied.



(a) Wing panel coordinate system



(b) Bead panel cross section

*Variables for panel optimization

Figure 15 Beaded Panel Details

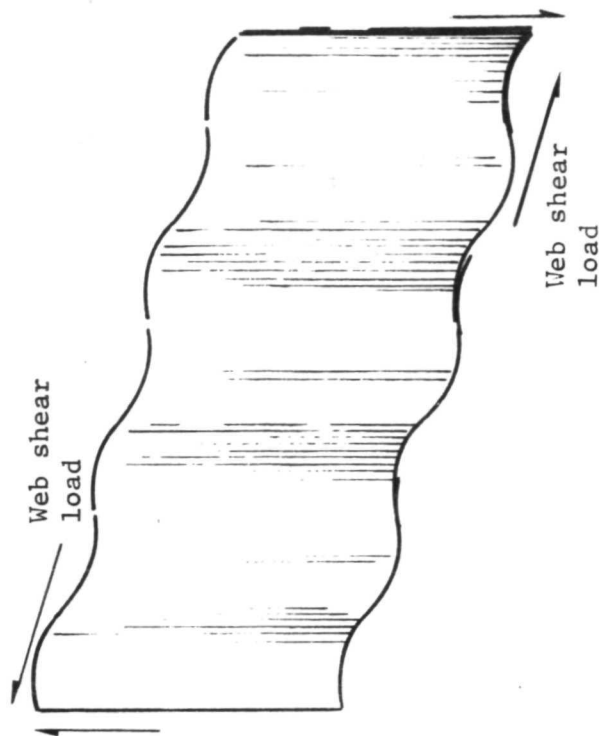


Figure 16 Configuration of Corrugated Webs

The largest ultimate rib and spar loads within the region being considered were selected and ratioed in proportion to rib or spar spacing.

The rib caps had splice straps for carrying load in double shear across the joints. These straps, together with the panel edges, panel doublers, and rib caps provided adequate rib cap strengths at BL 1.372 m (54 in.) with continuous splice straps. The rib cap at BL 2.464 m (97 in.) also has a splice strap, panel edges, and doublers, but the splice strap was not as thick as at BL 1.372 m (54 in.). The basic strength was assumed to vary in proportion to thickness squared with the cap area proportional to thickness. The area was thus increased as the rib spacing was increased in the weight study. Half of the area of the in-board and of the outboard rib caps was included in the cap area, to average the areas and thus the weight of the inner and outer rib caps.

As the spar spacing was increased or decreased, the load per spar was increased or decreased linearly and the area of the spar cap was also increased or decreased accordingly.

Heat Shields

A minimum-gage material thickness of 0.025 cm (0.010 in.) was established by the design that used two heat shield panels to cover one structural panel of 0.508 and 1.107 m (20 and 43.6 in.) (fig. 18). It was assumed that a similar heat shield of the same weight can be designed for other sizes, therefore, the t of the heat shield assembly was constant throughout the weight study. The heat shield support beams were placed to minimize the pressure bending moments in the overhang heat shield panels. The locations of the flexible supports under the support beams were placed to minimize bending moments and thus permit the use of lightweight beams. The support clips were made flexible in bending to accommodate the heat shield differential thermal expansion and were oriented toward the center of the panel as shown in figure 18. They were sufficiently strong to resist buckling or tensile failure under ultimate pressure on the heat shield surface.

The heat shield system design was essentially independent of the internal structural loads of the airplane wing calculated by NASTRAN. The weight of the heat shield assembly consisted of that of the 0.025 cm (0.010 in.) panel, the two support beams, the four support clips, the support gussets attached to the beaded panels, the fasteners, the edge strips, and oxidations allowance.

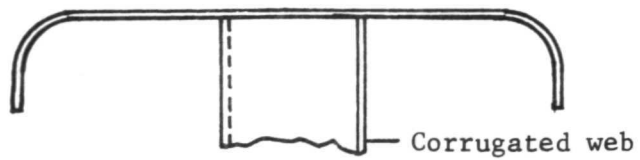
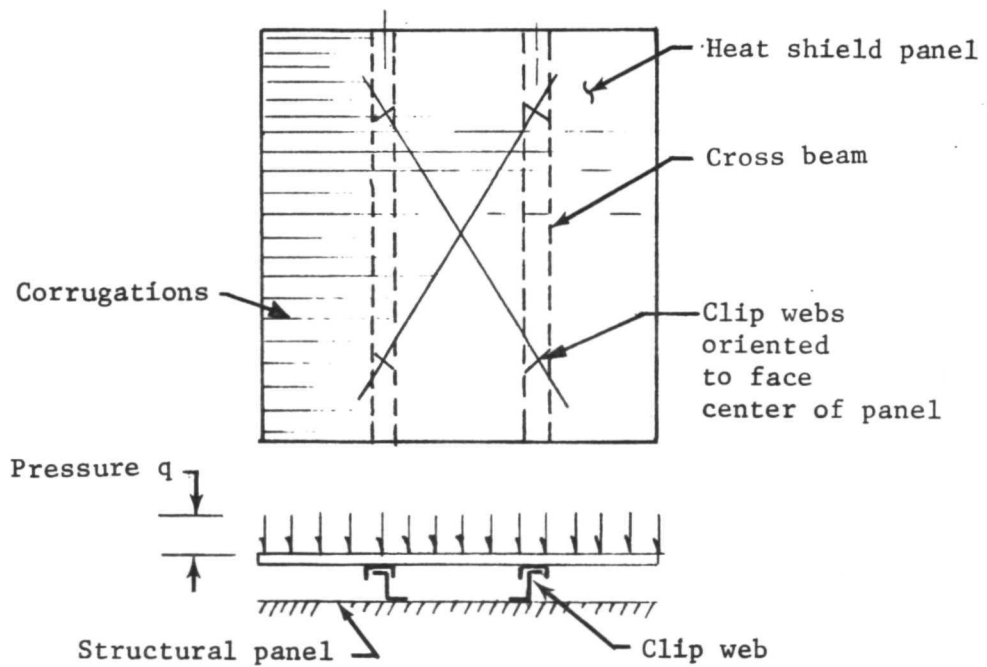


Figure 17 Rib Cap or Spar Cap Details with Corrugated Shear Web



(a) Heat shield cross section



(b) Heat shield support system

Figure 18 Heat Shield Details

ANALYSIS RESULTS

Temperature and TPS Arrangement

Detailed transient thermal analyses were conducted to determine stresses and deflections caused by temperature gradients through the wing structure. Isotherms were derived. Figures 19 and 20 show primary structure and heat shield temperatures for the final thermal analysis-TPS iteration (2.5-g condition). These wing temperatures were used as input to the NASTRAN internal loads program. Insulation (lower and upper surface outboard at 30% chordline) was placed to maintain the 1144°K (1600°F) material limit, and to minimize thermal gradients in the spanwise direction, thereby reducing thermal stresses.

Isotherms for radiation equilibrium temperatures on the fuselage are presented in figure 21. These fuselage temperatures were used for every wing optimization and NASTRAN analysis; however, the wing temperatures were modified with each iteration.

Critical Loads and Structural Geometry

The HRA was modeled for finite element analysis by systematically locating grid points at the intersections of spanwise and chordwise cuts. The proper elements were incorporated to represent the stiffness of the structure between grid points. Because of the symmetry of the structure and of the loading, only half of the airplane required modeling. A NASTRAN computer plot of the undeformed model is shown in figure 22.

Figure 23 compares spanwise normal stress resultant N_y in the inboard top and bottom panels due to the four mechanical loading conditions for the third and final NASTRAN iteration. This comparison established the 2.5-g loading condition as the critical condition for panel design. The symmetry of the curves for the top and bottom panels indicates that the response of the wing to the mechanical loads is almost pure bending as expected.

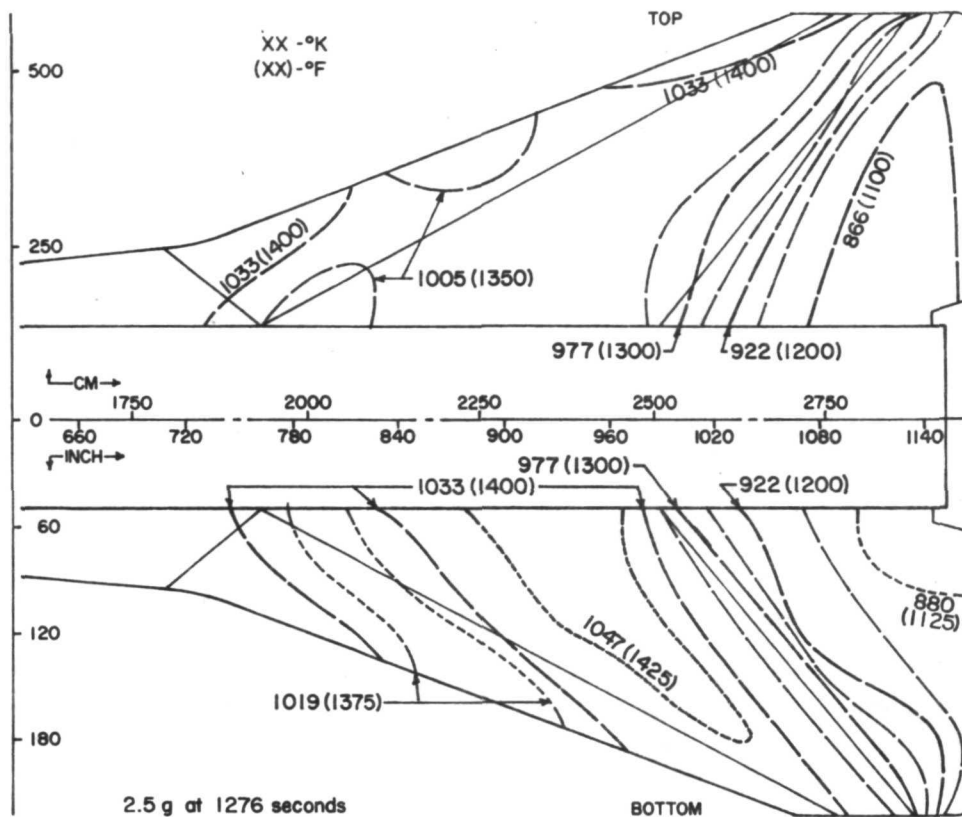


Figure 19 Primary Structure Temperatures For Beaded Panels

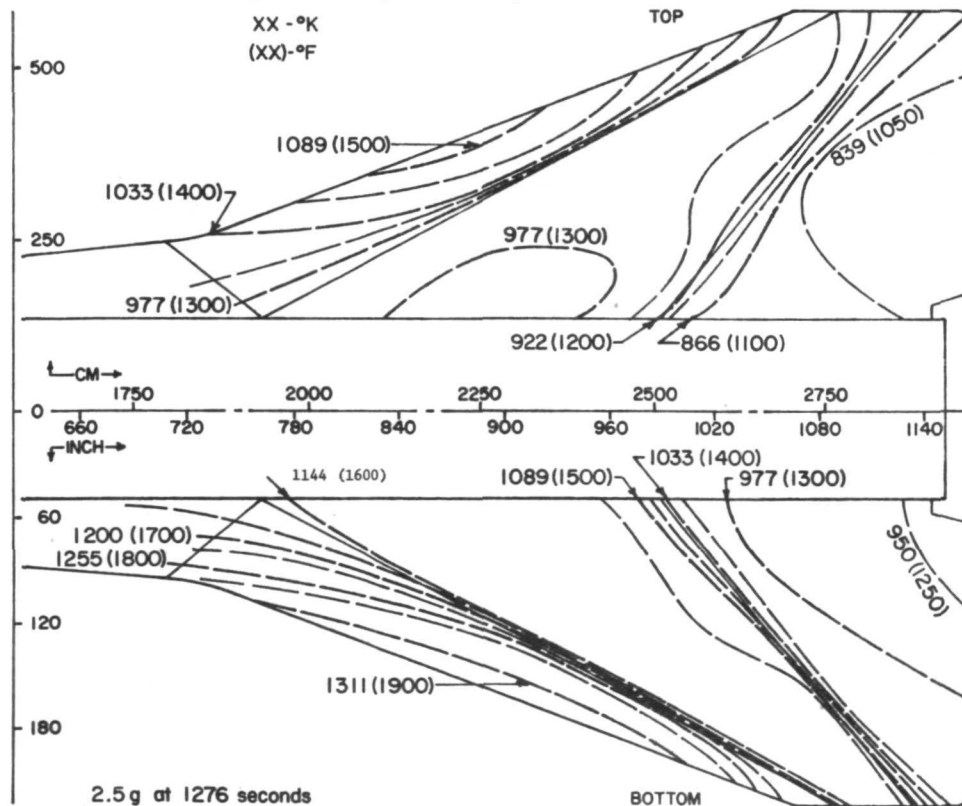


Figure 20 Heat Shield Temperatures

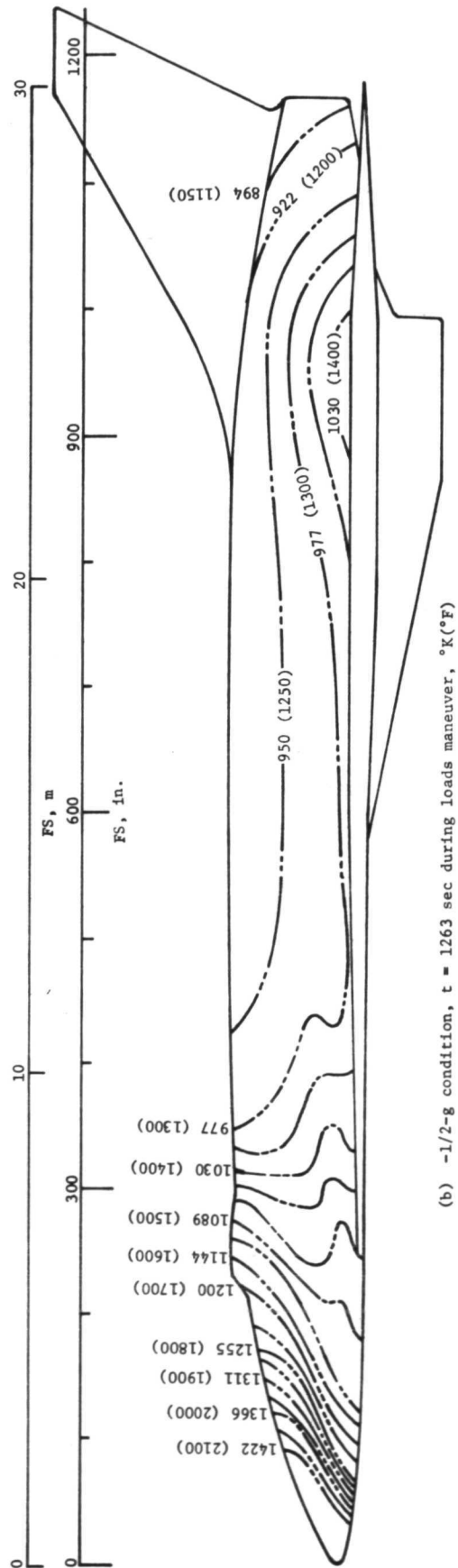
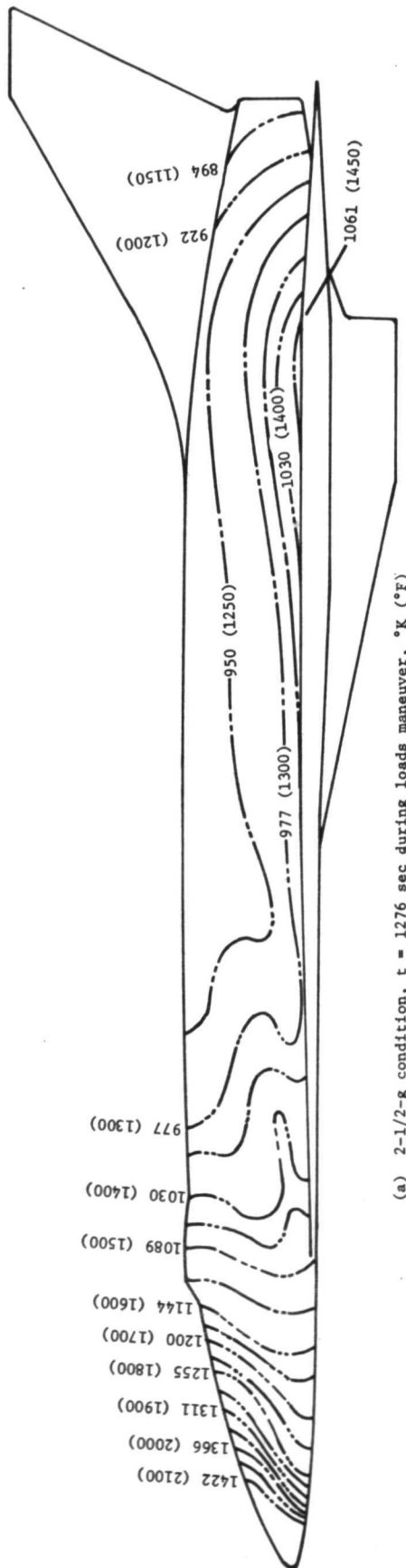


Figure 21 Fuselage Isotherms

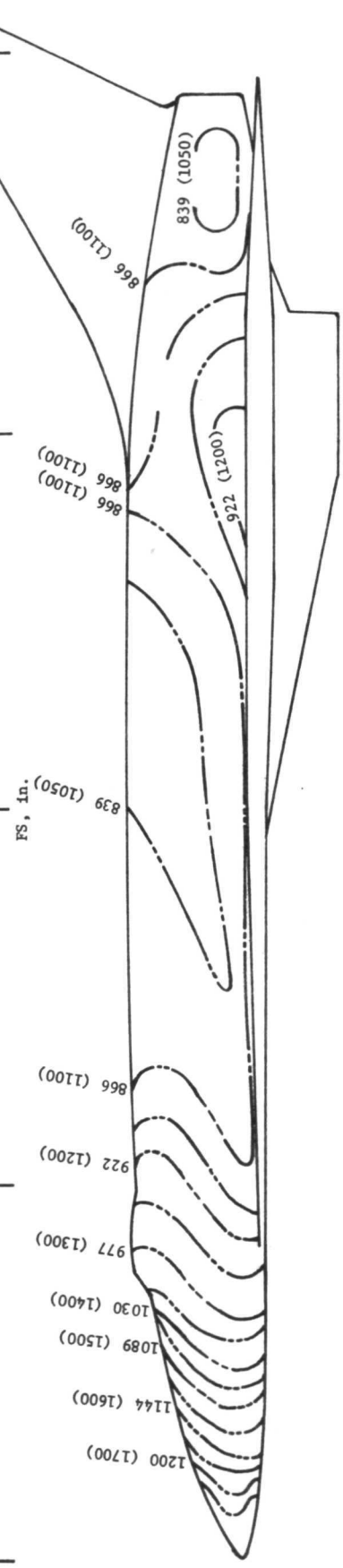
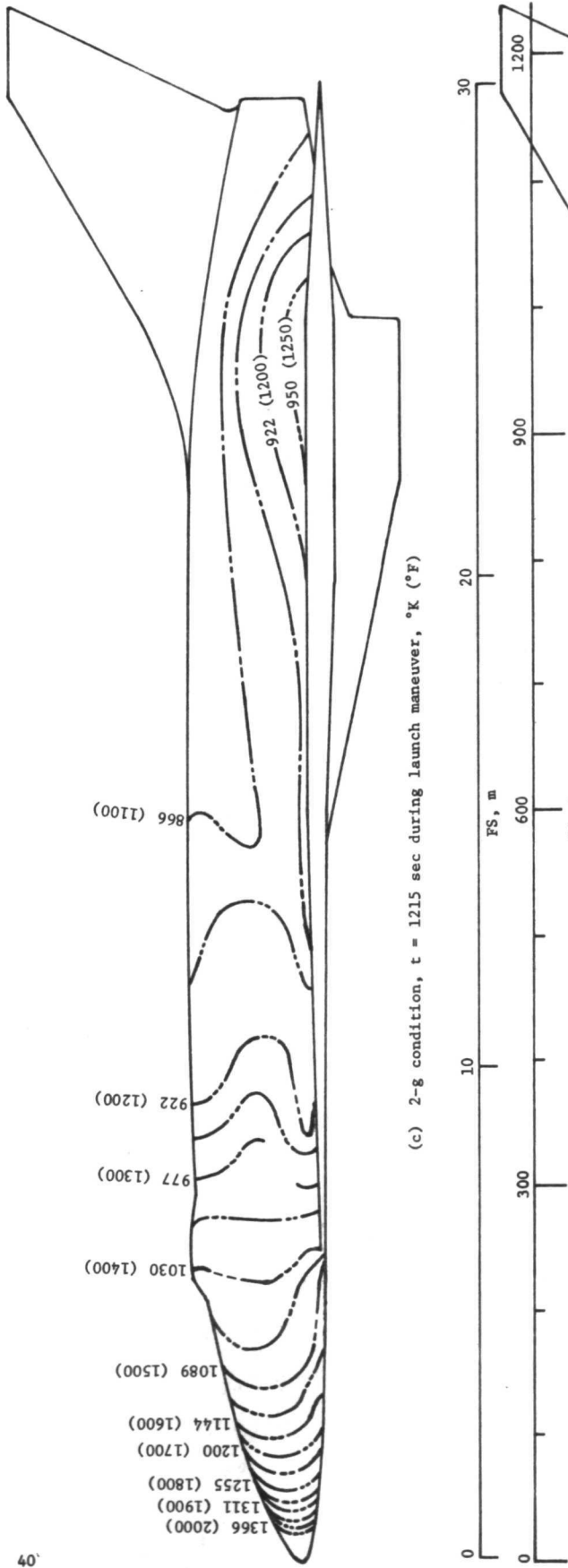


Figure 21 Fuselage Isotherms---Concluded

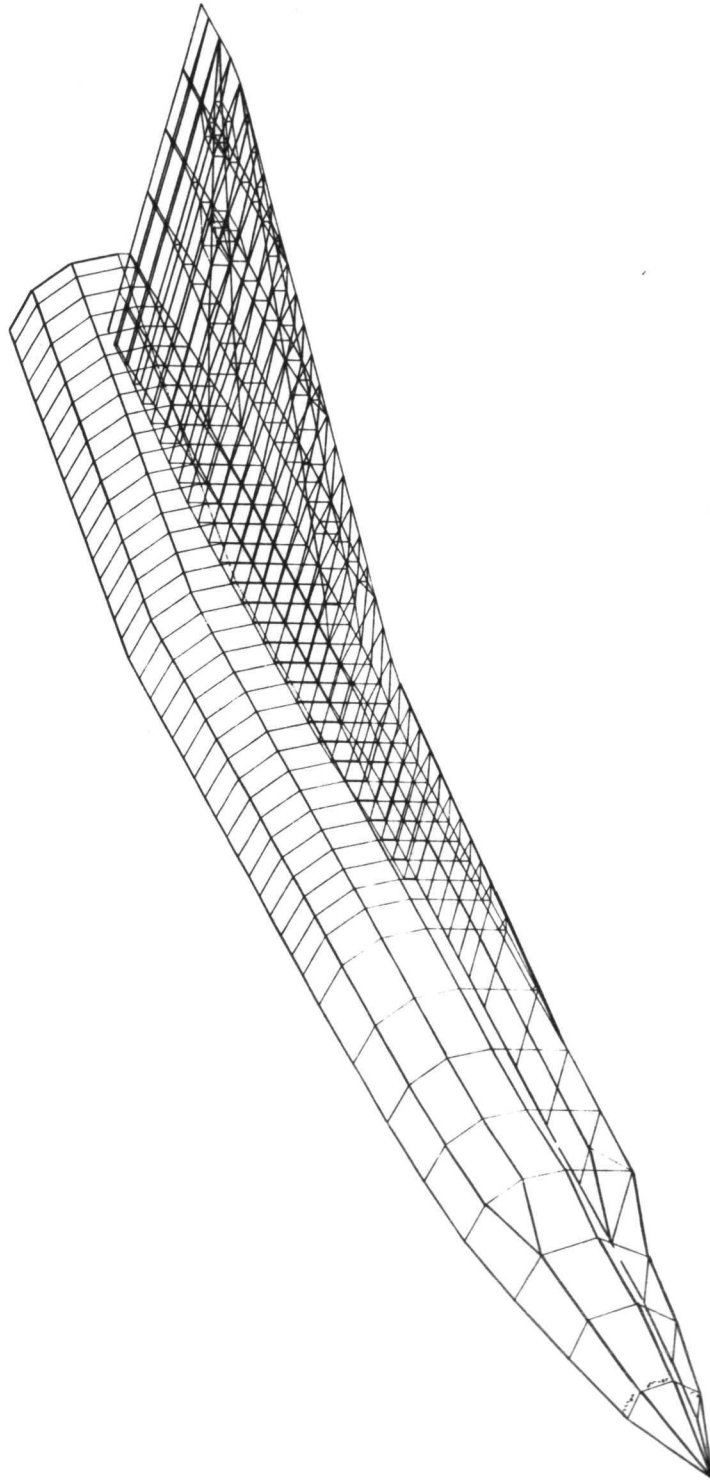


Figure 22 Computer Plotted NASTRAN Model of Undeformed Structure

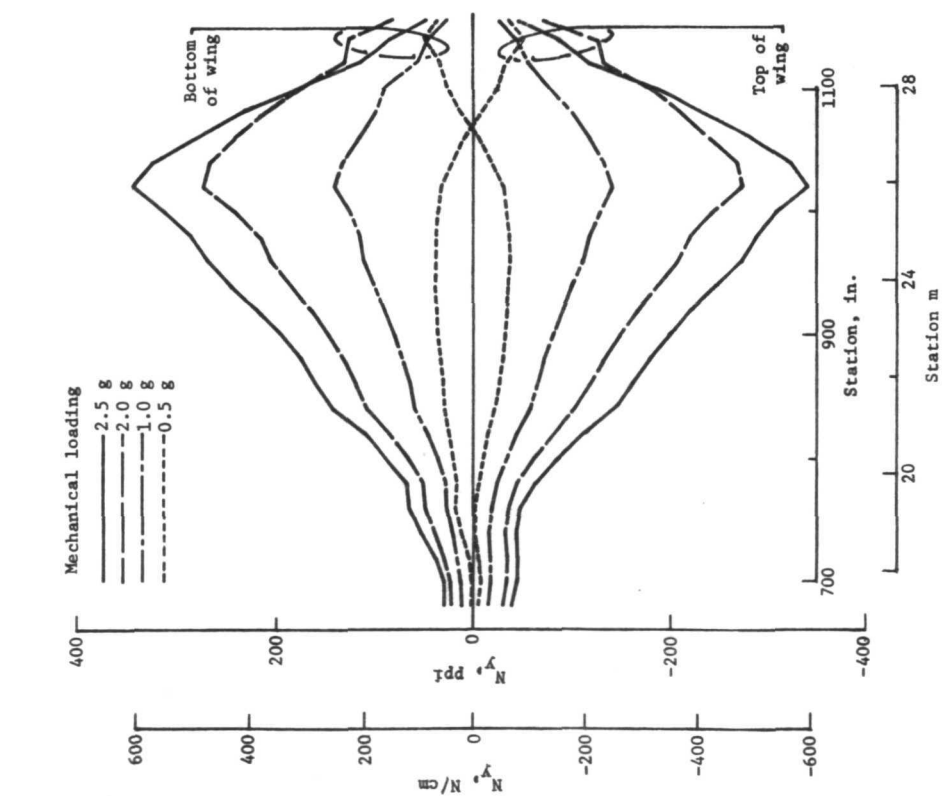


Figure 23 Mechanical Normal Stress Resultant in Structural Panels along BL 1.372 m (54.00 in.) for Noted Loading Conditions

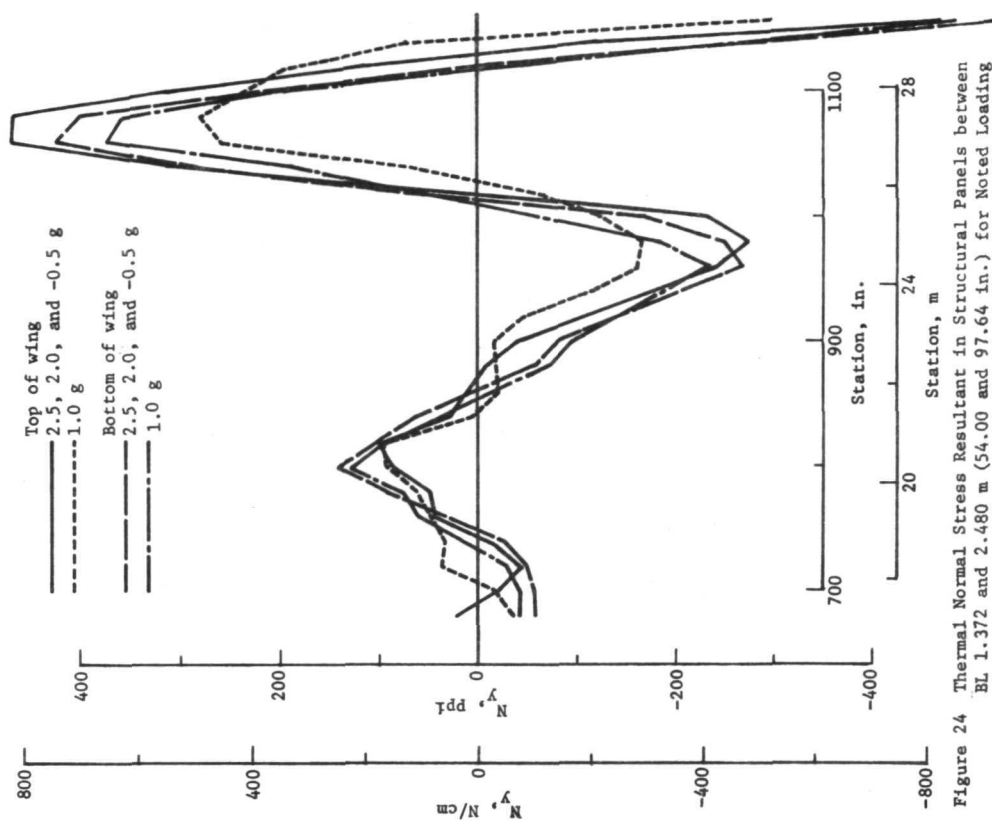


Figure 24 Thermal Normal Stress Resultant in Structural Panels between BL 1.372 and 2.480 m (54.00 and 97.64 in.) for Noted Loading Conditions

In Figure 24 is given the spanwise thermal normal stress resultant N_y in the top and bottom panels for the various thermal loading conditions. For this temperature distribution, the associated thermal stresses had a great influence on panel design. Total normal stress resultants are obtained by superimposing these curves on those of figure 23. The 2.5-g load condition was established as the most critical for panel design. A superposition criterion was used for combining mechanical and thermal stresses because the analysis was based on linear theory.

Also, it can be concluded from figures 23 and 24 that the mechanical loads reduced at the aft end of the airplane and the thermal loads increased at the aft end of the airplane. While a thermal analysis and TPS evaluation were conducted during each of the three design iterations, the aft thermal stresses could not be reduced by insulation placement because of the shape of the wing cross section.

The location of the critical upper surface wing beaded panel is shown in figure 25 for the three successive designs. In all three designs, the critical panel was adjacent to the wing root and within the region between FS 23.144 and 25.654 m (910 and 1010 in.). The loads on the critical panels are shown in table VI, which presents the loads on the panels, caps, and shear webs for the final design.

Table VI also contains the $\bar{\epsilon}$ of the components corresponding to the baseline spar and rib spacings of 0.508 and 1.107 m (20.0 and 43.6 in.), respectively.

The beaded panel configuration for the final design was determined by the OPTBEAD program for the loads shown in table VI. The optimum beaded panel configuration for the final design is shown in table VII. The final configuration is not exactly the same as that used in the wing test structure due to practical considerations of spar spacing and actual test loads. The wing test structure design has a $\bar{\epsilon}$ of 0.091 cm (0.036 in.). The test structure configuration has a bead radius of 2.654 cm (1.045 in.) corresponding to seven beads in the 0.508 m (20-in.) spar spacing. An odd number of complete beads is required in the test structure to accommodate the heat shield supports. Seven beads is the most nearly optimum number. Between the second and third designs, it was determined that the width of the flat between beads should be increased from 0.953 to 1.111 cm (3/8 to 7/16 in.) to facilitate spot welding of panel doublers.

TABLE VI
ULTIMATE DESIGN LOADS AND THICKNESSES

Component	Load	Third and final design									
		Axial load				Shear		Pressure		Theo t*	
		N/cm	ppi	N	lb	N/cm	ppi	N/m ²	psi	cm	in.
Upper panel	Mechanical	-988	-564	--	--	-343	-196	--	--	0.1001	0.0394
	Thermal	-729	-416	--	--	-194	-111	--	--	--	--
	Sum, mech + th	-1717	-980	--	--	-538	-307	--	--	--	--
	Equiv pressure	--	--	--	--	--	--	5 171	0.75	--	--
Lower panel	Mechanical	970	554	--	--	229	131	--	--	0.1001	0.0394
	Thermal	-658	-376	--	--	-412	-235	--	--	--	--
	Sum, mech + th	970	554	--	--	-412	-235	--	--	--	--
	Equiv pressure	--	--	--	--	--	--	11 377	1.65	--	--
Rib cap	Mechanical	--	--	1 076	242	--	--	--	--	0.0152	0.0060
	Thermal	--	--	-20 017	-4500	--	--	--	--	--	--
	Sum, mech + th	--	--	-20 017	-4500	--	--	--	--	--	--
Spar cap	Mechanical	--	--	-8 821	-1983	--	--	--	--	0.0196	0.0077
	Thermal	--	--	-6 561	-1475	--	--	--	--	--	--
	Sum, mech + th	--	--	-15 382	-3458	--	--	--	--	--	--
Rib web	Mechanical	--	--	--	--	-270	-154	--	--	0.0099	0.0039
	Thermal	--	--	--	--	44	25	--	--	--	--
	Sum, Mech + th	--	--	--	--	-270	-154	--	--	--	--
Spar web	Mechanical	--	--	--	--	-270	-154	--	--	0.0216	0.0085
	Thermal	--	--	--	--	61	35	--	--	--	--
	Sum, mech + th	--	--	--	--	-270	-154	--	--	--	--

*Thickness includes 0.003 cm (0.001 in.) oxidation allowance.

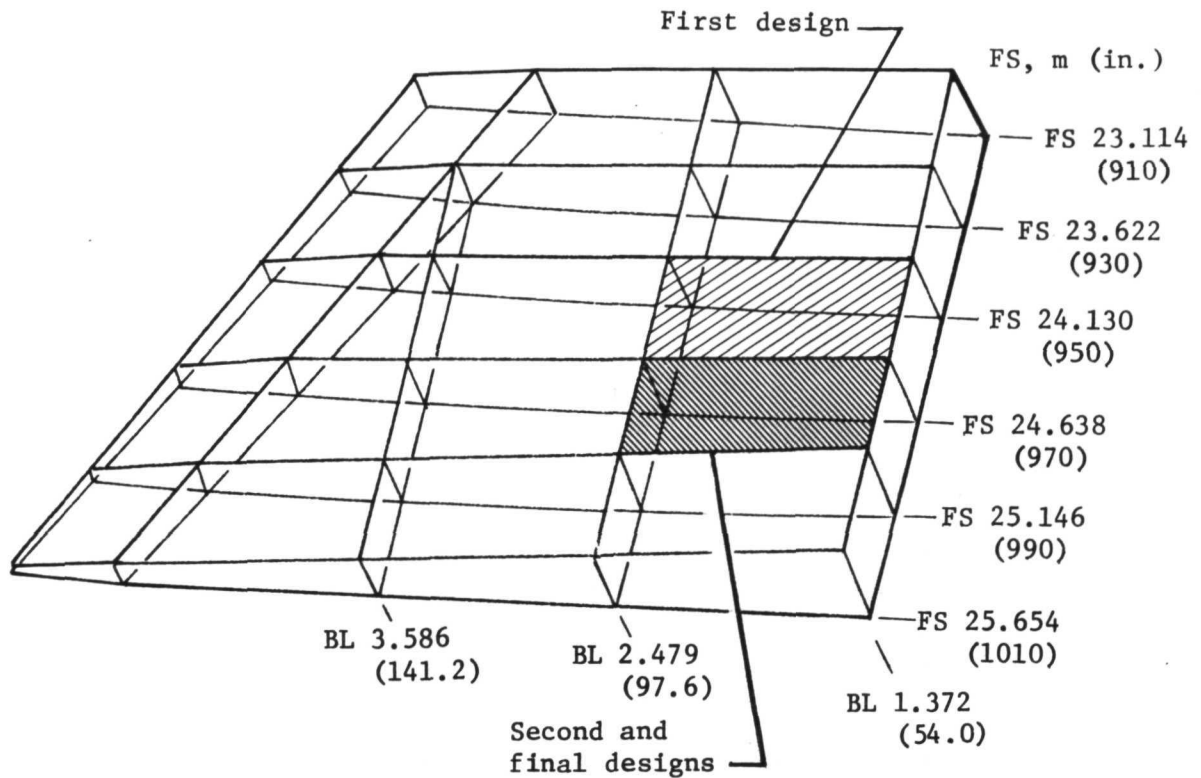


Figure 25 Critical Panels for Three Design Iterations

TABLE VII
CONFIGURATIONS OF BEADED PANELS
FOR THE FINAL DESIGN

Element	Design	
	in.	cm
Bead radius	1.125	2.858
Bead thickness	.028	.071
Width of flat	7/16	1.111
\bar{t}	.0384	.0975
\bar{t} [include 0.0025 cm (0.001 in.)]	.0394	.1001

Strength interaction curve for the critical panel of the final design is presented in figure 26. The maximum panel strength involves interaction between pressure, axial loads, and shear load. The strength interaction curve facilitates investigation of various wing panels for structural adequacy. If the coordinates of a point corresponding to the combined mechanical and thermal axial and shear load falls within the boundary of the curve, the design is adequate for the applied loads.

Effect of Spacing on Weight

The loads of table VI are for the most severely loaded compression and tension panels, webs, and caps in the wing region considered. The upper wing beaded panel was subjected to compressive axial loads, the lower panel was subjected to tensile loads. The upper panel was critical for design because of beam-column strength interaction, or stability limitations. The panel with optimum \bar{t} , selected by means of OPTBEAD, was an upper panel.

All the lower panels and all other upper panels had the same \bar{t} as the critical panel for the purpose of simplifying the analysis for estimating weight. Similarly, the upper rib or spar caps were assumed to have the same \bar{t} as the lower, although the higher compressive load is generally critical for design. The wing weight for the most critical load condition was .041 N/cm² (8.5 psf) however, the average unit weight for the total wing will be less if it was optimized for the variation in loads.

Rib Spacing.— The configuration of 0.508-m (20.0-in.), spar spacing and 1.107-m (43.6-in.) rib spacing was the reference point for the analytical variation of both the spar and rib spacings. As the panel length corresponding to the rib spacing was varied, the OPTBEAD program was used to calculate the optimum \bar{t} for each of several selected panel lengths. The total \bar{t} corresponding to both the upper and the lower panel was plotted in the lower portion of figure 27 for the third and final design. Also included as \bar{t} versus rib spacing in the lower part of figure 27 are the \bar{t} of the heat shields, shear webs, and caps. The total \bar{t} of the wing was plotted versus rib spacing as the uppermost curve in figure 27 for the final design. During the analytical variation of rib spacing for the calculation of corresponding \bar{t} , the spar spacing was assumed to remain fixed at 0.508 m (20.0 in.). The \bar{t} curve of figure 27 indicates a minimum \bar{t} in the region of 1.270 to 1.524-m (50 to 60-in.) rib spacing. The use of a rib spacing of 1.107 m (43.6 in.) is slightly nonoptimum. Rib spacing was influenced by the requirement of 0.508 m (20.0 in.) spar spacing centered at FS 24.384 (960). Equal spaces in the spanwise direction were made to occur at the intersection of a spar and the 30% chord.

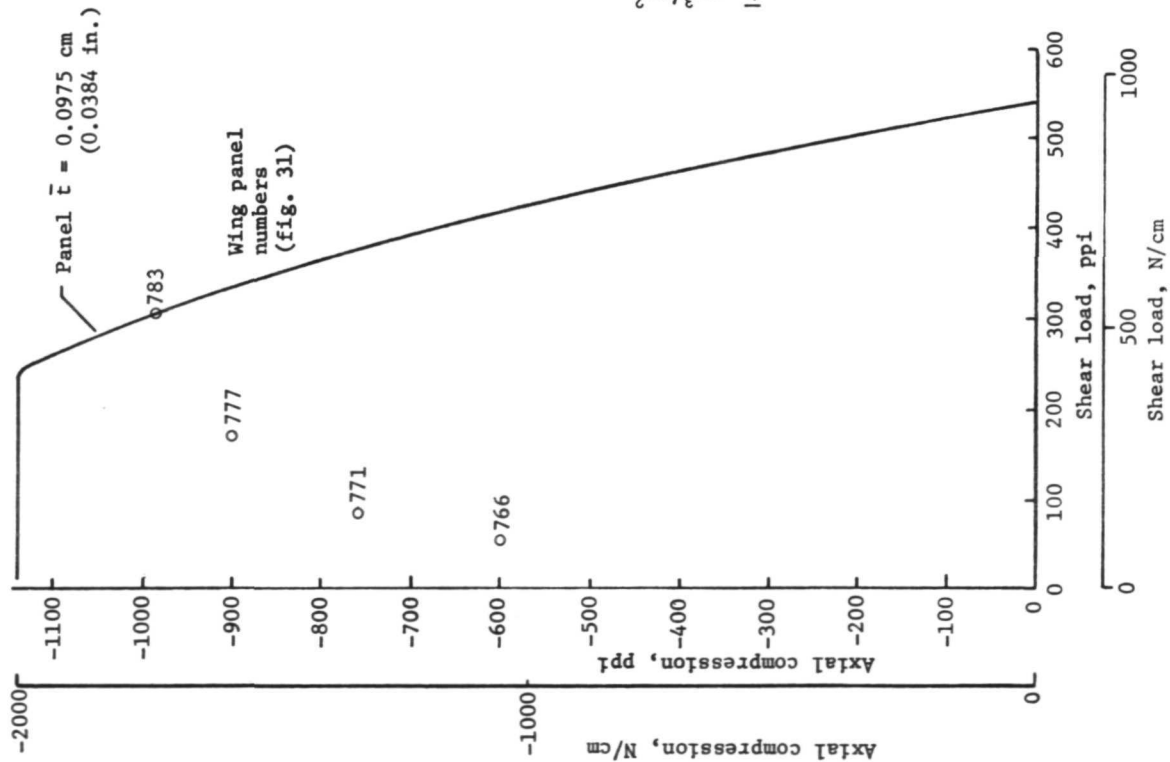


Figure 26 Strength Interaction Curve for Beaded Panels for Final Design

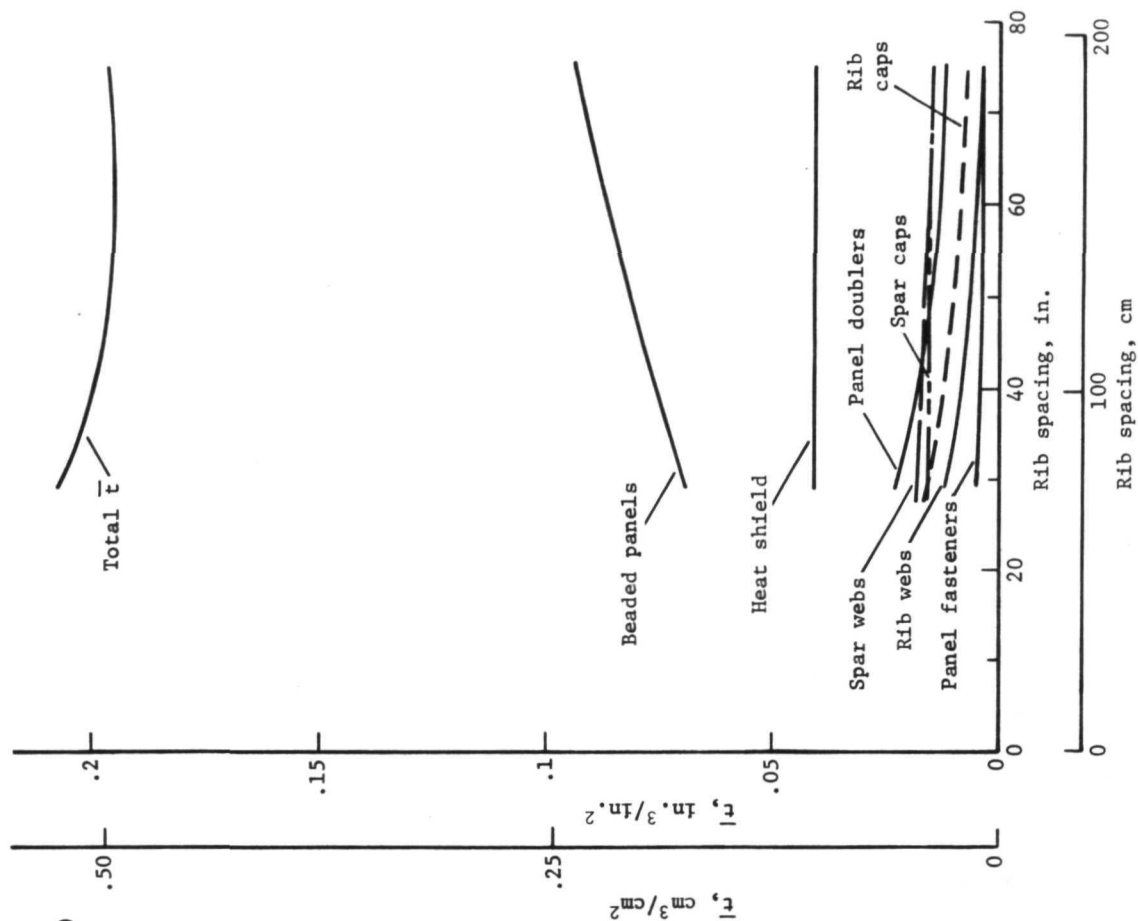


Figure 27 Wing Weight (\bar{t}) for Final Design as a Function of Rib Spacing

Spar Spacing.- With the rib spacing assumed constant at 1.107 (43.6 in.), the \bar{t} of the wing was calculated for several spar spacings and plotted in figure 28. The \bar{t} of various components was plotted versus spar spacing in the lower portion of figure 28 for the final design. The heat shield \bar{t} was assumed to be independent of spar spacing because the heat shield support was designed to minimize the transfer of wing loads into the heat shield panels. Because the OPTBEAD program results in beaded panel configurations, which are essentially independent of spar spacings, the \bar{t} versus spar spacing shown in the lower portion of figure 28 was plotted as a constant value.

The curve of \bar{t} versus spar spacing does not reach a minimum within the spar spacing range of 0.508 to 2.540 m (20 to 100 in.), primarily because the thickness of the beaded panels was relatively insensitive to spar spacing. Although the curve indicated the desirability of large spar spacings, practical limitations in manufacturing and handling impose upper limits to panel sizes. To provide five panels, spaced chordwise, for 7.9 sq m (85 sq ft) of test specimen, it was necessary to limit spar spacing to 0.508 m (20 in.) or less. This provided simulation of panels that were remote from free edges of the wing specimen, thus representing the type of loading and constraint to which a typical internal wing panel will be subjected.

Objectives of this program include using the wing test structure as a flight-loads measurement system prototype. In addition, tests will be performed to evaluate flight-loads instrumentation, methods of high-temperature calibrations, and temperature simulation techniques. Finally, a series of tests to the design conditions will be performed to demonstrate the structural concept and to compare analytical and experimental data.

Small departures from optimum spacings are not of significance to the overall program objectives.

Aeroelastic Analysis

Vehicle Flutter.- Flutter was considered in a qualitative manner showing more than an adequate margin on airspeed and dynamic pressure (beyond the 1.3 factor) over the design flightpath. This type of vehicle can be expected to have large margins on flutter. Comparison of planform parameters and the flight envelope of the HRA wing and the wing and airplane of similar construction (ref. 2) indicated a large positive flutter margin.

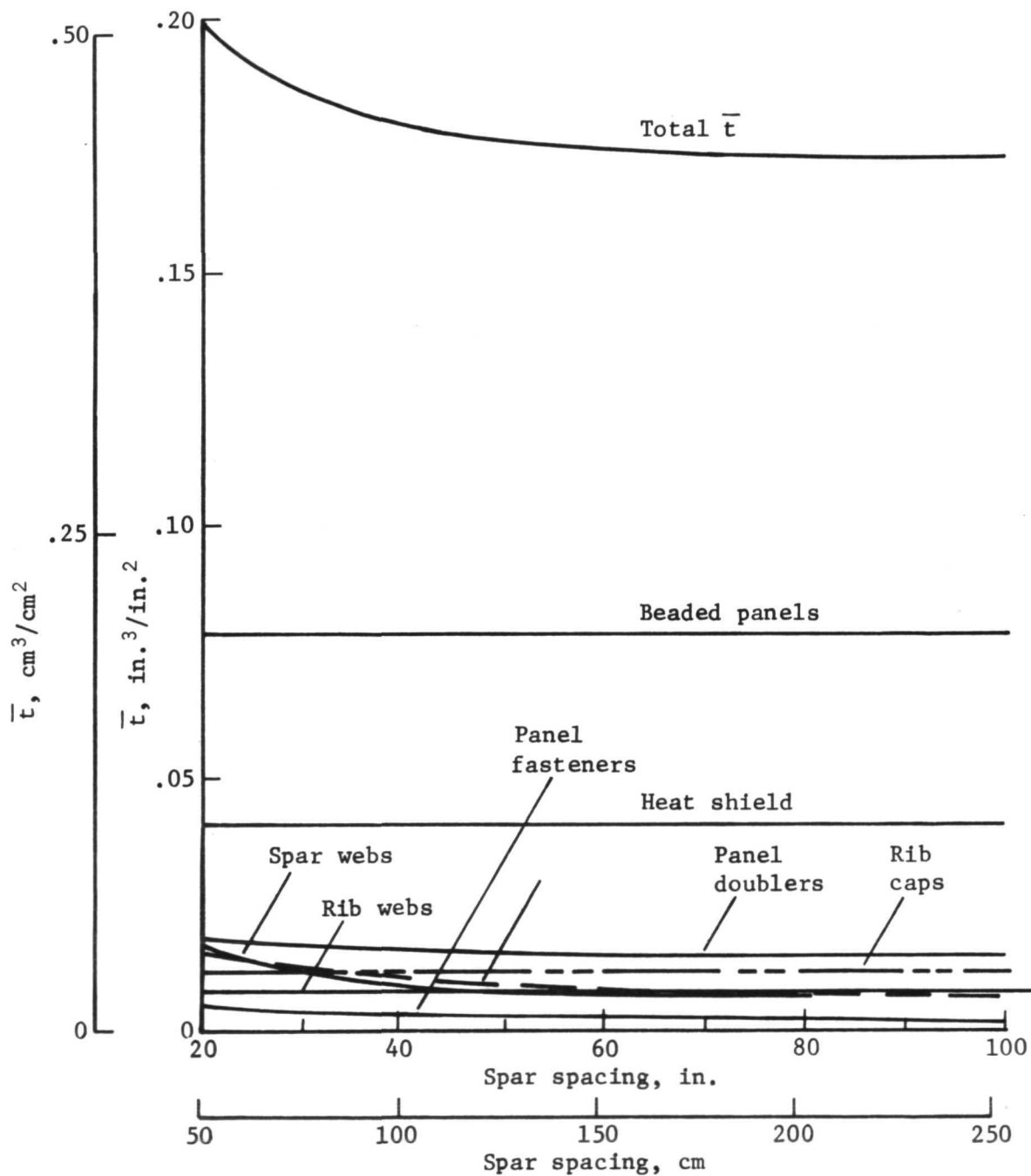


Figure 28 Wing Weight (\bar{t}) for Final Design as a Function of Spar Spacing

Panel Flutter.- A flutter analysis was performed on the heat shields using the theory and monographs presented in references 20 through 23. Effects due to elastic foundations, the corrugations, flow angularity, static pressure differential, and the cavity between the heat shield and structure were considered in the analysis. Results of this analysis indicated that flutter of the heat shield panel should not occur for low values of flow angularity. Reference 23 shows the sensitivity to flutter of a single-sheet, beaded heat shield panel as the flow angle changes from zero. For this test structure the heat shield performs principally as a thermal barrier, and secondarily as an aerodynamic surface.

Sonic Fatigue Analysis.- Analyses were performed on wing beaded panels, heat shields and flexible clips. The configurations were designed to survive the worst case acoustic loading of 159 dB overall sound pressure level, for the entire duration of each mission, for 150 missions. This is a very conservative assumption for the 159-dB condition is associated with the loads maneuver, 30 of the 150 total flights. The total time associated with this condition was assumed to be the total flight time of 150 missions of 45 minutes each.

Creep Analysis

A creep analysis was conducted, and it was found the total creep strain for a 150 flights was less than 0.5%.

WING TEST STRUCTURE DESIGN AND ANALYSIS

Part of the hypersonic airplane wing was designed, fabricated, and assembled into a test structure as a means of experimentally verifying the structural adequacy of the beaded panel design concept. In order that the wing deflections be more closely simulated under flight loads, a support framework was designed with spanwise stiffness characteristics approximating those of the fuselage. For economic reasons, the wing test structure geometry was modified between the leading edge and the 30% chord line and the small change in surface at the 70% chord line, affecting a small portion of one panel, was not included, as shown in figure 29.

The test structure was subjected to structural analysis to obtain stress and deflection data for the following:

- 1) Design of the fuselage simulating support structure and attachments;
- 2) Design of the load fixture attachments;
- 3) Calculation of the required interface and external loads for simulation of actual flight conditions;
- 4) Correlation with stress and deflection data from the airplane analysis and evaluation of the success of the simulation of actual flight loads;
- 5) Verification of the adequacy of the approximated shape of the test section.

DESCRIPTION OF STRUCTURE

The test portion of the wing extends from FS 23.114 to 25.654 m (910 to 1010 in.) Basically, the wing portion of the test structure was the same as its airplane counterpart except in the area of the leading edge. The leading edge is rotated slightly to make the outboard panels identical. A comparison of the airplane and test structure planforms in the area of interest is shown in figure 29.

The support structure consisted of a steel framework and an interface (carrythrough) region connecting the wing test structure to the framework. The combination was designed to simulate the spanwise stiffness characteristics of the fuselage. Whereas the

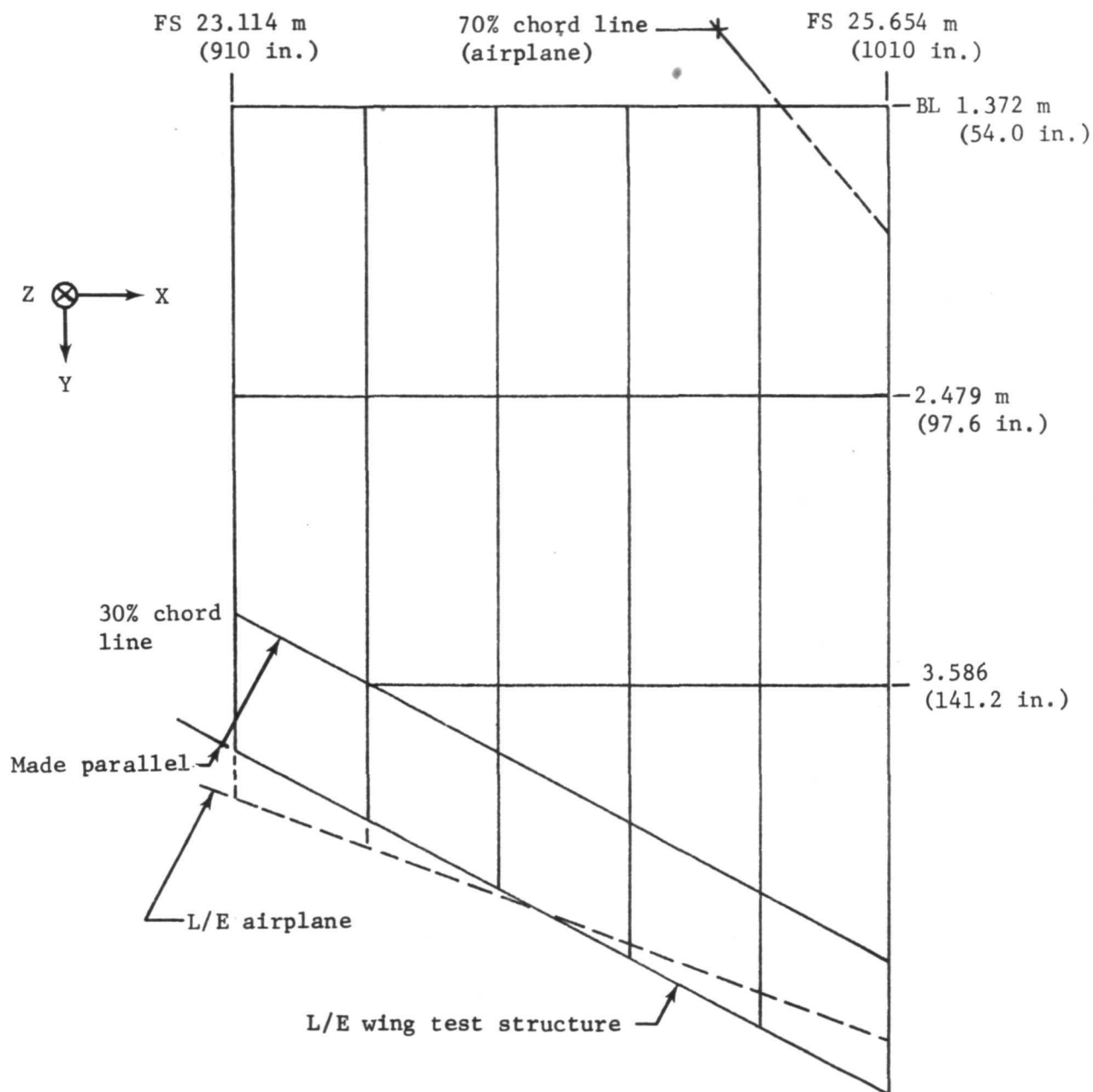


Figure 29 Comparison of Airplane and Test Structure Planforms

wing test structure is heated during test, the framework is kept cool. For this reason, some of the thermal deflections simulating those in the airplane will probably not be directly realized. The framework was designed to have one hard point at FS 24.638 m (970 in.) that will undergo practically no thermal displacement in the X-Z plane. Thermal displacements of the wing in the X-Y plane emanate radially from this point. The steel framework was a simple three-dimensional truss structure composed of standard structural members.

TEST STRUCTURE LOAD ANALYSIS

Finite Element Model

The NASTRAN model of the wing test structure was essentially the same as the corresponding part of the airplane wing. The support framework was modeled by bar and rod elements. A computer plot of the test structure model is shown as figure 30.

Loads Analysis

Loads that were continuously distributed as pressures and stresses in the airplane under flight conditions were simulated by a distribution of concentrated loads at a relatively small number of loading points on the test structure. This required the test structure to be locally hardened to support concentrated loads, and the loads were calculated with high precision so similar stress and deflection responses were maintained. Both the external loading and the interface loading on FS 23.114 and 25.654 m (910 and 1010 in.) were simulated, and the loads carried through from the fuselage response were realistic.

The support structure was designed initially by means of preliminary stress analysis to approximate the resistance to spanwise wing bending. To check the adequacy of the design, a NASTRAN analysis of the support structure under actual interface loads was performed. Member sizing modifications were made to adjust the stiffness characteristics and to assure structural stability.

The interface loads on the wing/fuselage intersection as well as on the wing cuts at FS 23.114 and 25.654 m (910 and 1010 in.) and the external surface loads to be applied at the actual number of loading points were obtained through a NASTRAN analysis of the wing portion of the test structure isolated from the support structure. In this run, displacements, expressed in the airplane reference system, were prescribed at all the points that were loaded

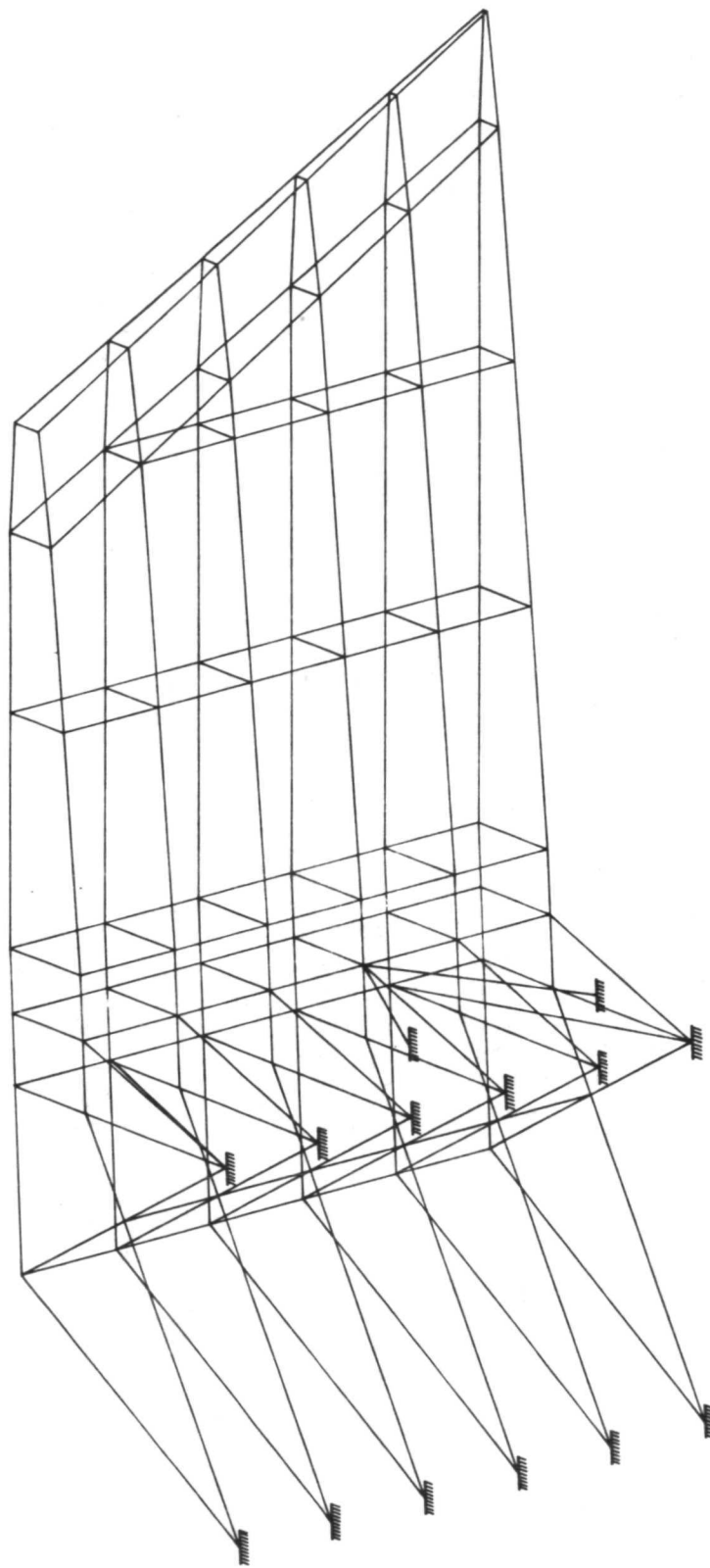


Figure 30 NASTRAN Plot of Wing Test Structure, Transition Section, and Support Structure

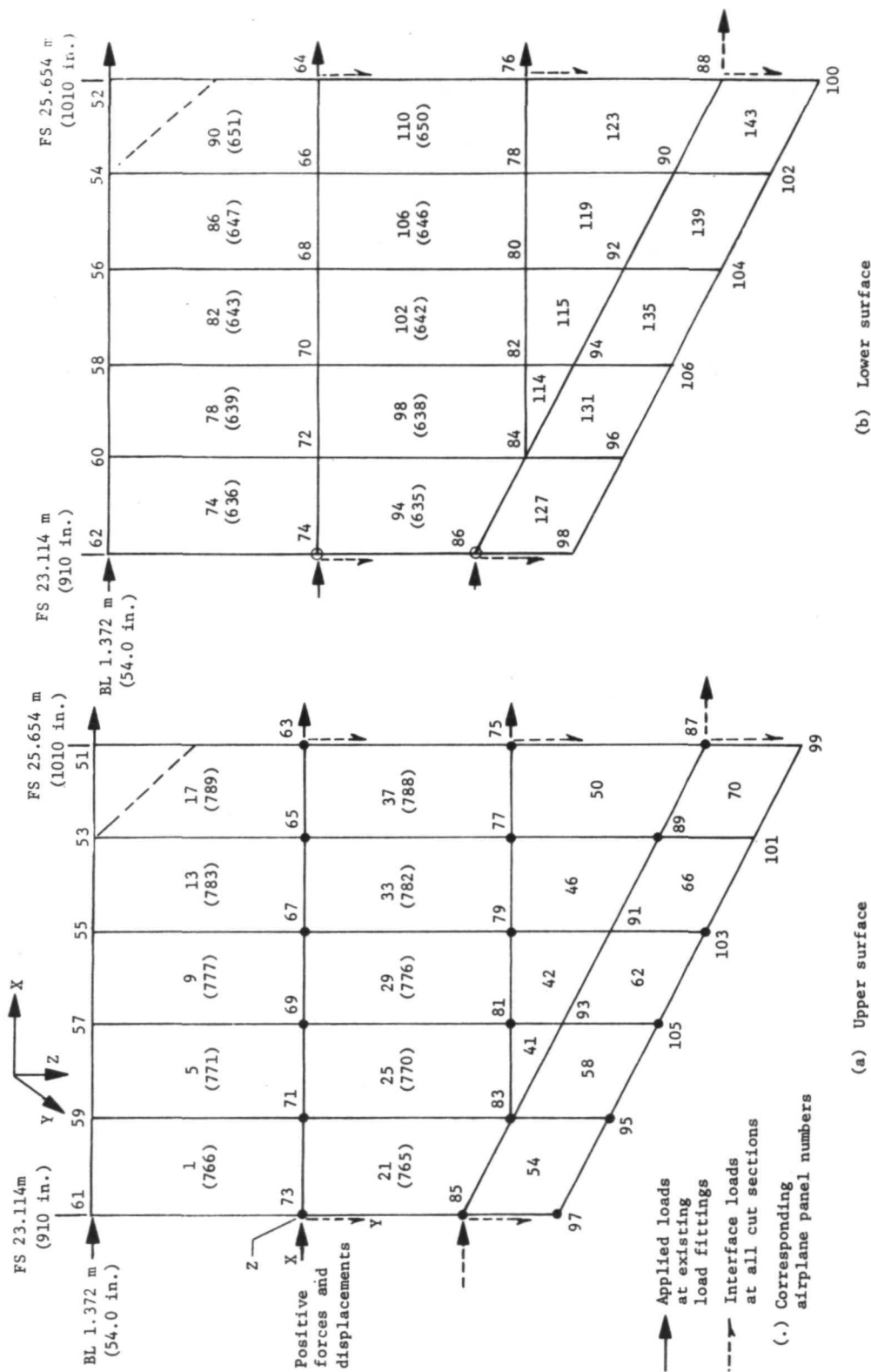
in all the directions of the concentrated loads (fig. 31) and in all three directions at points on the wing/fuselage interface. These prescribed displacements were equal to the corresponding displacements at corresponding points in the airplane analysis. Near the leading edge, where the two structures differ somewhat, forces rather than displacements were specified. The required loads were printed out by NASTRAN as "Forces of Single-Point Constraint." This process was carried out for both mechanical and thermal loadings and worked quite satisfactorily. The adequacy of this technique was established by analytical means and by running sample problems. It was shown that high precision was required for specifying the values of the displacements to obtain accurate forces.

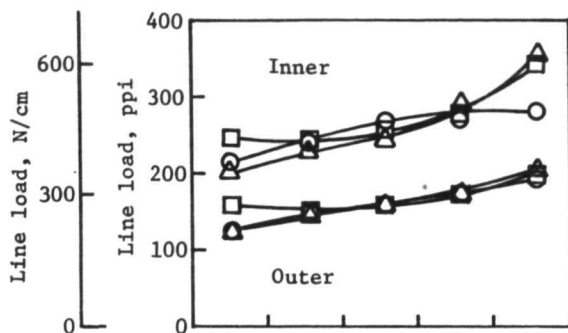
Interface spanwise shearing loads were not applied to the test structure. Therefore, in the NASTRAN run to determine loads, interface displacements in the spanwise direction were not prescribed. An additional NASTRAN run of the isolated wing section with the spanwise interface displacements prescribed established a modified set of loads that would be applied as spanwise and additional vertical loads.

The NASTRAN models of the wing and support structure were assembled and subjected to mechanical and thermal loading conditions with and without spanwise interface loads. It is found that, for this region of the wing, the spanwise interface loads were not very important for mechanical loading, but can be of great importance under typical thermal loading.

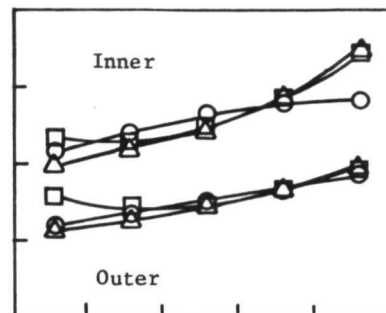
Panel axial loads, N_y , are given in figure 32 for mechanical and thermal load conditions. The inner panels are between BL 1.372 and 2.479 m (54.0 and 97.6 in.); the outer panels are between BL 2.479 and 3.586 m (97.6 and 141.2 in.). Three sets of curves are shown--one for the airplane, one for the test structure loaded at the existing load points, and one for loads at all interface load points. Mechanical loads were in good agreement for the three conditions. Thermal loads show a greater departure when comparing airplane and all interface with loads applied at the existing load points. The thermal agreement was best in the region from the forward cut section [FS 23.114 m (910 in.)] to about the center of the test structure. This lack of agreement was attributed to the fact that Y forces cannot be applied to the test structure. Additional normal load, in the Z direction, can be applied to increase the panel axial line loads.

Displacements in the wing test structure reference system were not numerically equal to the airplane displacement because of different reference systems; however, the agreement was quite acceptable once the rigid-body motions due to the different reference frames were taken into account. This agreement held true whether or not all interface loads were included.

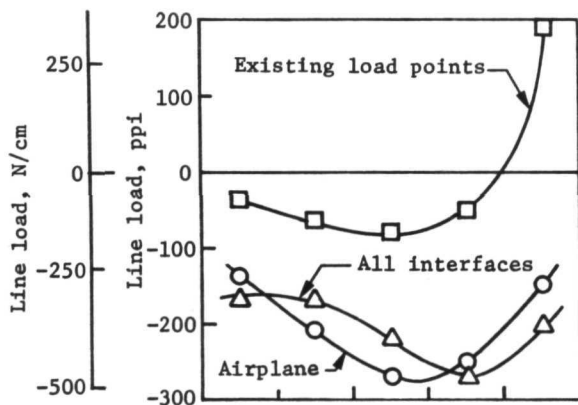




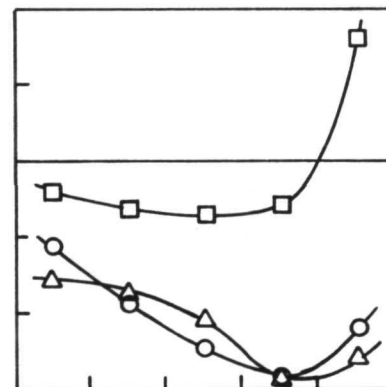
(a) Lower surface, mechanical



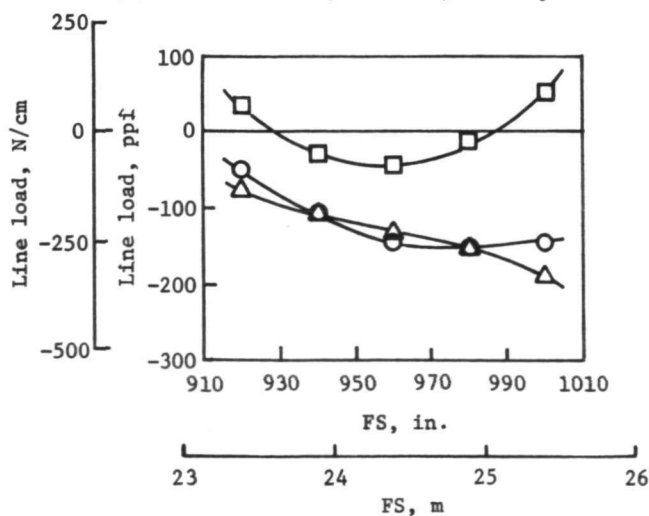
(d) Upper surface, mechanical



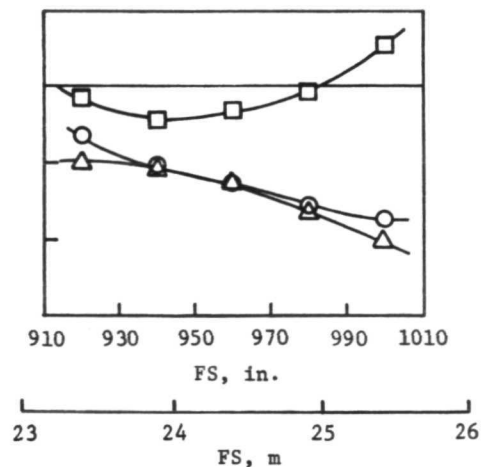
(b) Lower surface, thermal, inner panels



(e) Upper surface, thermal, inner panels



(c) Lower surface, thermal, outer panels



(f) Upper surface, thermal, outer panels

Figure 32 Panel Line Loads, N_y , for the Airplane and Test Structure

DETAIL DESIGN OF WING STRUCTURE

Beaded Panel Optimization

The beaded structural panels in the wing test structure are subjected to stresses resulting from both the temperature distributions and the mechanically applied loads. In flight, the structural panels of the airplane wing are subjected to normal loading resulting from aerodynamic pressure on the wing and aerodynamic heating.

The beaded structural panels were formed from René 41 sheet, 0.094 cm (0.037 in.) thick. This thickness included an allowance of 0.0025 cm (0.001 in.) for loss of metal resulting from oxidation. The computer program OPTBEAD, written for optimization of the airplane wing structural panels, was used for strength analysis of the beaded panels of the test structure and transition section.

A strength interaction curve of axial line load, N_y , versus shear line load, N_{xy} , is presented in figure 33 for the panel bead geometry used in the wing test structure. The panel has a 5.171-kN/m^2 (0.75-psi) ultimate venting pressure and is at a temperature of 1005°K (1350°F). The length was 1.107 m (43.6 in.) and the width was 0.508 m (20.0 in.). Margins of safety for ultimate loads are given in table VIII for the five panels shown in figures 31(a) and 33.

The interaction curve of figure 26 is for the critical panel in the airplane wing. The lightest weight was determined by the OPTBEAD computer program by selecting the optimum radius and thickness for the largest loads. A similar interaction curve is shown in figure 33 for the test structure panels. Requirements were imposed on the test structure panel beads to be symmetric (an odd number of beads) and to fit between the spar caps. These practical considerations resulted in small changes from the optimum geometry.

As discussed in the loads analysis section, the limited number of load points and directions for the test structure results in lower loads in some of the corresponding panels between the airplane and test structure. As shown by figures 26 and 33 the load distribution between panels is similar for both structures.

TABLE VIII ULTIMATE LOADS AND MARGINS OF SAFETY OF COMPRESSION
BEADED PANELS FOR COMBINED MECHANICAL AND THERMAL
LOADS, 2.5-g MANEUVER

Panel number	Ultimate load				Margin of safety from strength curve, figure 33
	Axial, N_Y		Shear, N_{XY}		
	ppi	N/cm	ppi	N/cm	
1	-531	-930	-111	-194	0.77
5	-560	-981	-117	-205	0.67
9	-611	-1070	-137	-240	0.50
13	-666	-1166	-172	-301	0.30
17	-690	-1208	-184	-322	0.24

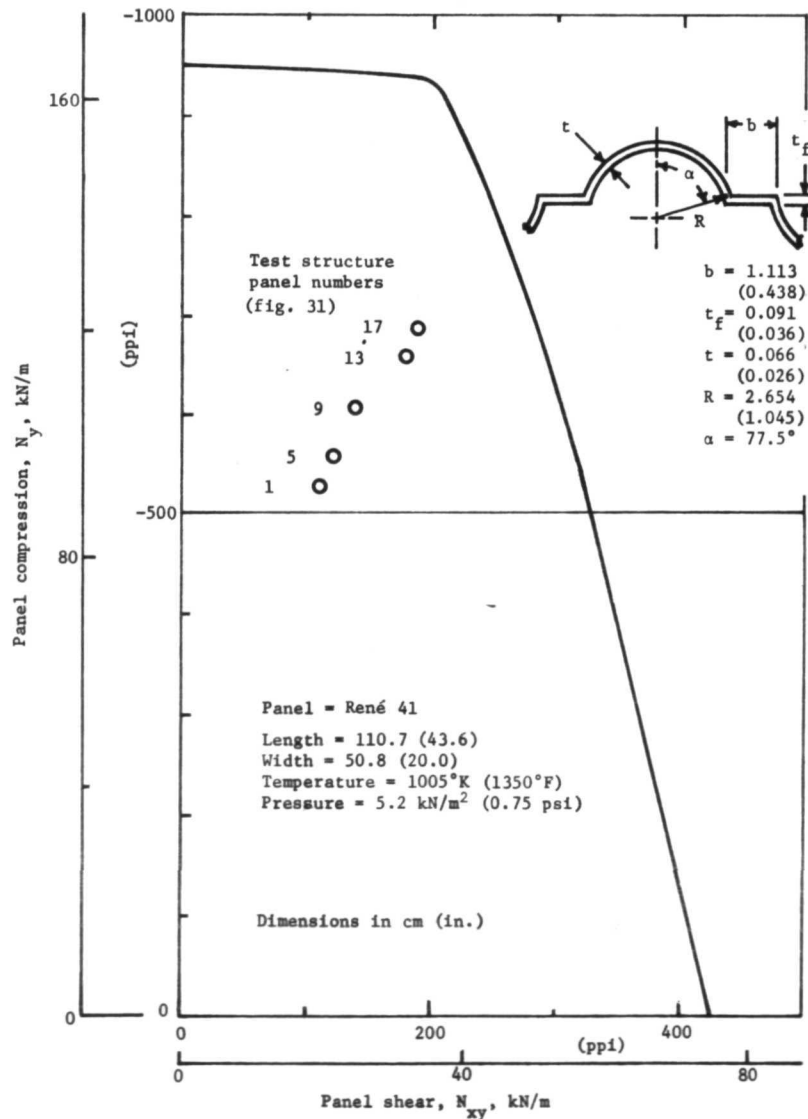
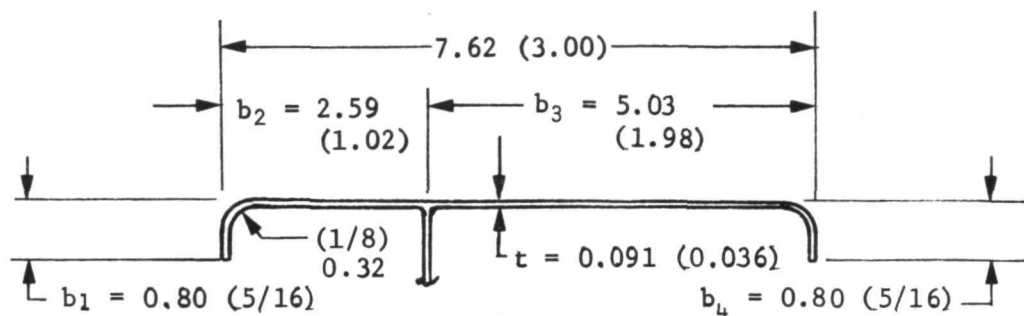


Figure 33 Strength Interaction Curve for Test Structure Panels

Caps

The rib and spar caps were channels formed of 0.091-cm (0.036-in.) thick René 41, with an additional 0.0025-cm (0.001-in.) thickness allowed for oxidation. The channel was 7.62 cm (3 in.) wide with flanges 0.794 cm (5/16 in.) deep, as shown in figure 34. The same cross section was used for all of the spar and rib caps. The rib caps were reinforced with panel and doubler edges. As required, splice straps of 0.160 or 0.091 cm (0.063 or 0.036 in.) thickness assisted in carrying loads across the intersections and along the caps.



Note: Dimensions in cm (in.)

Figure 34 Design Configuration of Rib and Spar Caps

Two cap positions were analyzed namely: rib caps and spar caps between intersections, and rib caps and spar caps at intersections.

Webs

The webs were designed to be flexible parallel to the rib and spar caps, stiff in the direction normal to the wing, and to resist shear loads in the plane of the spars or ribs. The flexibility

decreased thermally induced forces between the webs and the caps and panels. The optimum web configuration resisted the ultimate shear load with the least amount of material. The ultimate combined mechanical and thermal average shear stresses were low enough to be satisfied by the minimum thickness of 0.038 cm (0.015 in.)

Although the design specifies 0.041 cm (0.016 in.) metal thickness, including a 0.0025-cm (0.001-in.) oxidation allowance, the webs have a minimum thickness of 0.043 cm (0.017 in.) after stretch forming from 0.048-cm (0.019-in.) sheet.

Splices

The rib shear webs and the spar shear webs were attached at their intersections by four angle splices made of 0.076-cm (0.030-in.) thick René 41 sheet with 0.238-cm (3/32-in.) diameter rivets of HS 188. The angles were analyzed for ultimate margins of safety under interrivet buckling, shear buckling, net tensile strength, and bearing in rivet holes. The loads used in the strength analysis were the 2.5-g maneuver ultimate combined mechanical and thermal loads from the NASTRAN analysis of the test structure.

Heat Shields

Analysis was conducted for the heat shield panels, support beams, and flexible support clips. The surface panels were analyzed as overhanging beams having ultimate bending strength for René 41 at 1144°K (1600°F), and for TDNiCr at 1366°K (2000°F). An additional support beam was used for the TDNiCr heat shields due to the lower strength of the TDNiCr. Heat shield clips must be capable of resisting buckling as an Euler column and remain elastic when bent due to differential thermal expansion between the heat shield and the structural panel.

The René 41 and TDNiCr heat shield panels were analyzed for bending strength loaded by 5.171 kN/m² (0.75 psi) ultimate pressure. The ultimate stresses for a 0.025-cm (0.010-in.) thick panel stiffened by arcs of 3.28 cm (1.29 in.) radius were defined.

Fasteners

The structural beaded panels were attached to rib caps and spar caps with 10-32 Waspaloy screws spaced at 4.45 cm (1.75 in.). Screws were used rather than rivets to provide removable, replaceable panels and to permit inspection and access. The fasteners were in double shear along the ribs and carry relatively large spanwise loads across the rib joints. This was accomplished by the splice straps, without which the fasteners would be subjected to an unsymmetric single shear loading. The panel and doublers were sandwiched between the splice strap and the rib cap. The panel and doublers were sandwiched between the splice strap and the rib cap. The fasteners were in single shear along the panel edges that are attached to the spar caps. Because the beaded panels carry relatively low loads parallel to the ribs, splice straps were not required at the spar splices.

Four $\frac{1}{4}$ -28 Waspaloy bolts were used at the intersection of spar and rib caps. These connected the rib splice strap, the corners of the adjacent panels, and the spar and rib cap overlap.

TEST FIXTURE DESIGN

The hypersonic wing test structure has been designed for upside down testing so that positive upward lift forces on the airplane wing will be simulated, in general, by tensile downward loads on the cantilevered test structure, as shown in figure 35. The distributed wing loading will be approximated by concentrated loads at 18 spar-to-rib intersections as shown in figure 36. Concentrated vertical loads will be applied in pairs, by means of a whiffle tree (load divider) and a single hydraulic actuator applying the load to each pair of wing load points. It is, of course, desirable to have as large a number of wing load points as practical to simulate the distributed flight aerodynamic lifting forces.

Holes in the rib and spar webs for instrumentation leads throughout the structure and for access to instrumentation are shown in figure 35.

Support Test Fixture

The test structure was cantilevered from a steel support test fixture which was composed of structural steel truss members. The test fixture is shown in figure 35. The steel support structure was made up of steel angles that were bolted to form a truss assembly. The back-to-back angles of the assembly were attached to structural tee sections that were bolted to the floor of the test facility.

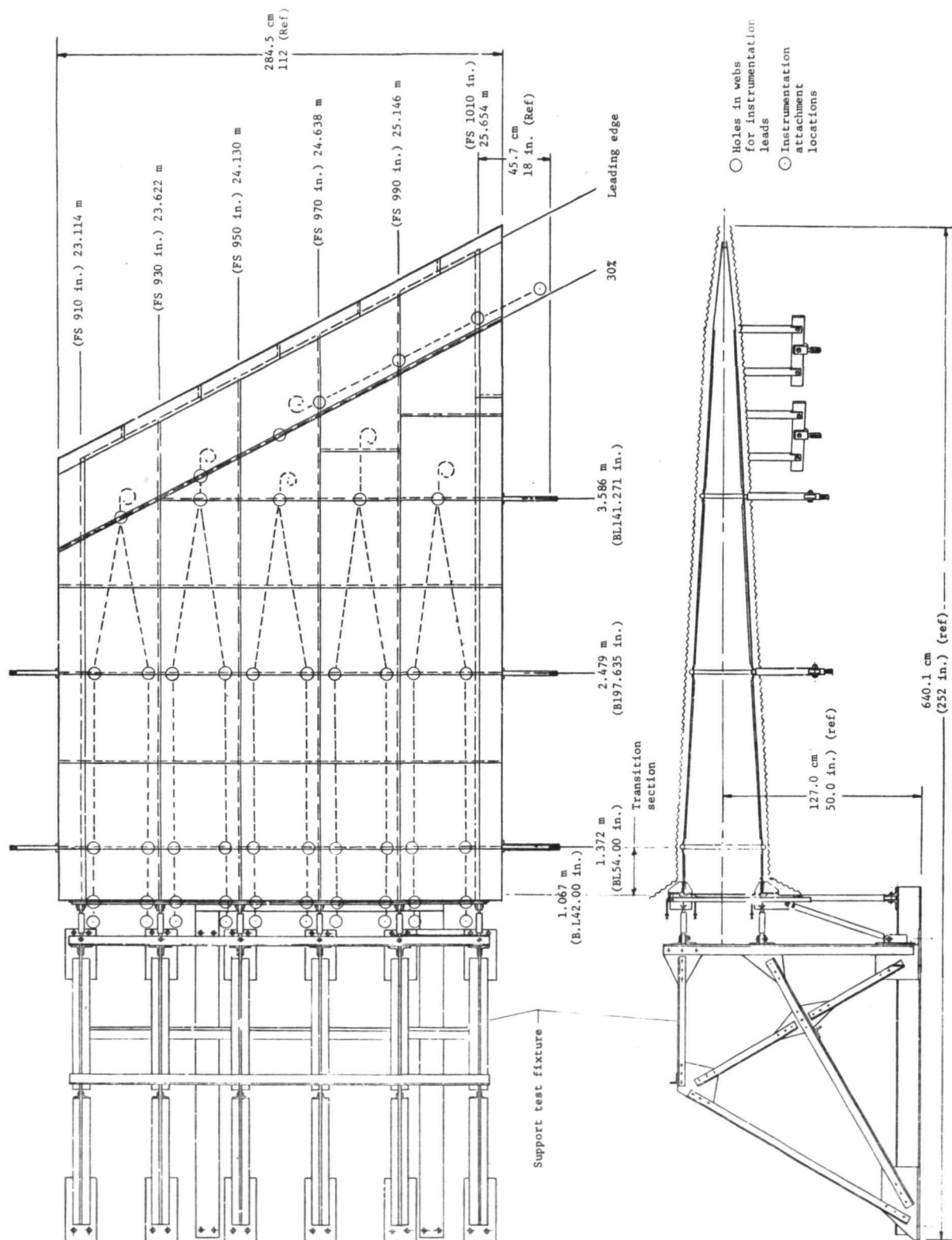


Figure 35 Test Structure Installation, Hypersonic Wing

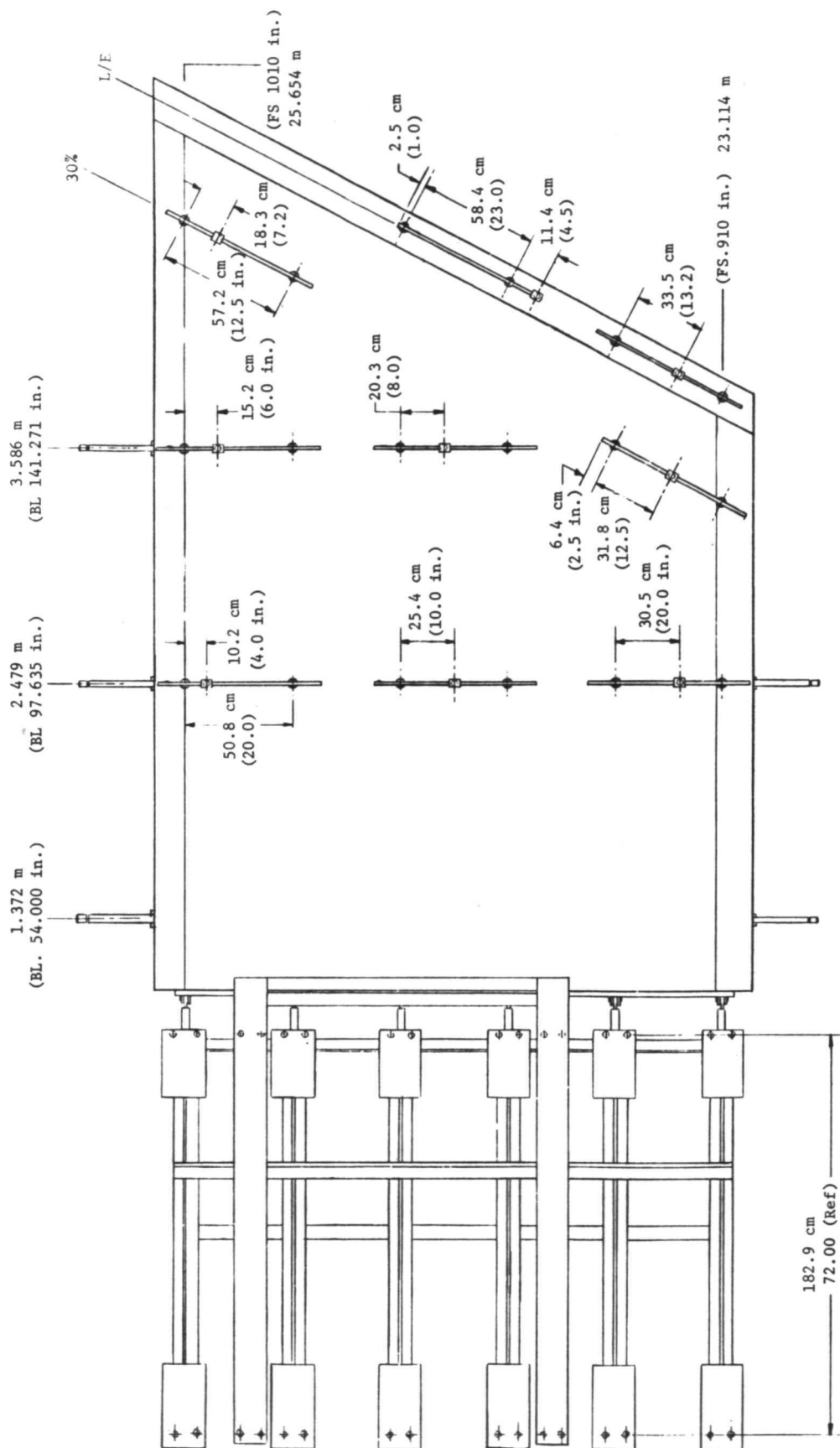


Figure 36 Loading Points for Wing Test Structure

Transition Section

A 30.48-cm (12-in.) long transition section between BL 1.372 m (54 in.) (wing/fuselage intersection) and the steel test support structure provided simulation of the wing carrythrough structure as shown in figure 35. The transition section also served as a thermal buffer zone between the hot wing structure and the cooled fittings attached to the steel support fixture. Stiff crossbeams at the inner edge of the transition region [at BL 1.067 m (42 in.)] diminished the tendency for structural panels to scallop from large concentrated reactions between the steel support structure and the inboard ends of the spar caps.

Ball-Ended Linkages

The inner ends of the 12 spar caps were attached to ball-ended horizontal linkage bars that carry only axial loads. The wing bending loads and certain thermally induced loads were reacted by these links. These links can be adjusted to length because they are turnbuckles. Vertical shear loads at BL 1.067 m (42 in.) were reacted by six diagonal ball-ended links that extend from the lower spar caps to the base of the steel support structure. These diagonal linkages were also adjustable for length by their turnbuckle construction. The single fixed point of the entire test structure was at the lower linkage intersection at BL 1.067 m (42 in.) and FS 24.638 m (970 in.) The net fore-and-aft loads on the test structure were reacted by two diagonal drag struts attached to the floor and to the fixed point.

If the test structure were uniformly heated, all points would expand away from this fixed point.

The ball-ended links between the support structure and the test structure permit free thermal expansion of the transition section, in the fore-and-aft direction, without constraint from the steel support structure. Because the relatively stiff support structure will be at room temperature, there could be severe thermal forces between the hot wing and the cold support structure if such freedom of movement were restricted.

Because the total thermal expansion of the inner edge of the transition region will be relatively large, the ends of the links were spaced farther apart at the steel support structure than on the wing. The amount of excessive spacing was one-half of the

thermal excursion predicted by NASTRAN analysis, of the test assembly, for the thermal condition. This procedure limited approximately half their maximum value.

Thermal Protection

Because the transition structure at BL 1.067 m (42 in.) will be at an elevated temperature, relative to the steel support structure, provisions were made to protect the ball ends of the links and other steel parts that will be at room temperature. Stainless steel fitting assemblies were bolted rigidly to the transition structure at BL 1.067 m (42 in.) and were the wing attachment points for the ball-ended linkages.

The stainless steel fittings were recessed around the bolting bosses to minimize the thermal contact area with the hot René 41 transition structure. The fittings were provided with water cooling passages so that the heat will be carried off in the coolant rather than being absorbed by the steel support links.

A Cera Felt insulation blanket between the transition structure and the steel support structure protects the steel structure.

Vertical Load Application

The vertical loads, simulating aerodynamic lift on the wing, will be applied through bayonet-type Inconel 718 fittings. The rib and spar load fittings were rigidly bolted under the rib and spar intersection by four 0.635 cm ($\frac{1}{4}$ in.) bolts that pass through the rib and spar caps, the panels, the panel doublers, and the splice strap that runs along the rib cap. A 1.429-cm (9/16-in.) diameter cross pin fits into the slotted end of the loading bar. The slotted end of the Inconel 718 loading bar is placed over the wing fitting and rotated until the cross pin fitted into the cross-drilled recess. The other end of the loading bar straddles and is bolted to one end of the whiffle tree.

Horizontal Load Application

Horizontal loads were applied to the foreword and aft ends of the rib caps at the edges of the test structure at BL 1.732, 2.479, and 3.586 (54, 98, and 142 in.). The directions of the loads were along the rib caps. The Inconel 718 load bar assemblies were used.

Each flat plate was attached to the test structure by six 0.635-cm ($\frac{1}{4}$ -in.) Waspaloy bolts. The bolts pass through the spade-shaped horizontal load fittings, through the spacers below the load fittings, and through the caps of the short extensions of the ribs. The load bar assemblies will be always aligned with the rib caps because of the rigid bolted joint.

WING TEST STRUCTURE FABRICATION

GENERAL APPROACH

A complete test specimen representative for the test area of the wing and consistent with the established design was constructed as shown previously in figure 6. To initiate the fabrication activity, the established wing test structure design was used to define the logic flow diagram of figure 37, which depicts the general fabrication sequence from start of tooling and details through final assembly.

The sequence of manufacturing operations of figure 37 was generally set up to do the forming earliest so that all formed details such as beaded panels, heat shields, and rib/spar webs would be available for work phasing into subassemblies. At the same time, details such as clips, angle brackets, tie straps and spacers were being made in detail and stocked for further assembly work. As fasteners such as nut plates became available, nut plate strips were punched and nut plates were spot welded into nut plate subassemblies that were later installed to rib and spar caps in final assembly.

Several critical manufacturing operations in terms of schedule were defined and among these were the fusion welding of rib and spar caps and the spot-welding operations that were to be performed on beaded panel assemblies, heat shield assemblies, and nut plate strip assemblies. In addition, chemical-milling operations were reviewed in favor of more reliable stock control methods and scheduling. This was achieved by the decision to manufacture doublers using electrical discharge machining methods. Thus, the chemical milling of the webs of the standoff clips proceeded normally and no delays in assembly were experienced.

The fabrication effort was based on the technology developed during the activities as reported in Appendix A, Beaded Panel Tests, and Appendix B, Joint Tests.

TOOLING

The general approach for tooling was to make as much use of such standard tools as brakes, machine tools, shears, and forms as was possible to accurately manufacture the hardware. However, certain specific cases demanded designing and building tooling to make the configurations of unusual shapes and/or operations. Many of these, such as the welding fixture for the sinewave welding and the forming dies for the beaded panels and heat shields, were of a complicated nature and of multiple use variety.

The following tooling requirements were identified:

- 1) Tools to make details;
- 2) Subassembly tooling;
- 3) Final assembly tooling.

Tooling for Details

While many of the details used on this program were made directly from sheet stock by shearing and cutting processes, there were a great number of details that required tooling either because of the quantity or the precision involved. As an example, a special tool was made to dimple René 41 washers that were used on the TDNiCr leading edge heat shield. These washers were not required until it was found that TDNiCr could not be sufficiently dimpled to allow insertion of the heat shield countersunk fasteners. Special tools of this kind were used extensively throughout the detail phase of the program.

Subassembly Tooling

The subassembly tooling operations for the most part were for the beaded panels, heat shields, and spars and ribs.

A typical forming die for the beaded panels, shown in figure 38, was made from 7075 aluminum. The varied beaded length panels were formed in the standard beaded panel dies using fiberglass inserts as shown in figure 39. The tooling of figure 40 was used to make steps and cutouts for the doublers that were used at the ends of the beaded panel assemblies.

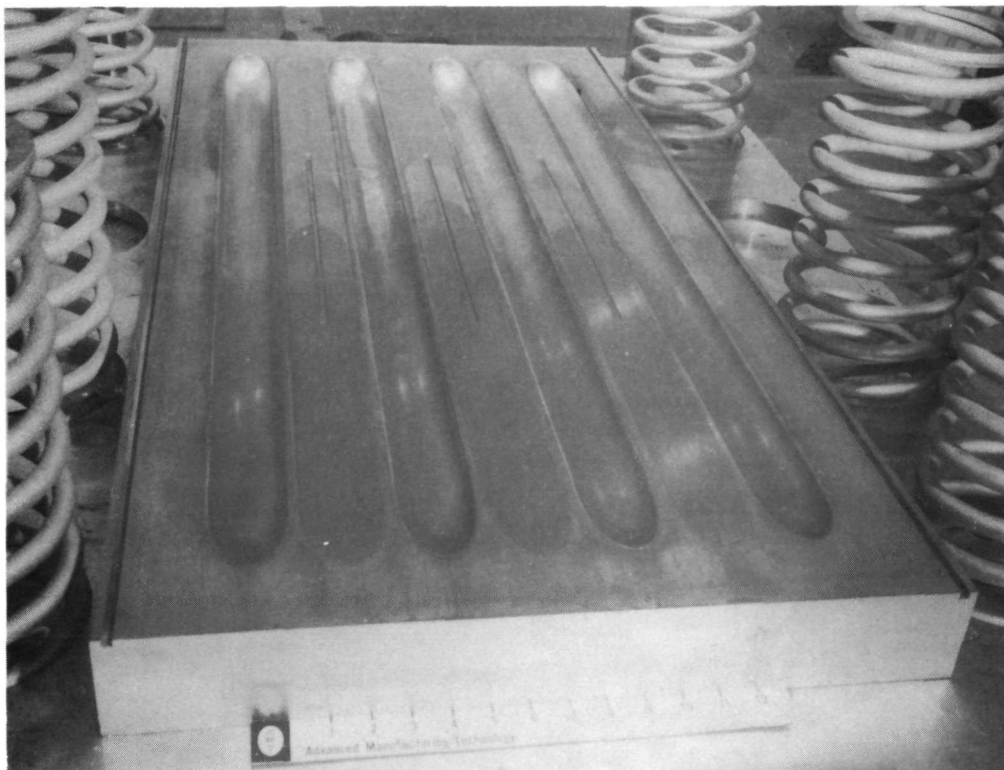


Figure 38 Lower Half of Aluminum Beaded Panel Forming Die Showing Stripper Springs

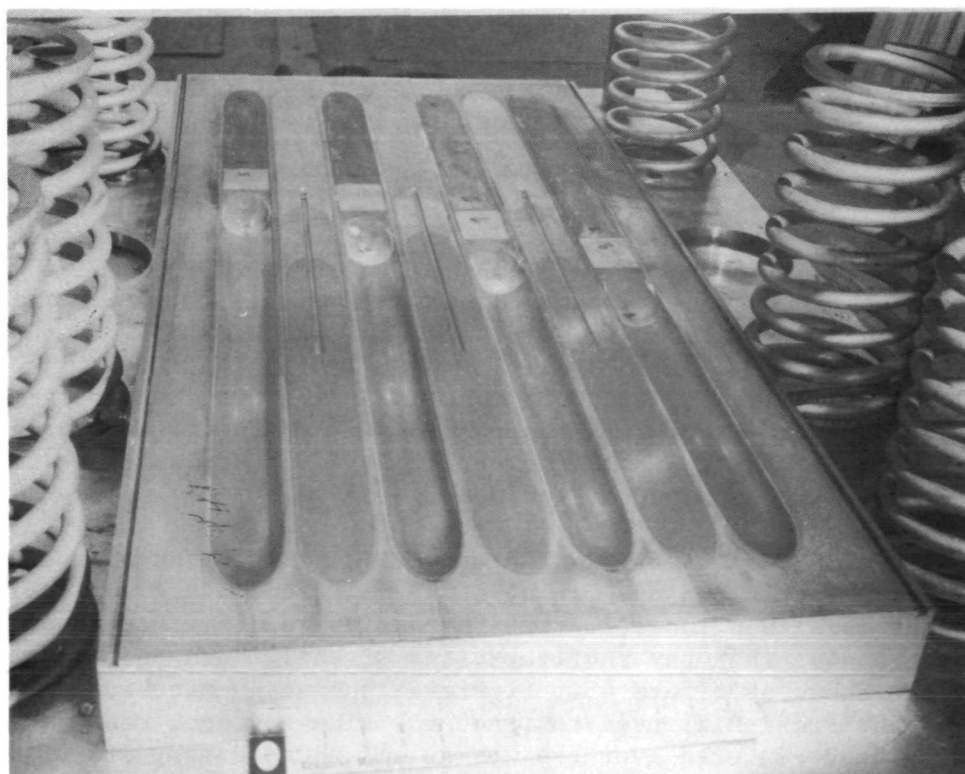


Figure 39 Plastic Inserts Installed to Form Different Length Beads

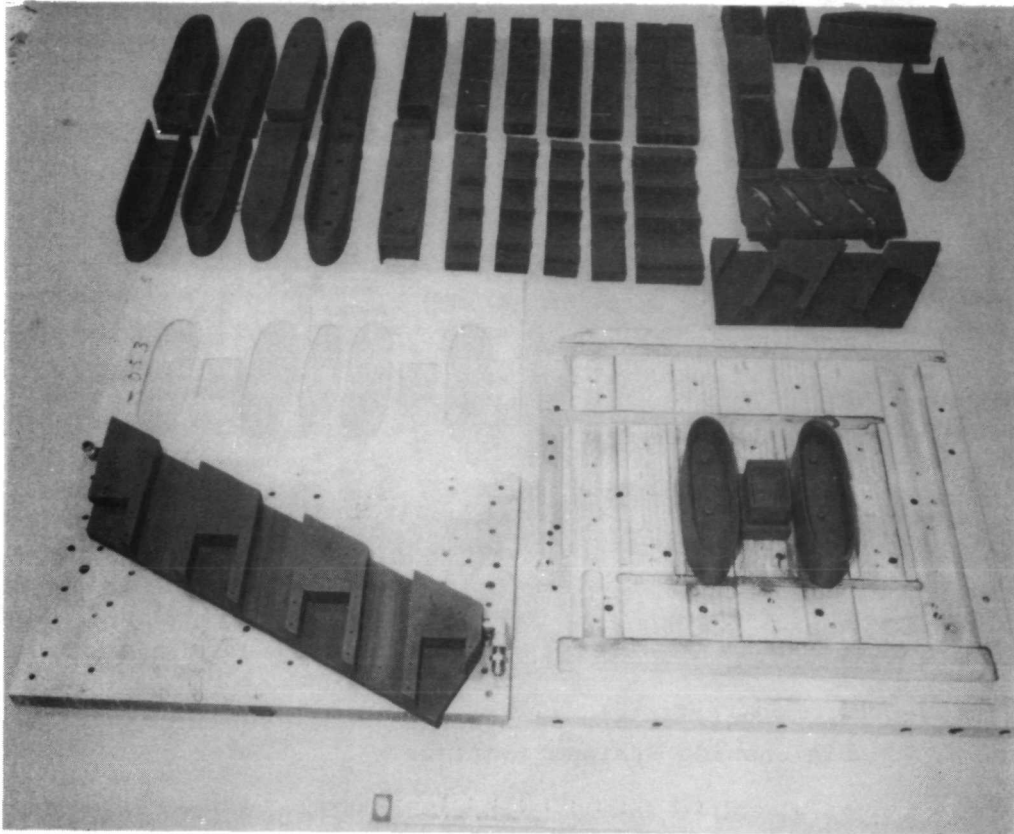


Figure 40 EDM Graphite Electrode Tooling and Tool Mounting Plate Used to Machine Steps on René 41 Doublers

The tooling of figures 41 and 42 was used to form the heat shield configurations. Figure 41 shows the machined closed-beads on the left-hand end of a die, and figure 42 indicates the right-hand end of a die fitted with fiberglass inserts.

The forming die of figure 43 was used for stretch forming the webs for the spars and ribs. The forming die was adaptable to forming webs of several configurations; however, only one configuration was used for this program.

The variety of configurations required for rib and spar assemblies necessitated the making of 79 different pieces of tooling that were then inserted into the master weld fixture shown in figure 44. The many configurations of chill bars and backup bars are shown as figure 45. Figure 46 shows the tracking mechanism of the Profi-Mill used to trace the sinewave web, keeping the welding head centered over the web at all times during its travel along the length of the rib or spar being welded.

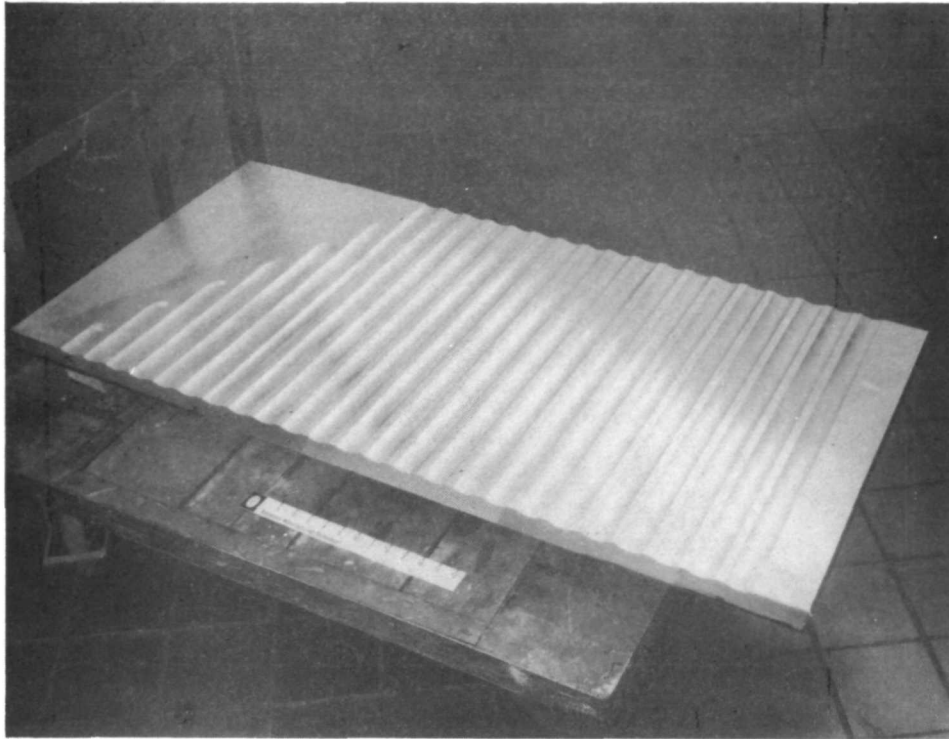


Figure 41 Heat Shield Forming Die Showing Machined Closeout Dimpled Corrugation Termination

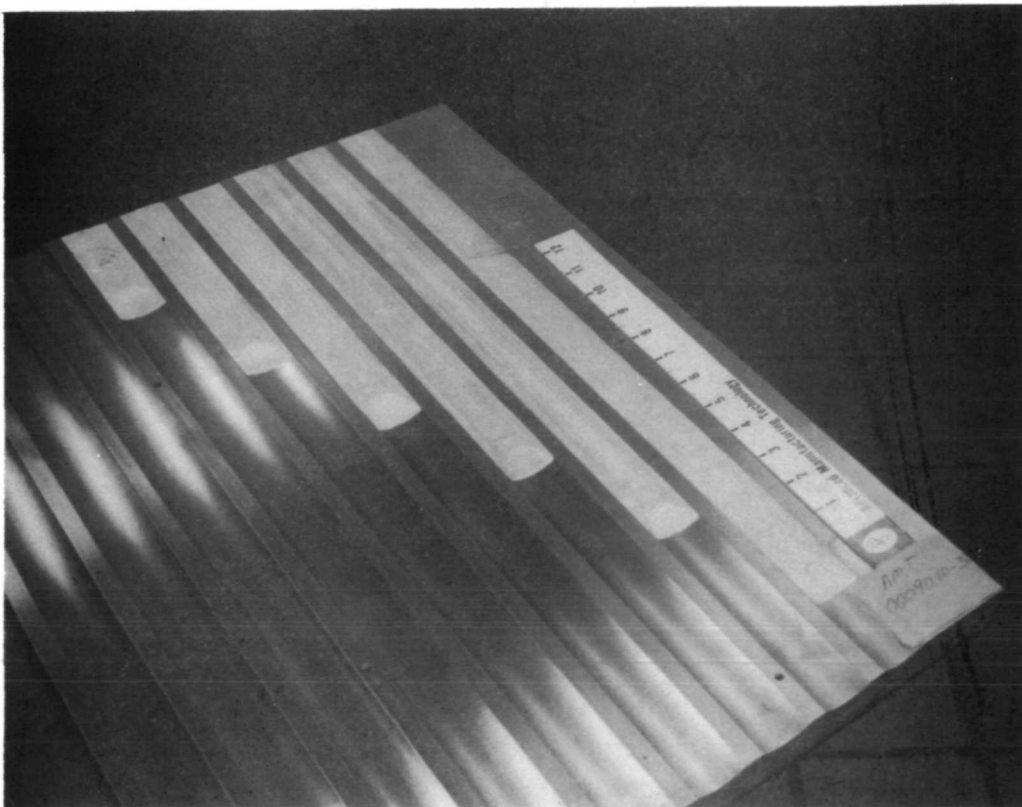


Figure 42 Heat Shield Forming Die with Fiberglass Inserts

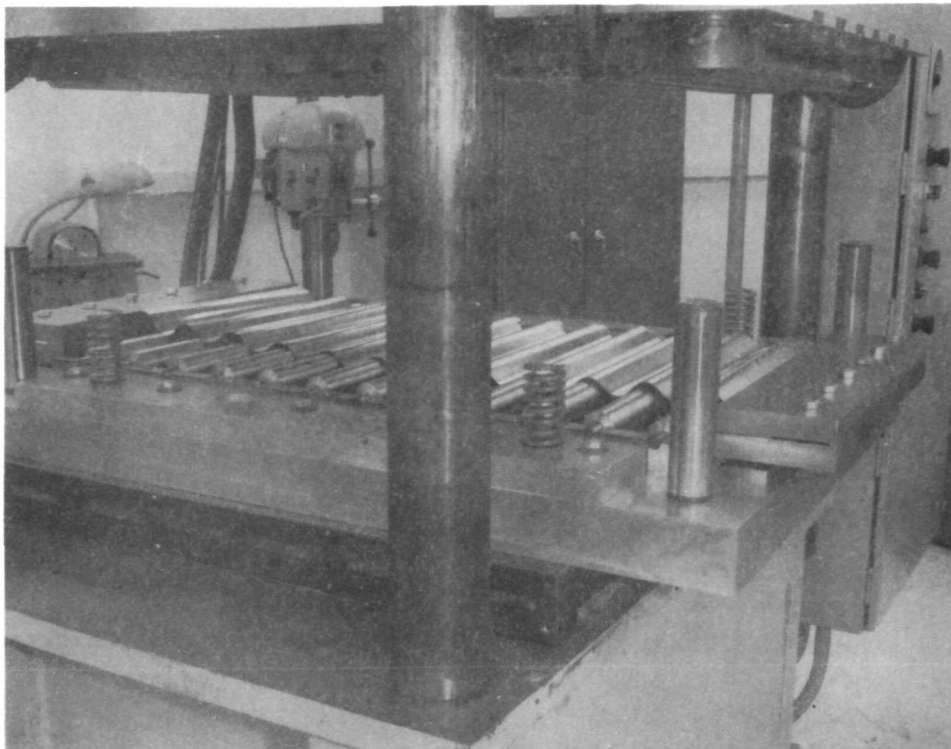


Figure 43 Bottom and Top Half of the Web Forming Die Set in a 100-Ton Dake Press, with Formed Piece on the Lower Die

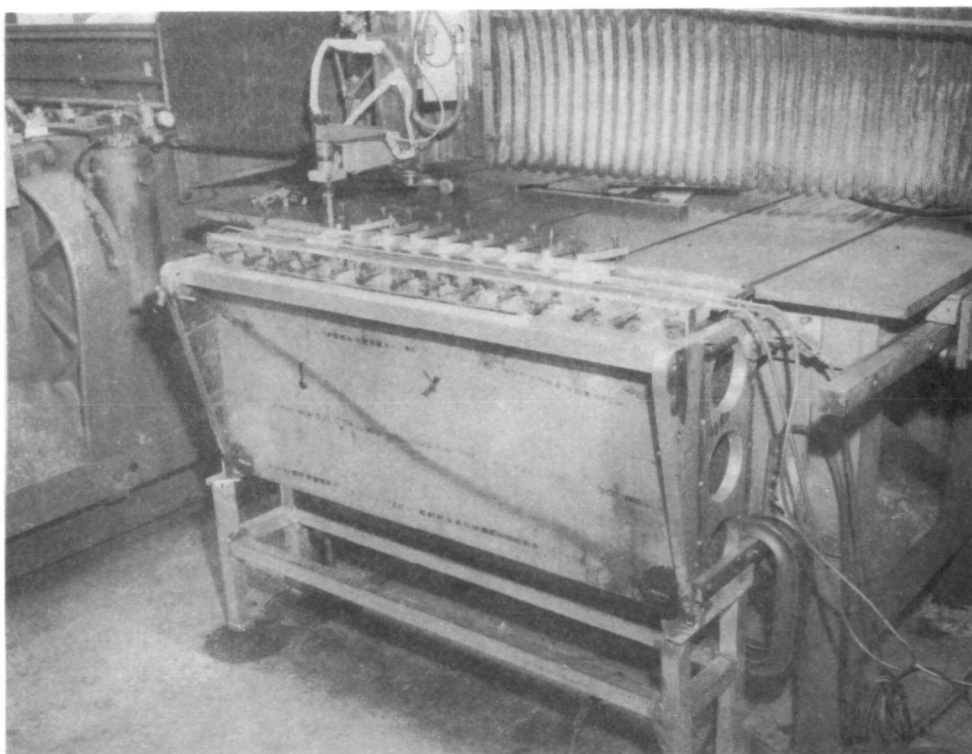


Figure 44 Master Weld Fixture for Rib Spar Assemblies Shown Ready to Weld

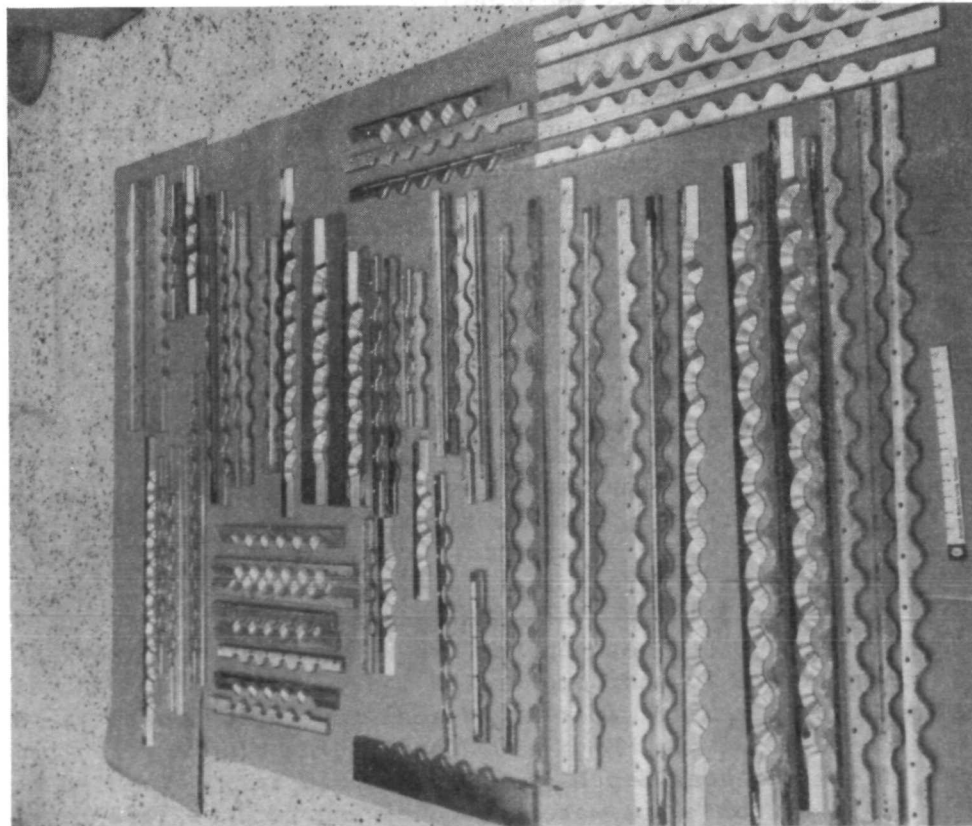


Figure 45 Assortment of Chill and Backup Bars to Make Various Rib and Spar Sub-assemblies for Master Weld Fixture

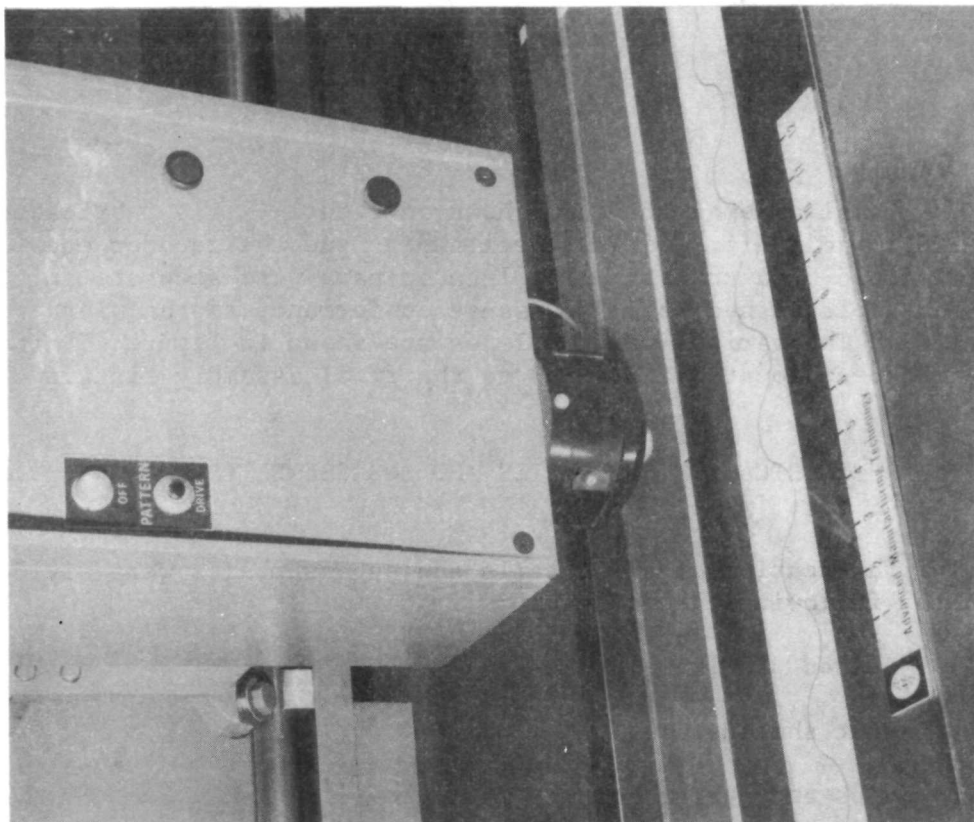


Figure 46 Optical Line Tracer Template Set Up for Precision Sinewave Weld (Note the sinewave line replica tracing and a cap blank at the lower end of the figure.)

Final Assembly Tooling

The final assembly fixture shown in figure 47 was fabricated from 10.16-cm (4-in.) square steel tubing and the locator pads were located by a transit. The locator pads were accurate in the three planes necessary to assure conformance to the wing geometry. The various station lines are shown in figure 48 after they had been located and fixed to the final assembly fixture.

FABRICATION OF DETAILS AND SUBASSEMBLIES

The fabrication of all details and subassemblies were divided into the following categories.

- 1) Beaded panels;
- 2) Heat shields;
- 3) Ribs and spars;
- 4) Details (clips and angles).

Final assembly operations were coordinated with the detail and subassembly manufacture, and many subassemblies and details could not be completed until they were matched to the final assembly. This included the drilling of holes that were required to be matched on final assemblies and the trimming to exact size of some details and subassemblies that were required to fit a precise location in final assembly.

Beaded Panels

Figure 49 is a manufacturing flow diagram of the operations required to fabricate the beaded panels. A total of 53 panels were required for the final assembly. In addition, a quantity of deliverable spares was also fabricated at the same time.

The beaded panels were formed using a 22-MN (5×10^6 -lb) Baldwin Universal Test Machine as a holding device for the die. The blanks were placed between the two 7075 aluminum forming dies as shown in figure 50 and compression loaded to machine capacity. This load caused a near water-tight seal for the hydrostatic forming operation at 34.475 MN/m^2 (5000 psi). The blanks were formed to 68% of maximum bead depth [1.615 cm (0.636 in.)] annealed at 1340°K (1950°F) for $\frac{1}{2}$ hr, water quenched and reformed, as required.

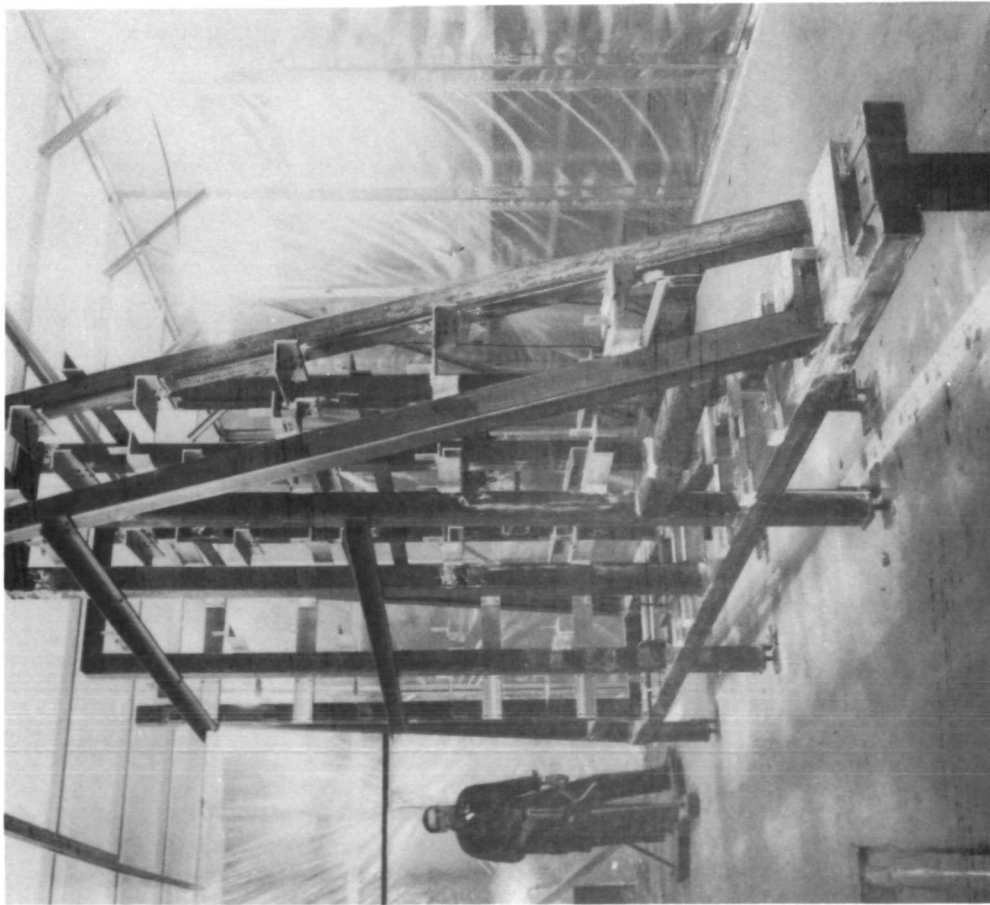


Figure 47 Final Assembly Fixture Structure Looking at Station and Butt Line Jig Points of Lower Wing Surface as Viewed from the Leading Edge Outboard

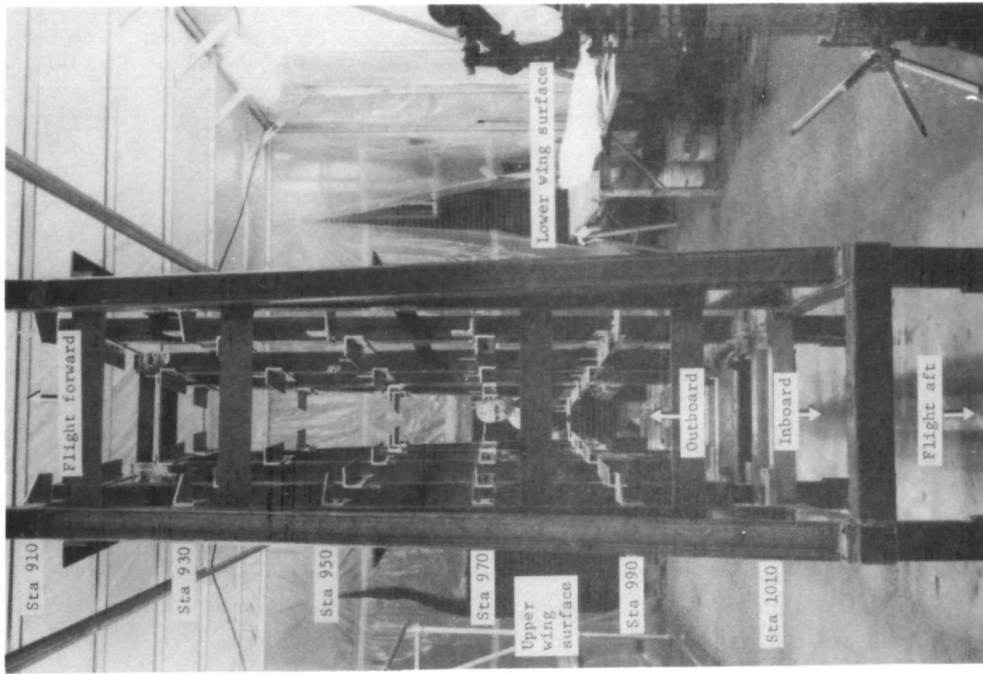


Figure 48 Final Assembly Fixture Structure Looking at Station Plane Locations as Viewed from the Inboard Section

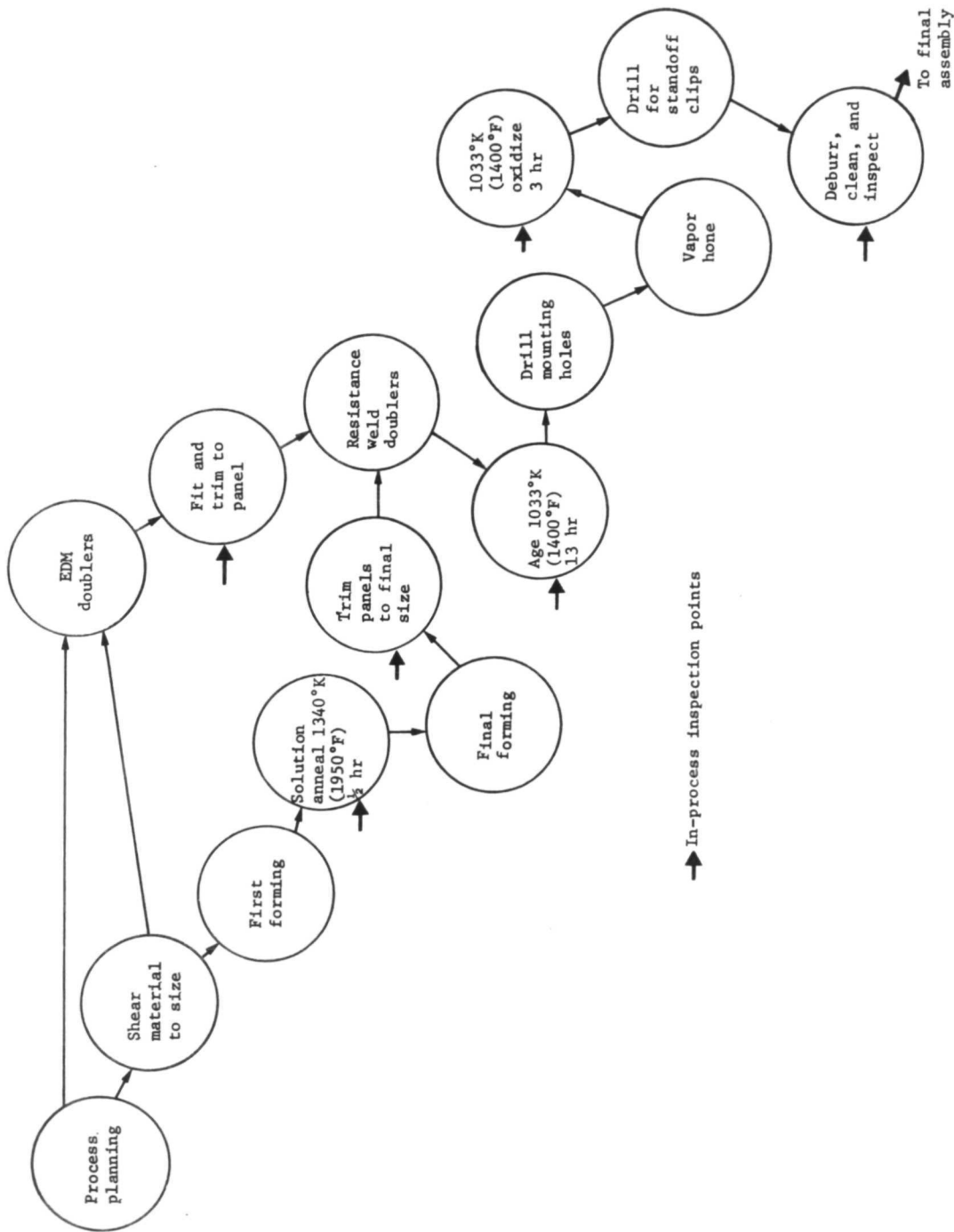


Figure 49 Manufacturing Flow for René 41 Beaded Panels

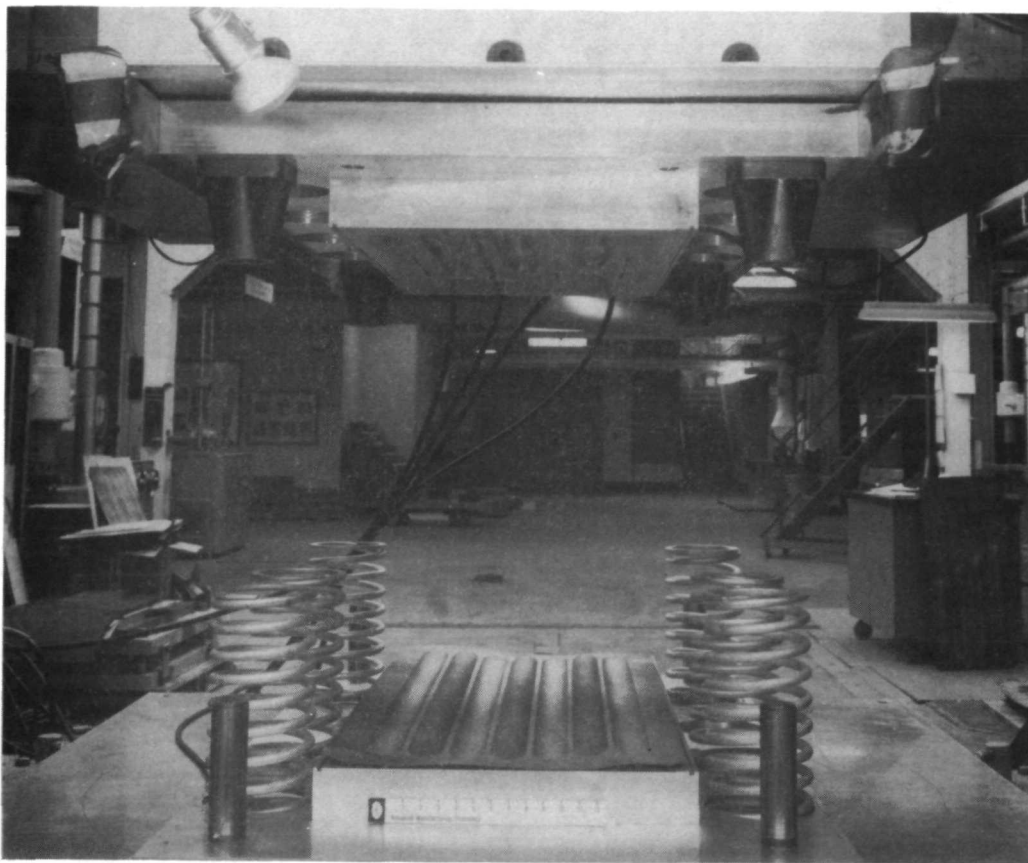


Figure 50 Beaded Panel Forming Die in 22-MN (5×10^6 -lb) Press

Doubler geometries such as those shown in figure 51 were typical for the rectangular panels. The setup for spot welding the doublers to the panel is shown in figure 52. Each spot was laid out on the doubler before welding. After spot welding, the panels were aged. Attachment of heat shield clips to the completed panels is shown in figure 53.

Heat Shields

The manufacturing flow for the heat shields is indicated in figure 54. The design of the wing required that 72 heat shields be manufactured for the wing and transition section with an additional 42 heat shields manufactured for the extensions on the periphery of the wing. The heat shields and extensions were made from René 41 except for five leading edge panels on the lower surface of the wing, which were made from TDNiCr.

Figure 55 shows a René 41 panel lying on top of a form die. The rubber forming pad for René 41 was two pieces of 2.858-cm (1.125-in.) thick butyl rubber sheets with a durometer hardness of Shore A-78.

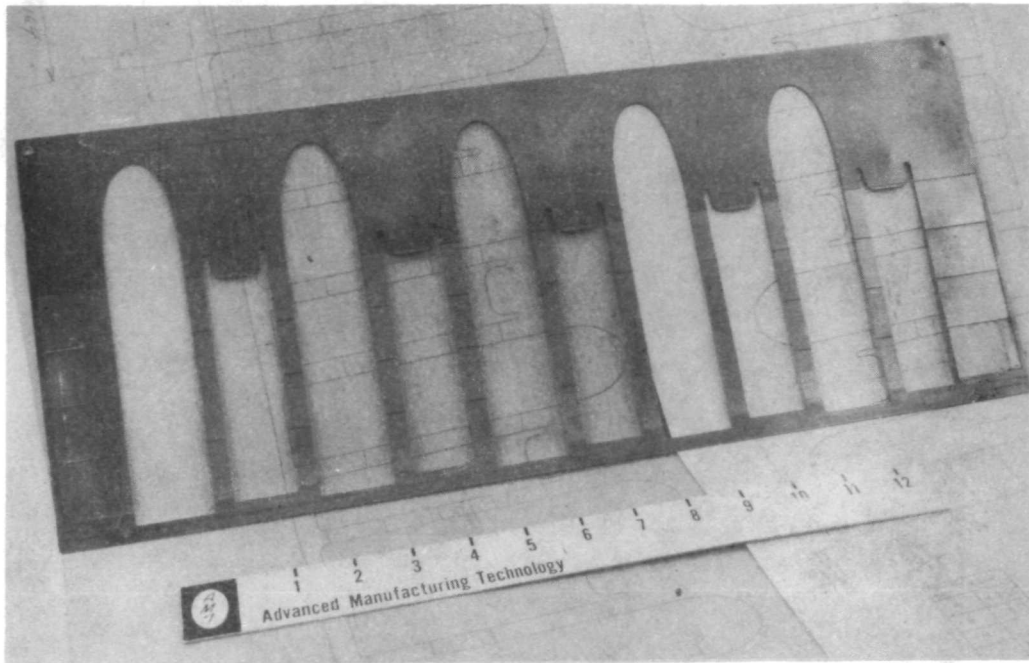


Figure 51 Doubler Stepped Thickness Obtained by EDM Operation
(Part shown is not trimmed.)

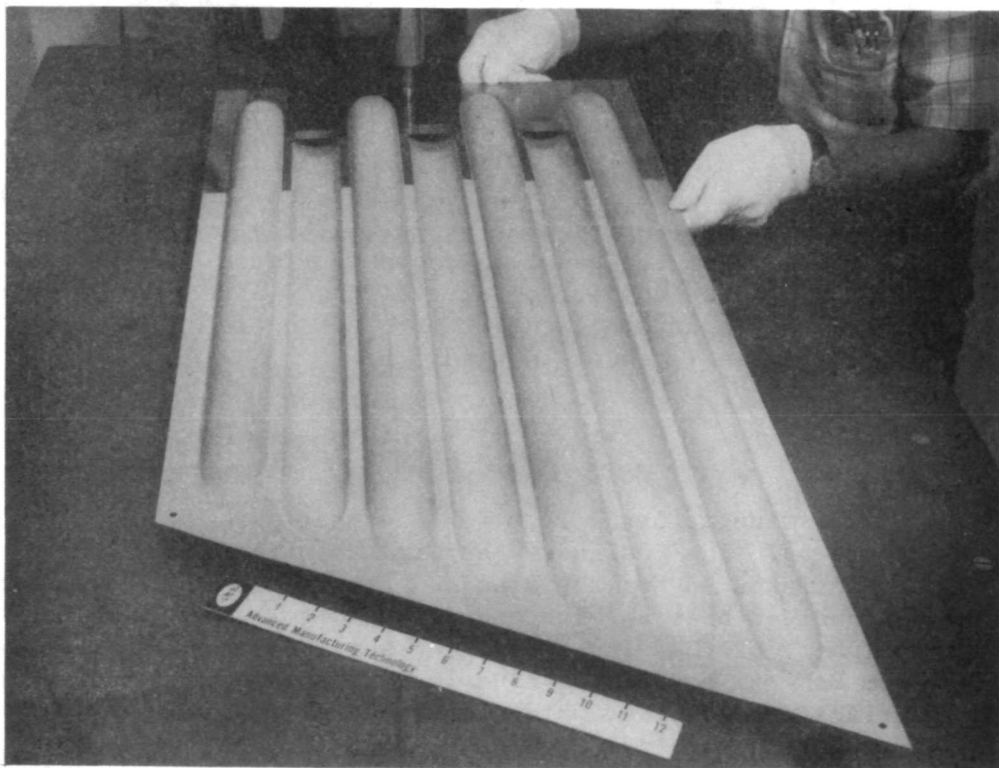


Figure 52 Spot Welding of Doubler to Beaded Panel

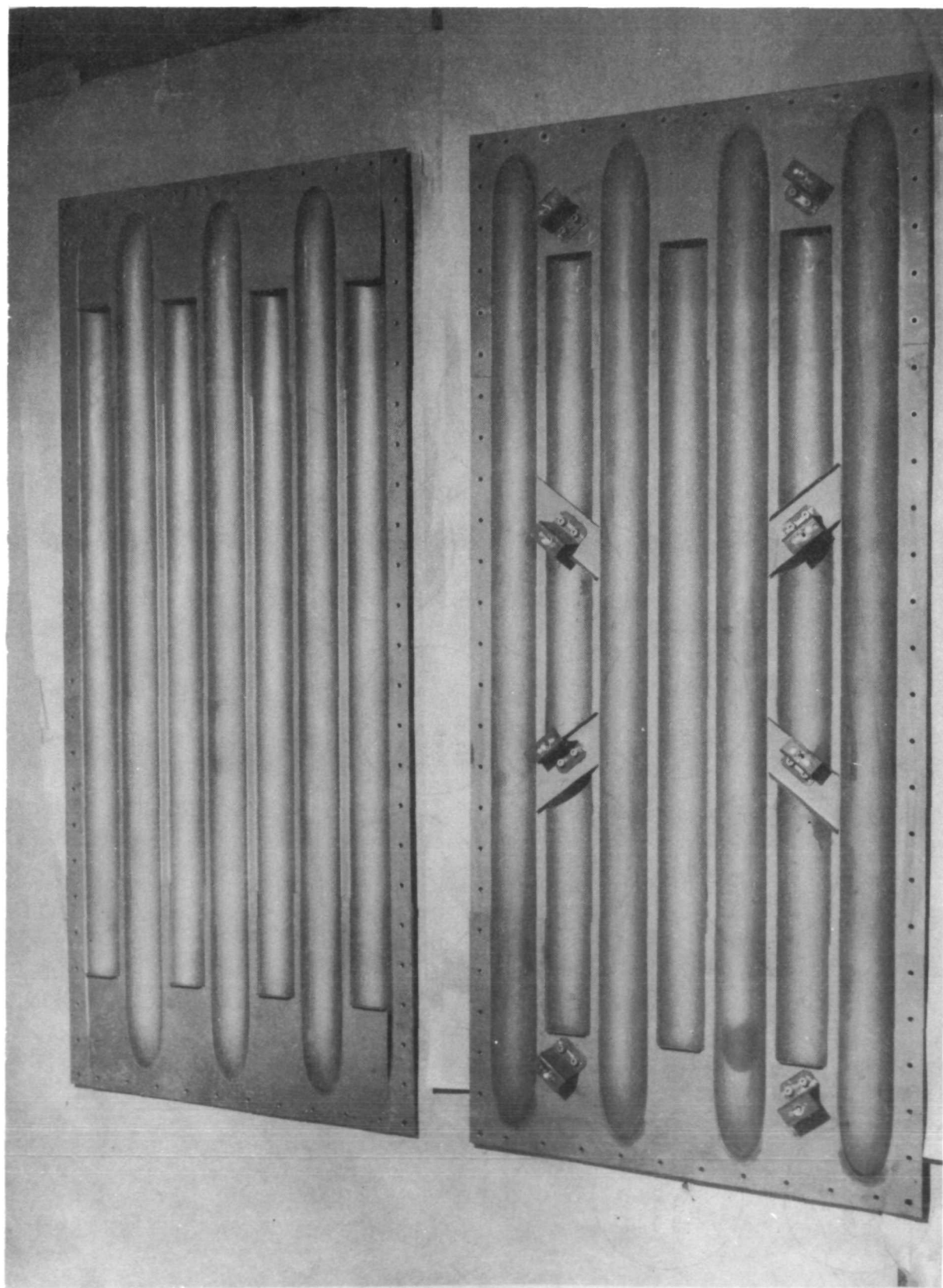


Figure 53 Heat Shield Standoff Clips in Position on the Beaded Panel

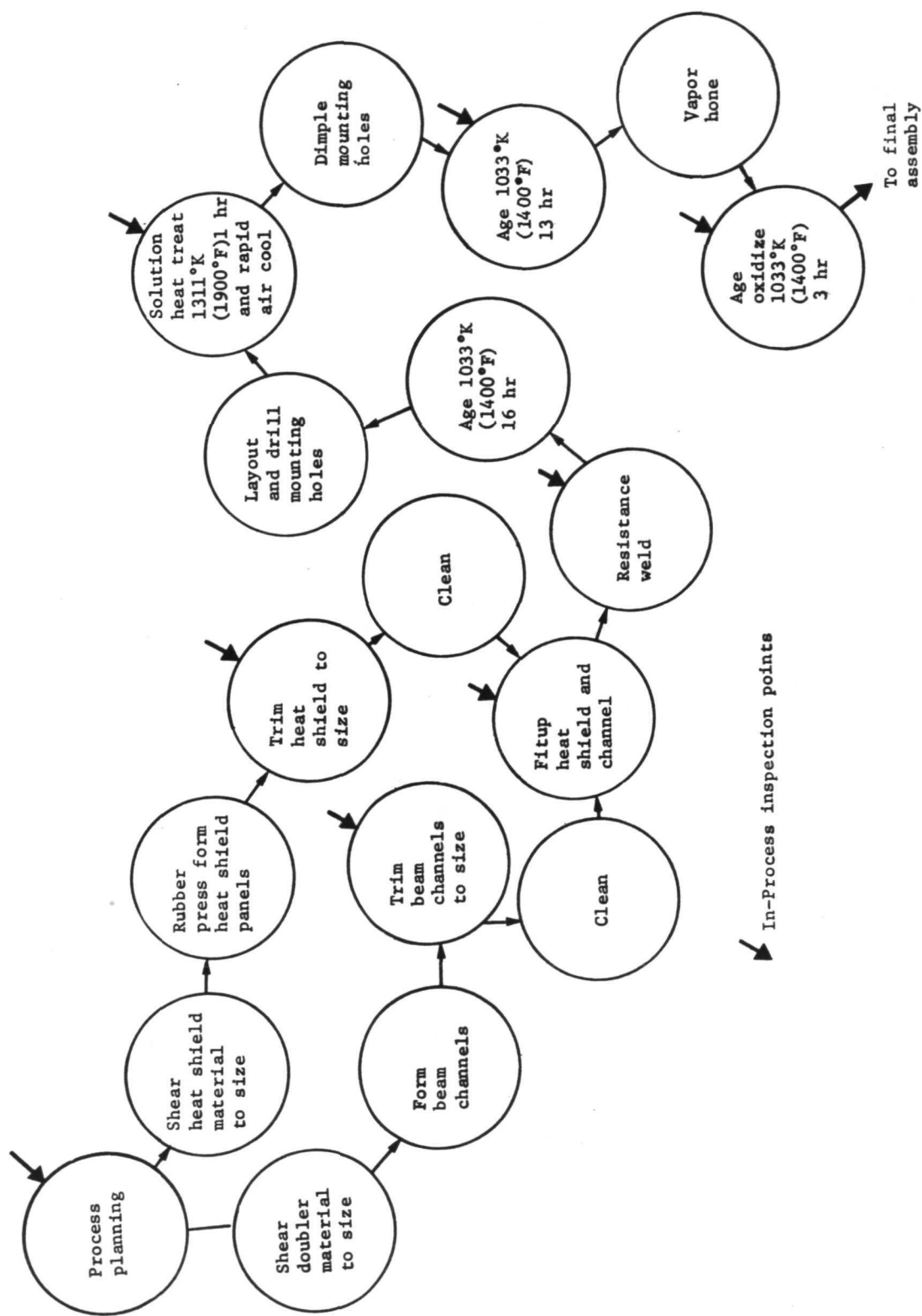


Figure 54 Manufacturing Sequences to Produce Heat Shield Assemblies

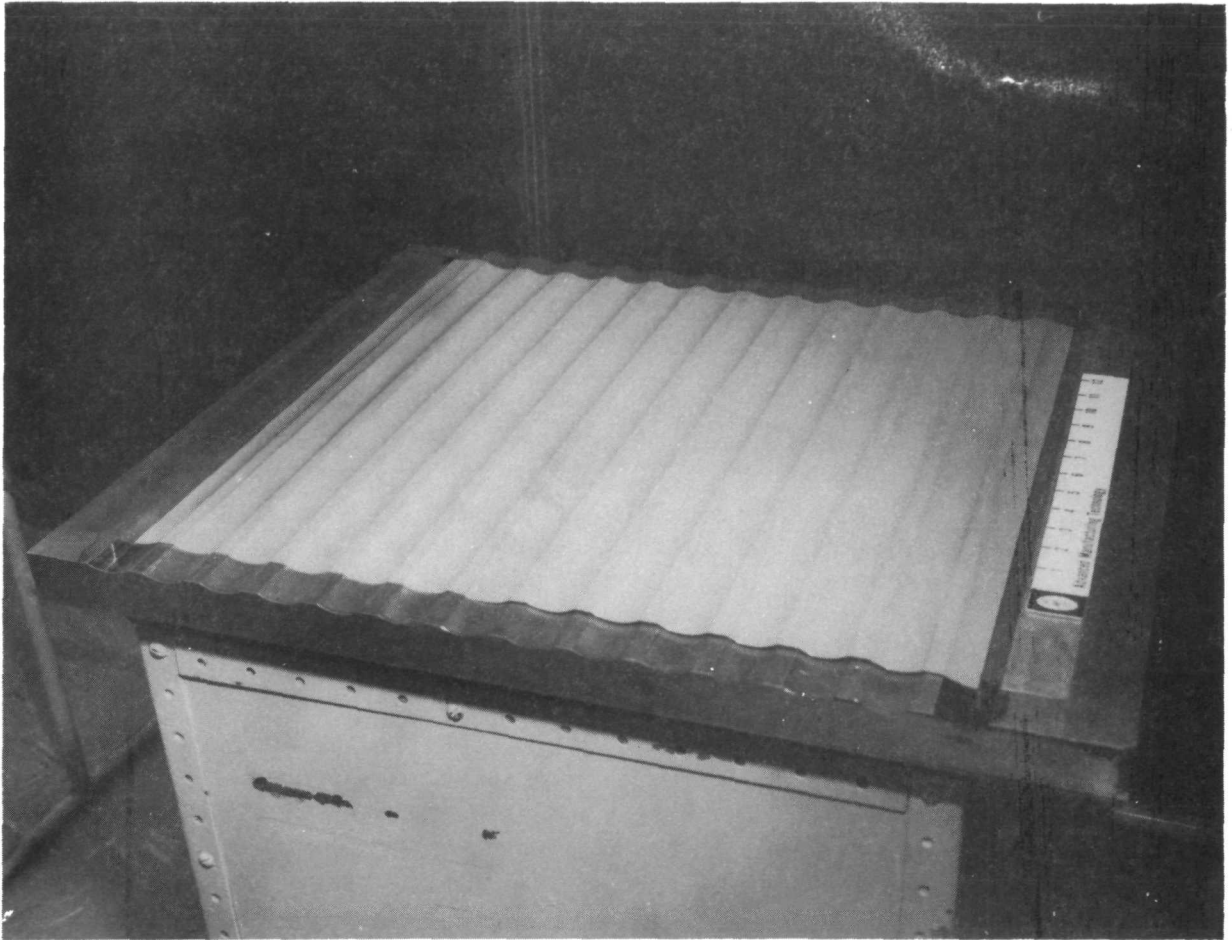


Figure 55 Formed Heat Shield in Forming Die

A typical completed René 41 heat shield (with oxidation treatment) is shown in figure 56.

Completed TDNiCr heat shields are shown as figure 57. The seam where the blanks were welded together is plainly visible. Welding was required to form pieces large enough to be heat shields because the available material was not wide enough. Thorough visual inspection of these welded seams revealed no cracking, nugget separations, or tearing of the material in the formed parts.

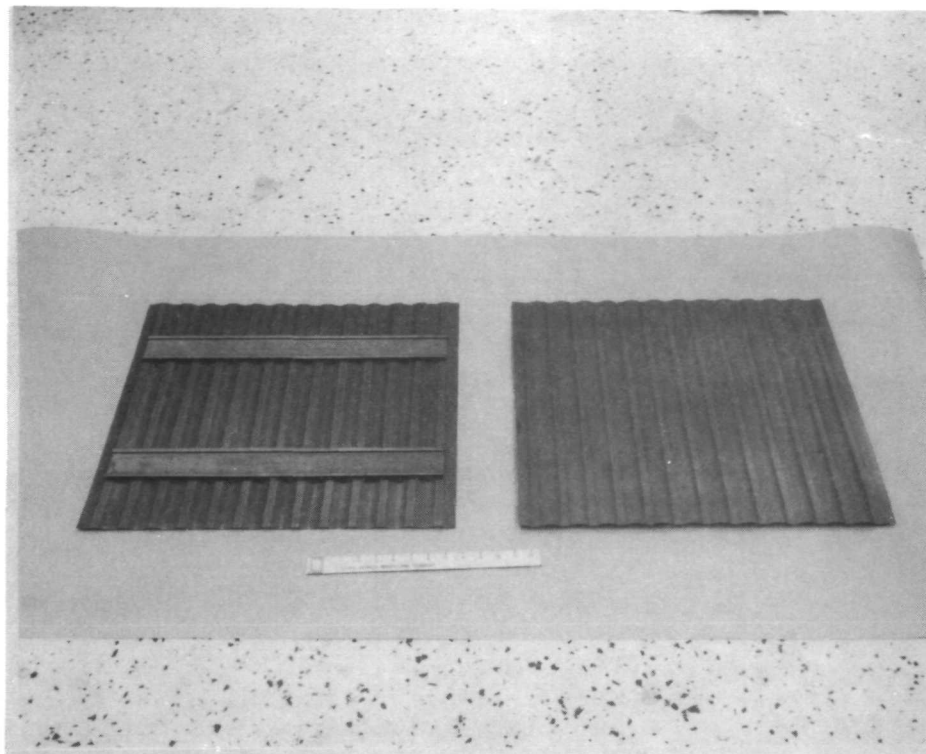


Figure 56 Typical René 41 Heat Shield as Aged (Underside and external surfaces are shown.)

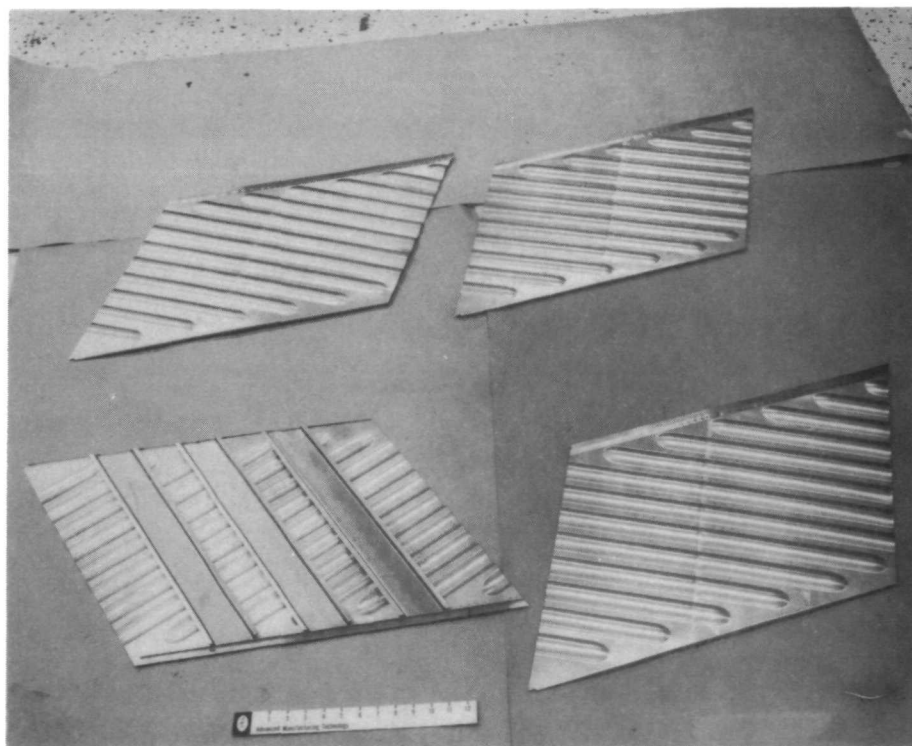


Figure 57 Completed TDNiCr Heat Shields before Oxidation Treatment

Ribs and Spars

The manufacturing sequence for the ribs and spars is shown in figure 58.

The most difficult and exacting subassemblies to build were the rib and spars. They consisted of a sinewave web to which caps were welded at single and compound angles.

These assemblies were complicated by several interdependent factors:

- 1) The welds were made through the cap necessitating an exact tracking mechanism for the web configuration.
- 2) The overall web height was controlled to a total tolerance spread of 0.038 cm (0.015 in.), including an allowance for weld shrinkage. If the tolerance was not held, the rib and spar intersections at final assembly would not mate properly.
- 3) High welded product quality was required. René 41 is not an easy material to fusion weld.
- 4) The exact slopes and cants of the caps as they were welded to the webs required close control over the tooling. Custom backup bars and chill bars were required to make a weldment.

In all, a total of 55 completely welded assemblies were made. All web forming was conducted using the same 22-MN (5×10^6 lb) press as was used for the beaded panels. Figure 59 shows a typical web for a spar assembly.

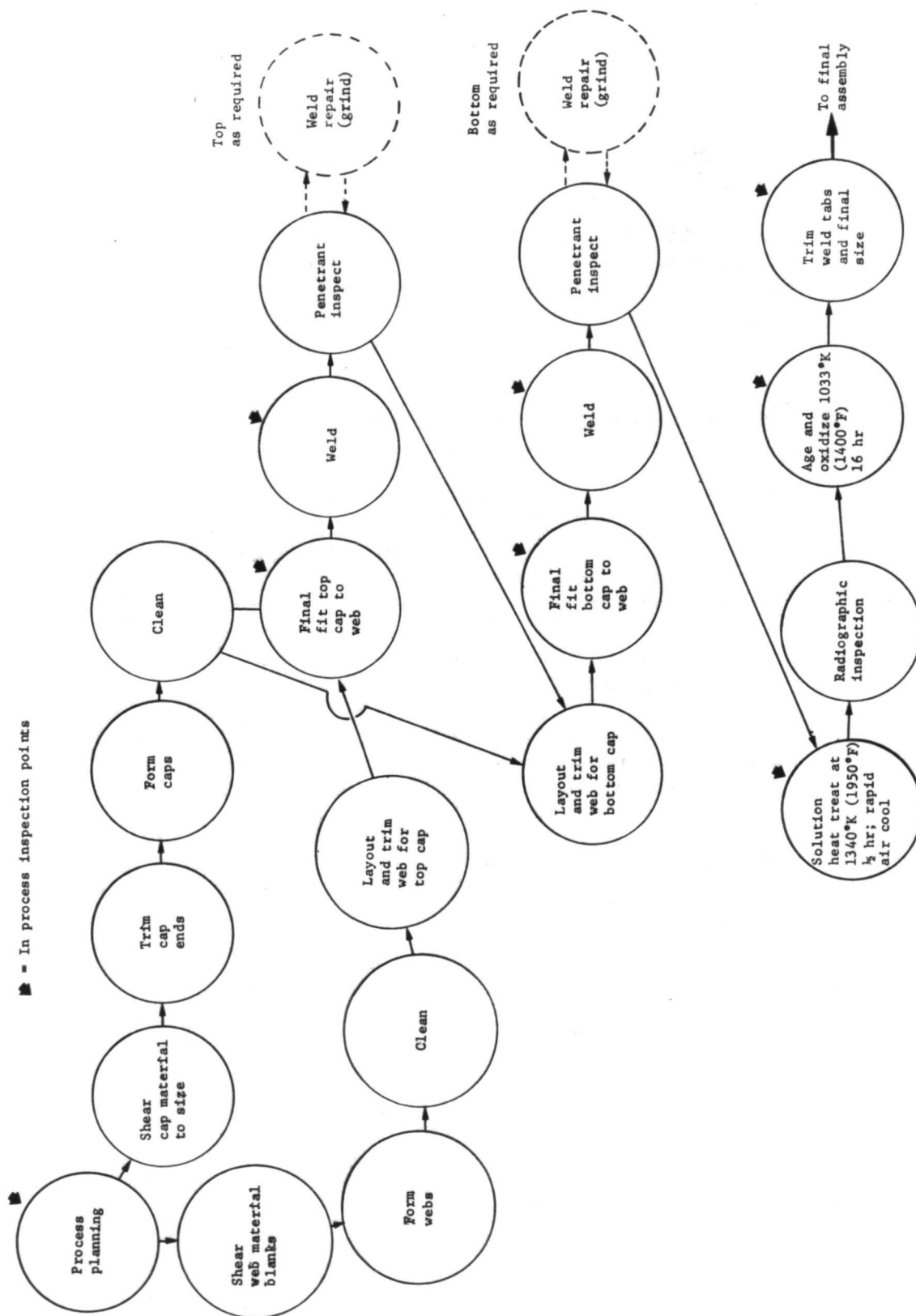


Figure 58 Manufacturing Sequence of Rib and Spar Assemblies

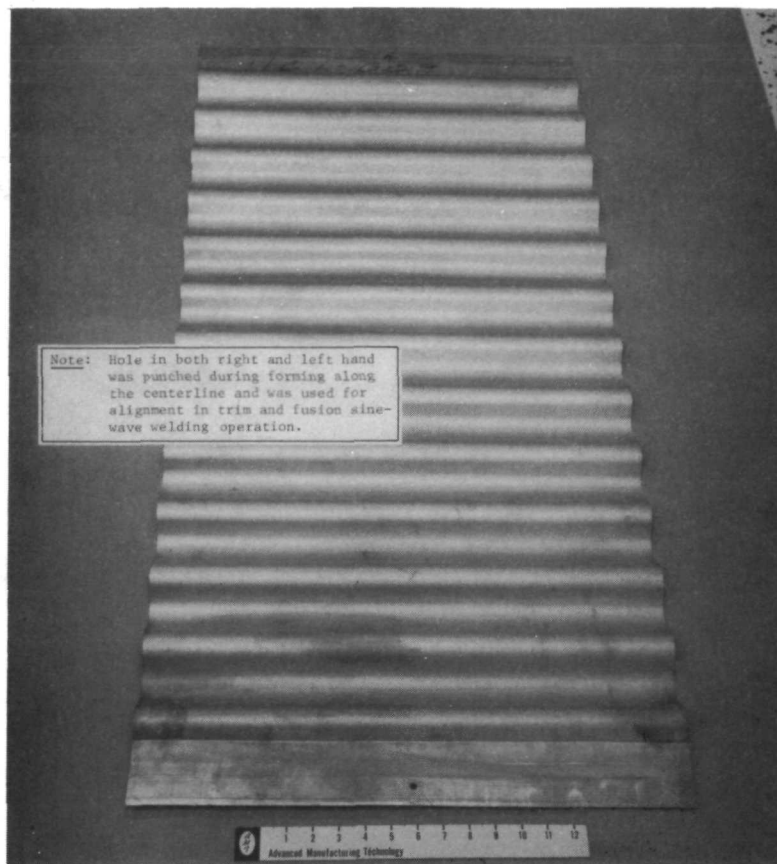


Figure 59 Formed Web Used in Spar Assembly

Figure 60 shows the layout step for the second weld after one cap had already been welded onto a web. Note that the weldment is distortion-free and is easily held in place by the use of small C-clamps onto a tooling bar. This structural support assembly was reinserted into the weld fixture to weld the other cap as shown in figure 61. This method of locating the trim dimensions for the second half of the weldment was used principally to retain control over weld shrinkage that had occurred during the first weldment. Adjustments were made for that weld shrinkage [approximately 0.038 cm (0.015 in.)] and the anticipated weld shrinkage of the second weldment in scribing the cutoff line for the top of the web.

Figure 62 shows a series of spar assemblies that were half completed and were awaiting the tooling change to allow the welding of the other cap. Completed rib welded assemblies are shown as figure 63. In this figure, the compound angles and offset of caps required to allow the ribs and spars to fit at final assembly are clearly visible. These assemblies were processed up through the aging step but had not been finally trimmed. In most cases, these assemblies were not finally trimmed until they were matched to their final assembly position.

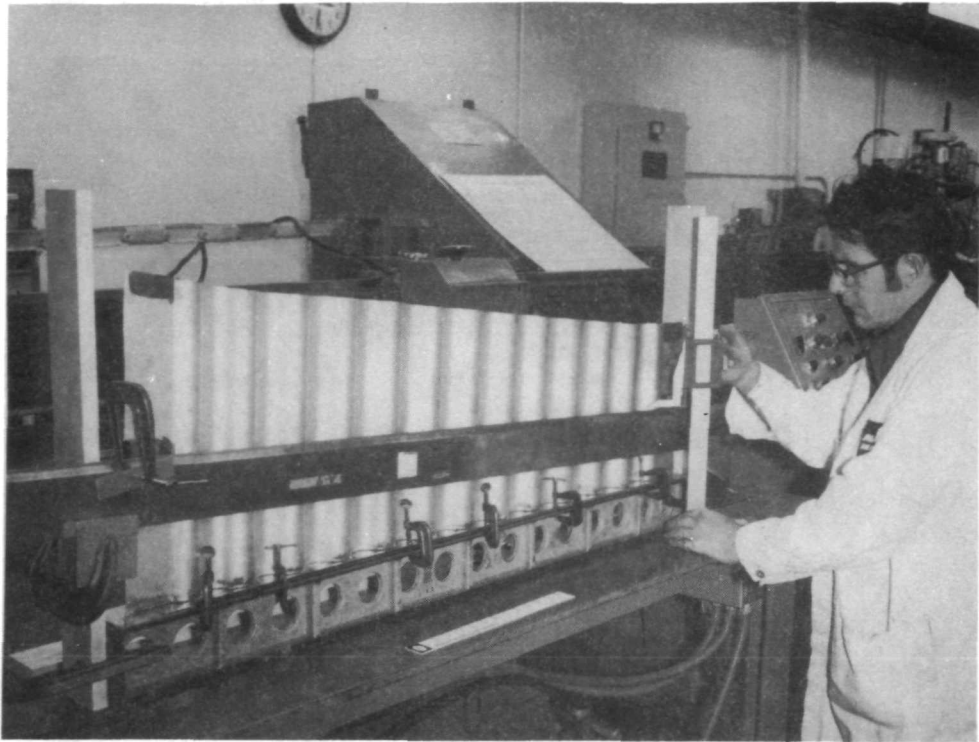


Figure 60 Locating the Trimline of the Web for the Opposite Cap in the Sinewave Weld Assembly

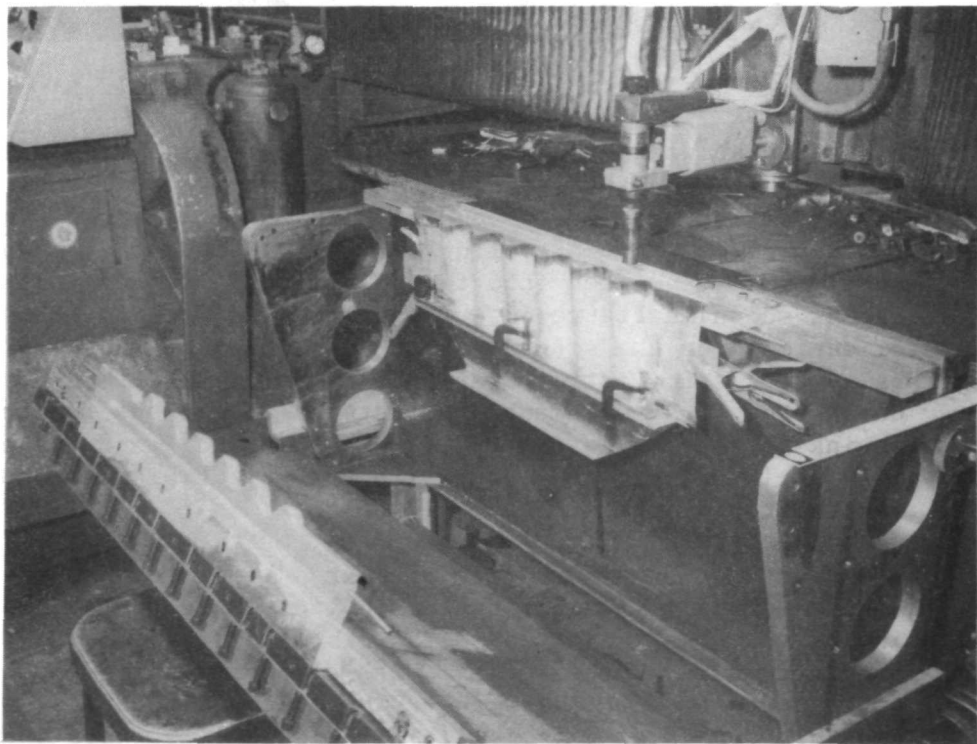


Figure 61 Open View of the Master Weld Fixture Showing the Clamping Arrangement Necessary to Fitup the Opposite Cap for Welding

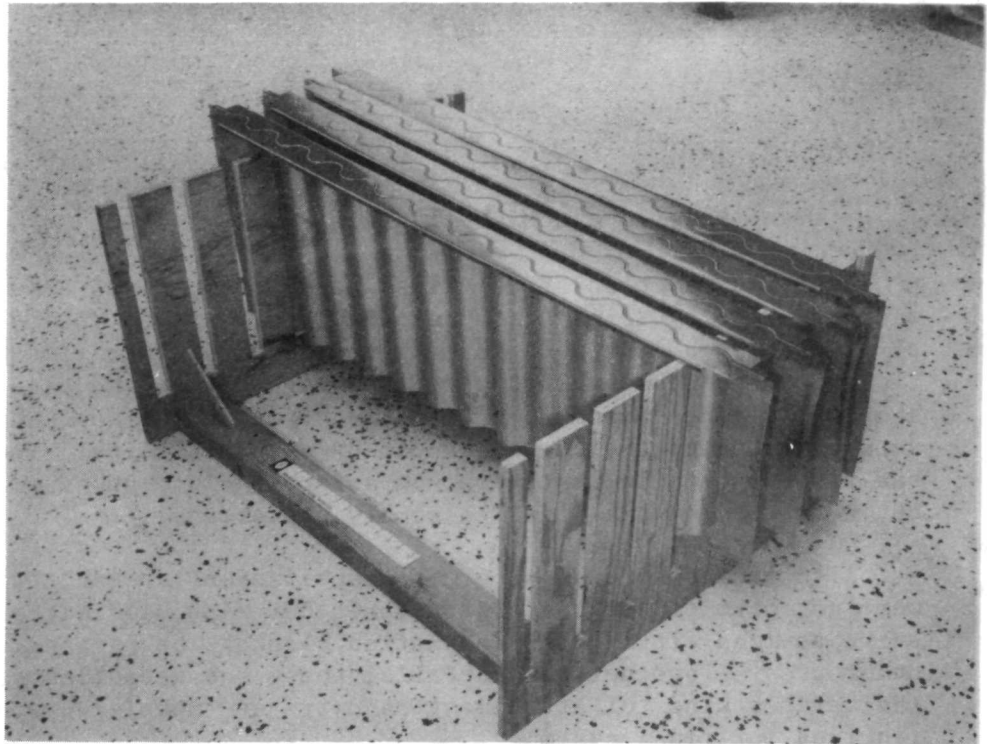


Figure 62 Set of Cap and Web Subassemblies (All common parts were made before changing the weld fixture setup for the joining of the opposite cap.)

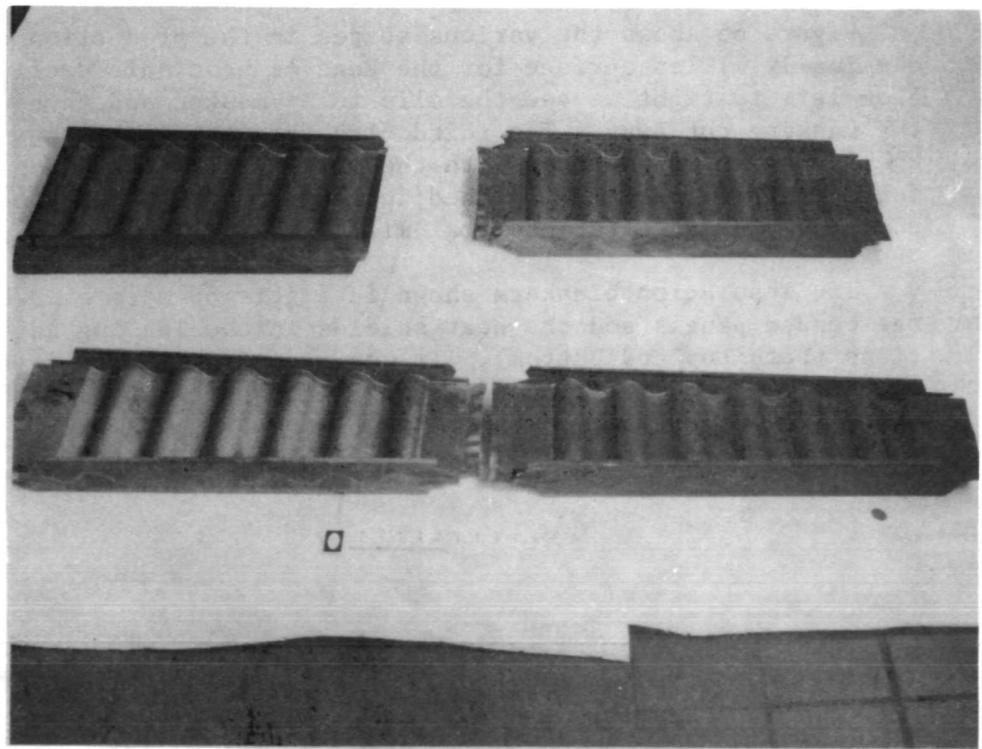


Figure 63 Set of Leading Edge Rib Assemblies As-Welded and Aged (Ready for trim and fitup in final assembly.)

Details and Miscellaneous Subassemblies

Each intersection of the ribs and spars in final assembly was assembled by forming a cross with four angles. These detail parts were made in simple forming and shearing operations. The rib and spar subassemblies were tied together on the exterior of the beaded panel assemblies with tie straps. The heat shields were attached to the beaded panels by standoff clips. These are examples of details that were not assembled into subassemblies, but were used only at final assembly operations.

Also, there were a number of miscellaneous assemblies that were not part of the basic structure, but were used either to serve as load fittings or insulation blankets or in a number of other uses. Together with details, these subassemblies constitute the various kinds of attachment hardware and special-use hardware required for final assembly.

All attachment hardware such as that shown in Figure 64 was purchased. This hardware was made from either Waspaloy or HS 188 alloys and was compatible with the René 41 parent material.

Figure 65 shows the various stages in the production of the chemically milled surface for the René 41 heat shield clips. From left to right we see the clip fully masked and then with the masking cut away. The third clip from the left shows the chemically milled surface with the masking stripped away and the fourth clip (right) is finished including trimming of the edge undercut present after chemical milling.

The insulation blankets shown in figure 66 were used between the beaded panels and the heat shields in the leading edge sections (both top and bottom). It was made from 0.008-cm (0.003-in.) thick Inconel foil sandwiching Microquartz insulation.

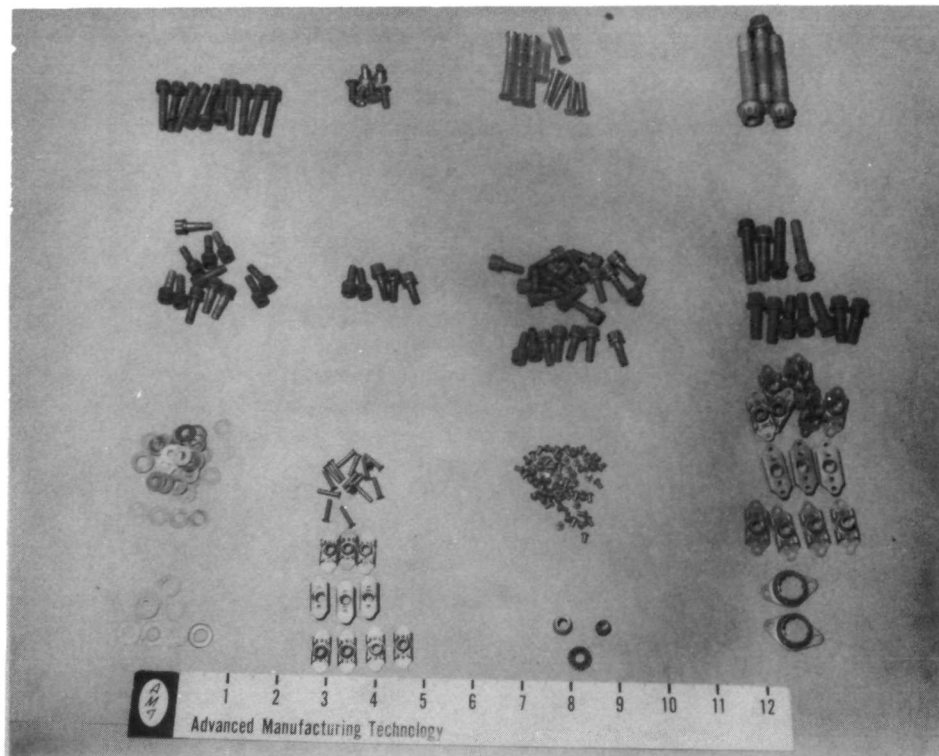


Figure 64 Assortment of Fasteners Used in Final Assembly

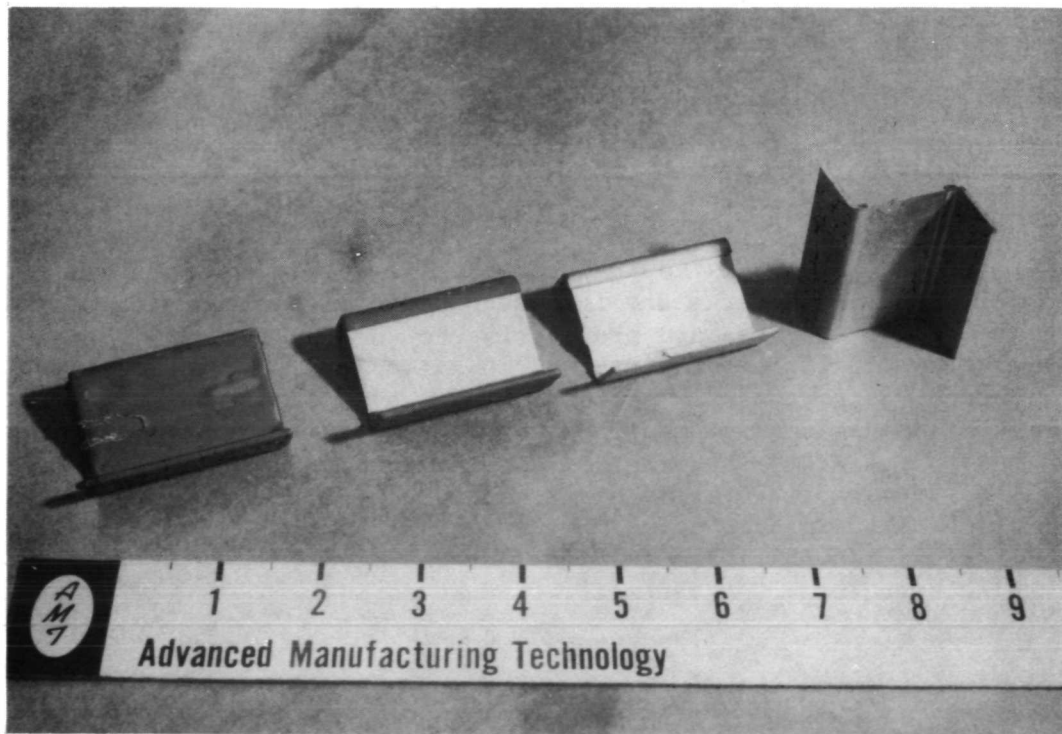


Figure 65 Chem-Mill Sequence of Standoff Clips (Protective plastic coat, strip, and selective chem-mill, as chem-milled.)

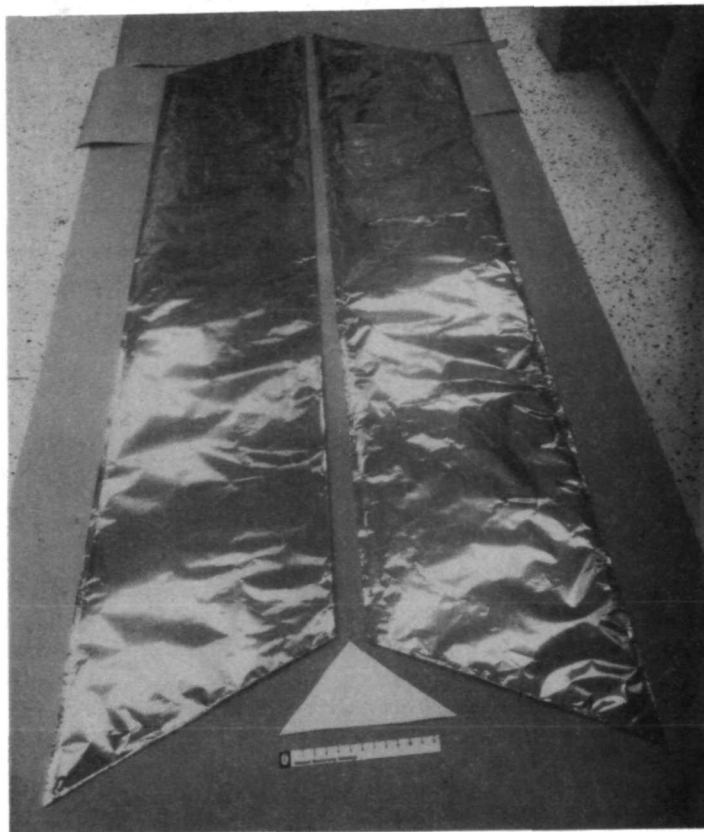


Figure 66 Completed Leading Edge
Insulation Blanket

FINAL ASSEMBLY

The manufacturing flow used for the final assembly is indicated in figure 67. The general final assembly approach was to build the basic structure in a sequential manner starting at the transition area and progressing to the leading edge. Because of the actual flow of parts and subassemblies, the assembly sequence was governed by parts and availability at final assembly. The final assembly operations were carried on in a locating assembly fixture shown in the tooling section of this report. The assembly fixture was a self-contained floor-mounted tool with station plane 25.654 m (1010 in.) near ground level and station plane 23.114 m (910 in.) at top level, positioning the wing structure in a vertical attitude for assembly.

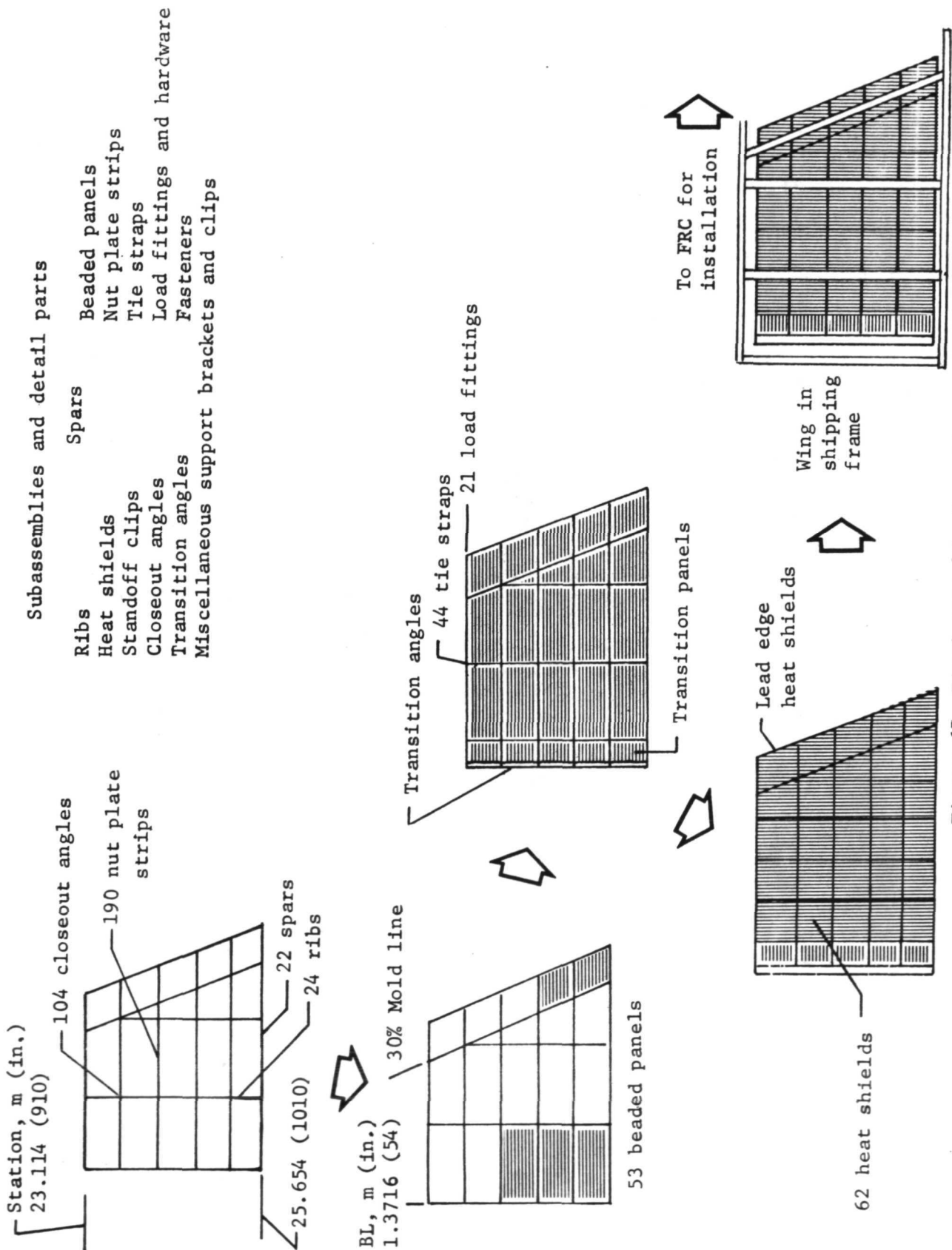


Figure 67 Final Assembly Operation

The ribs and spars were riveted together at their intersection. Four attachment angles were required for each intersection. Figure 68 shows the basic substructure, after riveting attachment angles at rib and spar intersections. Figure 69 shows a typical drill plate being used on lower surface of a rectangular cavity BL 1.3716 to 2.4638 m (54 to 97 in.) between station 24.638 and 25.146 m (970 and 990 in.). This hole pattern is typical for all 18 rectangular cavities. When tie straps were available, they were drilled in position concurrently with rib and spar caps.

After the rib and spar cage cavities were riveted and drilled with coordinated drill plates, the installation of nut plate strips previously manufactured began. All nut plate strips were riveted inside rib and spar caps with 0.238-cm (3/32 in.) flush head HS 188 rivets. Figure 70 shows a technician installing fasteners through cap and nut plate strip with nut runner to assure positive location before riveting. Riveting was with flush-head countersunk rivets using standard bucking bar techniques.

Figure 71 shows the trapezoidal and leading edge drill plates in position on the structure. The drilling procedure was generally the same for all drill plates and cavities. As the construction progressed toward the leading edge, all rib and spar welded assemblies were riveted together, and the caps were drilled to accept beaded panels. This progressive sequence is demonstrated in figure 72.

As the basic structure of ribs and spars was assembled and holes were drilled, beaded panel assemblies were fitted to the structure. The tie straps and peripheral attachment hardware were put in place. Those tie straps that had not previously been drilled, were drilled at this point.

After beaded panels and tie straps were installed, all fasteners were torqued to specification. Attachment holes in the heat shield standoff clips were drilled at subassembly. Standoff clips were mechanically attached to channels using No. 10 screws and self-locking nuts. Figure 73 shows partial installation of standoff clips and load fittings on wing upper surface.



Figure 68 Wing Substructure after Riveting Attachment Angles Common to the Rib and Spar Assemblies

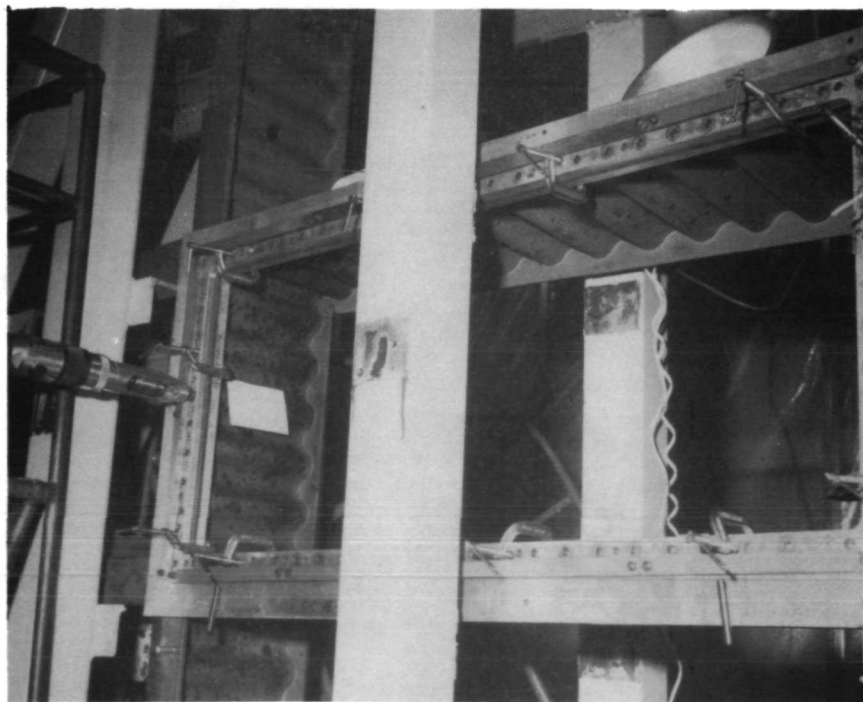


Figure 69 Multiple Use Drill Plate in Position with Power Air Feed Drill Used to Drill Panel Holes Through the Rib and Spar Caps

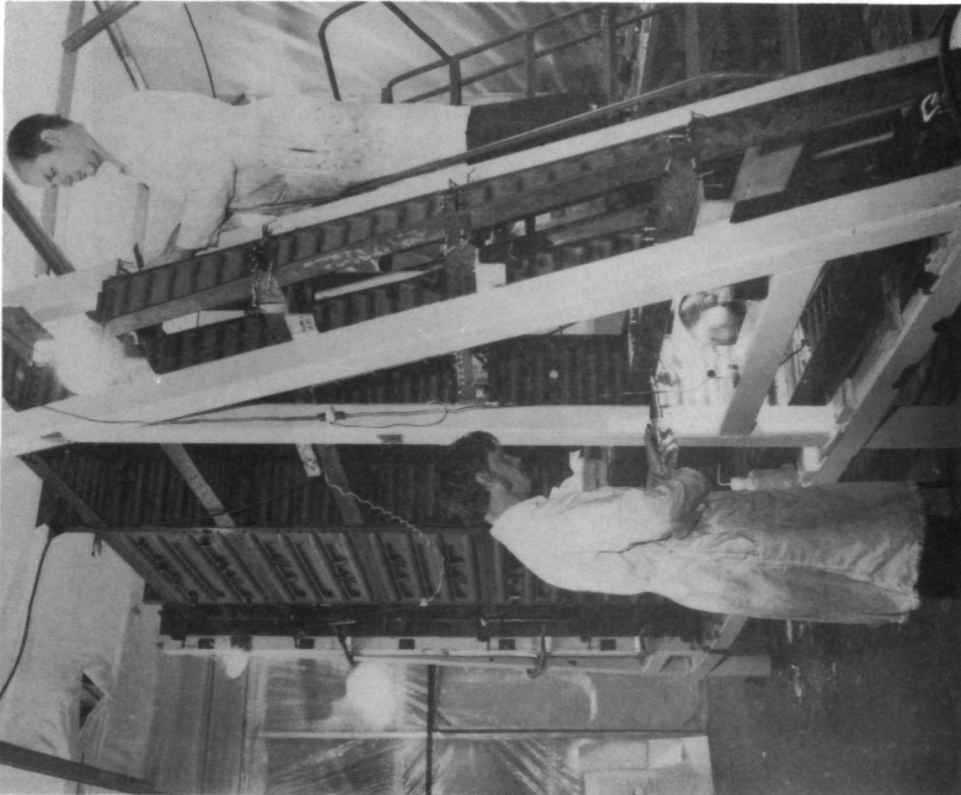


Figure 70 Operator (in Foreground) Installing Fasteners Through Nut Plate Strips Behind Spar Cap

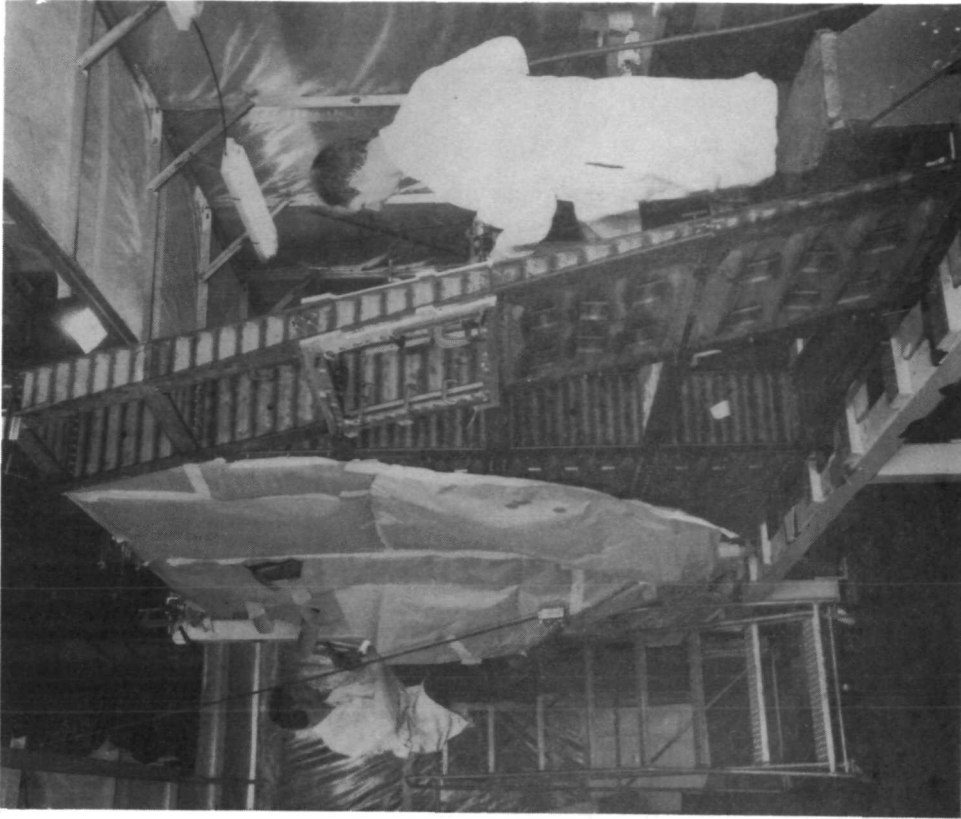


Figure 71 Operator Drilling Mounting Holes (Separate drill plates used for top and bottom sides of the wing; leading edge view.)



Figure 72 Bottom Side of Wing Showing Progressive Sequence of Assembly



Figure 73 Wing Structure Showing All Structural Beaded Panels Installed and Some Heat Shield Standoff Clips in Place

Figure 74 shows complete installation of lower surface panels, tie straps, and heat shield standoff clips. Zee angles are used up to the 30% chord and hat section clips used for leading edge heat shields (TDNiCr). Vertical load fittings required heat shields that were modified from BL 1.3716 m (54 in.) to the leading edge on upper and lower surfaces as shown in figure 75. Vertical load fittings were installed on the upper surface and fit checks made with whiffle tree rod arms to verify orientation of fittings and clearance cutouts in heat shields. The leading edge insulation blankets for upper and lower surfaces were also fit checked before heat shield installation. The lower surface (fig. 76) of the wing was covered with heat shields in the same sequence as the upper surface.

Heat shield extensions for the periphery of the wing were then fit-checked and prepunched for installation at the NASA Flight Research Center (FRC).

The wing test structure was delivered to NASA, Flight Research Center and assembled to the support test fixture (with the appropriate load fittings), as presented in figures 77 through 80.



Figure 74 Closeup of Structural Beaded Panel Installation Showing Tie-Straps, Heat Shield Standoff Clips, and Hat Sections for the TDNiCr Panels

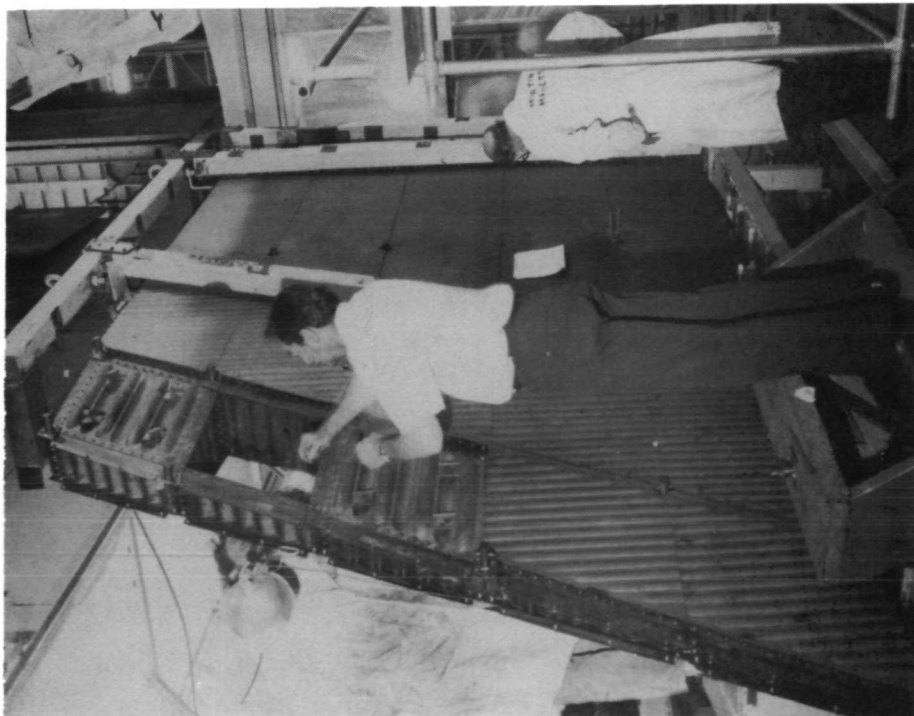


Figure 75 Upper Surface of the Wing Showing Heat Shields Installed and the Vertical Load Fittings

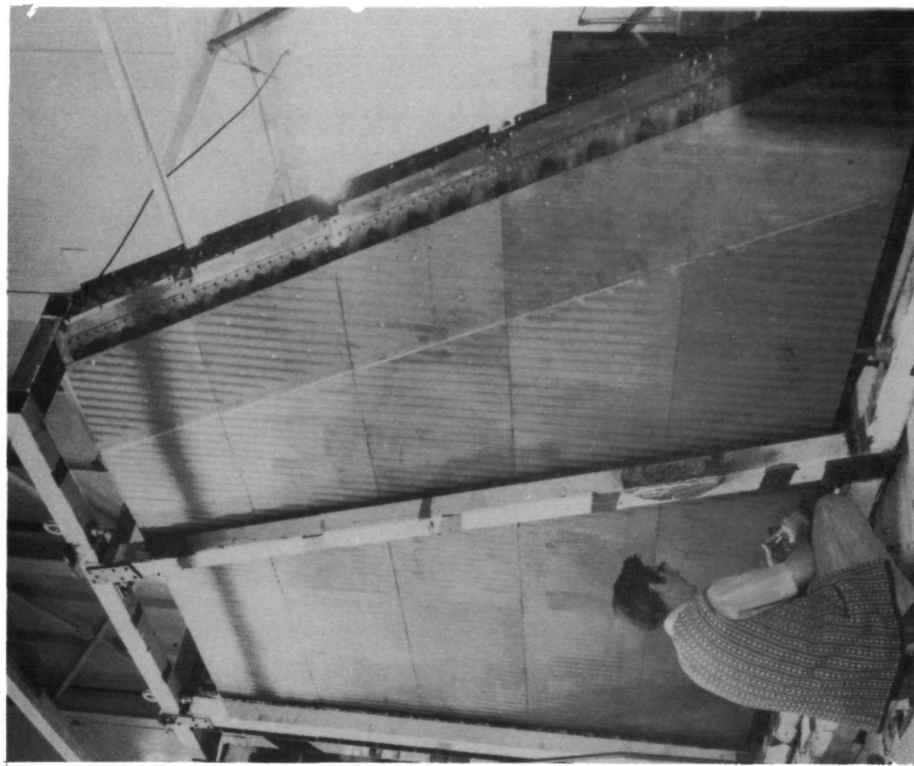


Figure 76 Lower Surface of the Leading Edge Outboard (Inspector is checking the final torque on the heat shield attach screws.)



Figure 77 Overall View of Wing Test Structure Attached to Support Test Fixture at FRC

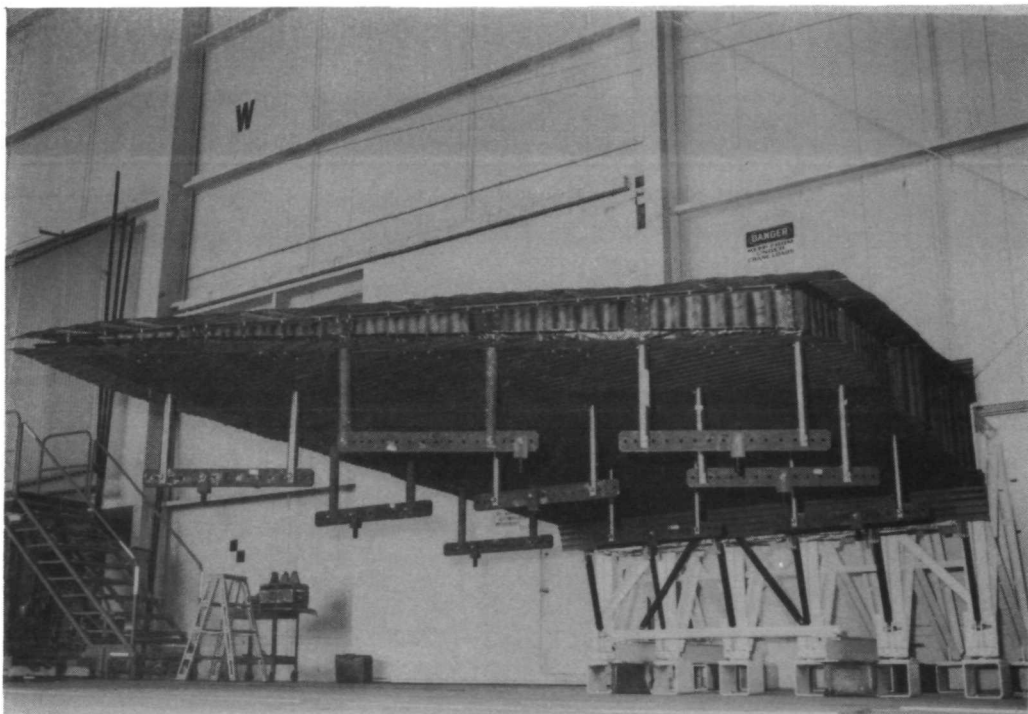


Figure 78 Vertical Loading Devices

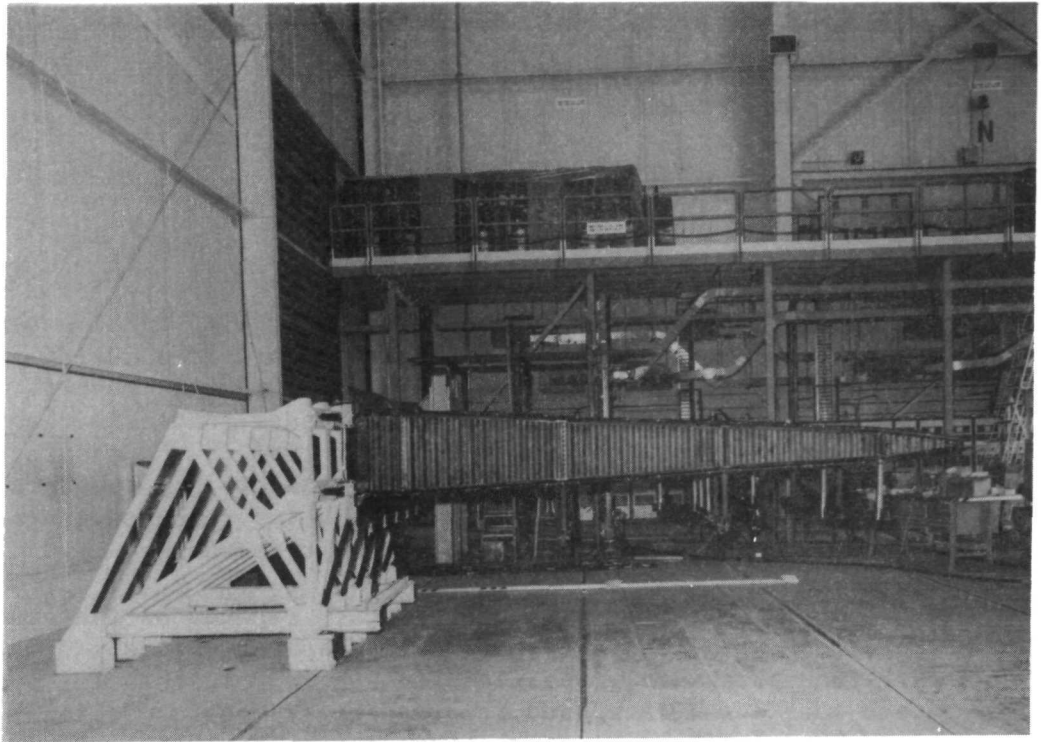


Figure 79 Cross Section of Wing and Support Structure

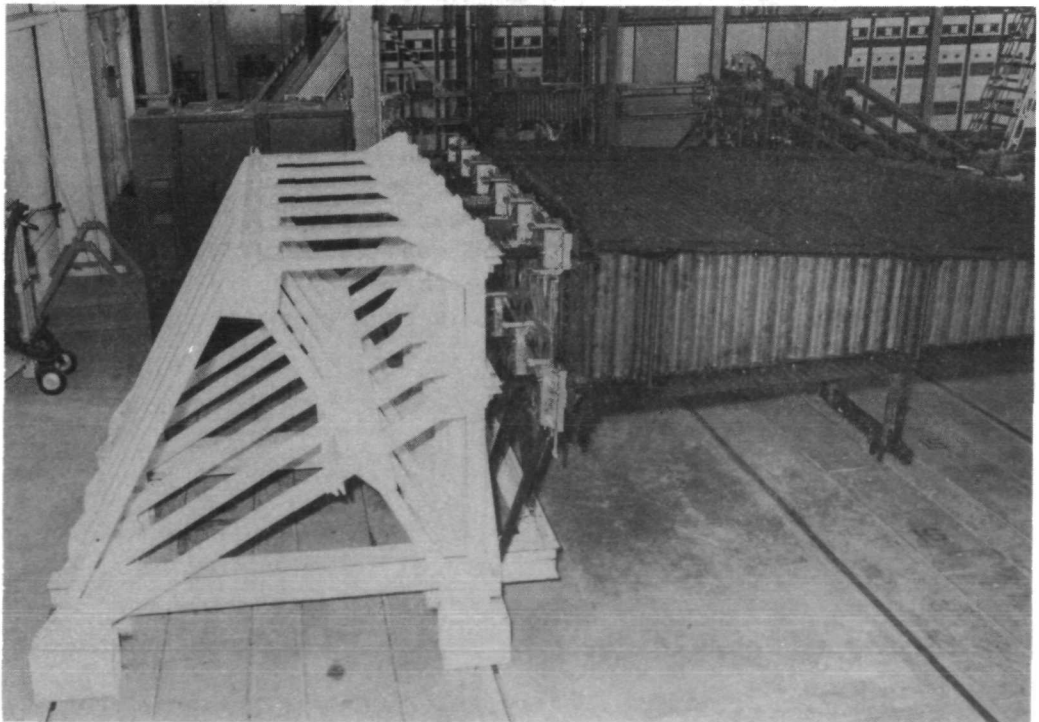


Figure 80 Detail View of Support Test Structure, Water-Cooled Attachment Fittings, and Wing Transition Section

QUALITY ASSURANCE

Surveillance and inspection of hardware were performed in the detail stage, the subassemblies, and during final assembly operations. Continuous surveillance was provided during final assembly operations. As previously noted in this report, quality check points and inspection points were designated in the flow diagrams that show the operations performed in the manufacture of the various major subassemblies. In addition, the detail plan packages for details and subassemblies required inspection and buyoff before proceeding to the next operation.

The basic instrument used to retain records of individual operations with regard to details and subassemblies was the parts and subassembly verification record. In this log book, items were accumulated and recorded regarding inspection results from the detail planning, heat treat results, radiographic records, and functional test or check results. The log book served to also check on the manufacturing parts list and to verify the status of manufactured details and subassemblies during their various operations in the manufacturing sequence. A second set of records was the Minor Discrepancy Reports (MDR), which recorded variances of finished hardware to the engineering requirements.

The majority of the inspection for the program was accomplished using standard techniques and tools. Height gages, micrometers, depth gages, and thread gages were typical of the standard tools that were used to evaluate the quality of produced hardware. Radiographic inspection was performed on welds using standard aircraft techniques and controls such as penetrometers and other beam intensity verifications.

CONCLUSIONS

By considering the objectives of this program as: developing a prototype flight-loads measurement system; evaluating flight-loads instrumentation; determining methods of high-temperature calibration; providing temperatures simulation techniques; and finally testing to design conditions to demonstrate the concept, the conclusions are as follows:

- 1) The wing structure was analyzed and was found to be satisfactory from the standpoint of ultimate load, panel flutter (for zero flow angle), wing flutter, sonic fatigue, and creep, without requiring refurbishment throughout the life of the Hypersonic Research Airplane.
- 2) Insulation was required at the outboard (between 30% chord line and leading edge) lower and upper surface areas to minimize the thermal stresses and limit the beaded panel structure temperatures to approximately 1033°K (1400°F).
- 3) The 2.5-g maneuver load condition designed the structure (combination of mechanical and thermal loads). Thermal loads were important to design, and a proper thermal protection system can reduce weight. However, insulation placement could not reduce aft wing thermal stresses because of the shape of the wing cross section.
- 4) The beaded panel tests agreed well with theory, and joint tests showed the adequacy of the welds and fasteners.
- 5) Multiple usage tooling assured proper tolerances and minimum cost. As an example, nonmetallic inserts were used to allow for forming of the variable beaded length panels.
- 6) A unique method was obtained for welding sine wave webs to channel caps. An optical tracer synchronized to a weld torch produced superior subassembly weldments for a large variety of similar configurations.

Martin Marietta Corporation

Denver Division

Denver, Colorado, August 21, 1973

APPENDIX A

PANEL TESTS AND FABRICATION

PURPOSE OF TESTS AND PANEL DESIGN

Panel tests were used to verify that beaded panels performed as predicted. Panels in an optimized configuration were tested to establish buckling loads at elevated temperature under combined compression, shear, and pressure.

Local attachments and eccentricities were the same as the wing design. Differences between measured and predicted failure loads in any mode greater than 20% would have required additional optimization iterations, differences between 5 and 20% would have required resizing for least weight utilizing the equations used for the optimization.

Examination of NASTRAN stress analysis of the wing showed a ratio of axial line loads to shear line loads of 3 to 1 or greater. The limiting axial load on the box with the NASA panel was 1007 N/cm (575 ppi). Using a factor of 0.8 (compression without shear or pressure) the maximum compressive load for the box was established at 806 N/cm (460 ppi). During test, the box was subjected to compressive load combined with torsion and pressure.

Panel ultimate design load of 613 N/cm (350 ppi) was 75% of the box cutoff load of 806 N/cm (460 ppi). Using a 3 to 1 ratio of axial to shear line load gave a shear load for the panel of 210 N/cm (120 ppi). For these line loads 5171 N/m² (0.75 psi) internal pressure and 922°K (1200°F) temperature, a panel design that was buckling critical was selected, using the optimization program. Overall panel size was 45 cm (17.7 in.) wide by 78 cm (30.7 in.) long, for an opening of 41x73 cm (16x29 in.) and fastened with 104 No. 8 screws.

The optimization computer program, OPTBEAD, used in an analysis mode provided a buckling interaction curve, with strength cutoff. Results from the runs of OPTBEAD provided the configuration that met the design criteria shown in figure A1.

Panel doublers were incorporated at the ends to provide additional strength. Additional thickness resisted local buckling and reduced high stresses adjacent to the fasteners. There was a gradual introduction of load from the fasteners to the bead area through the tapered fingers along the panel flats.

APPENDIX A

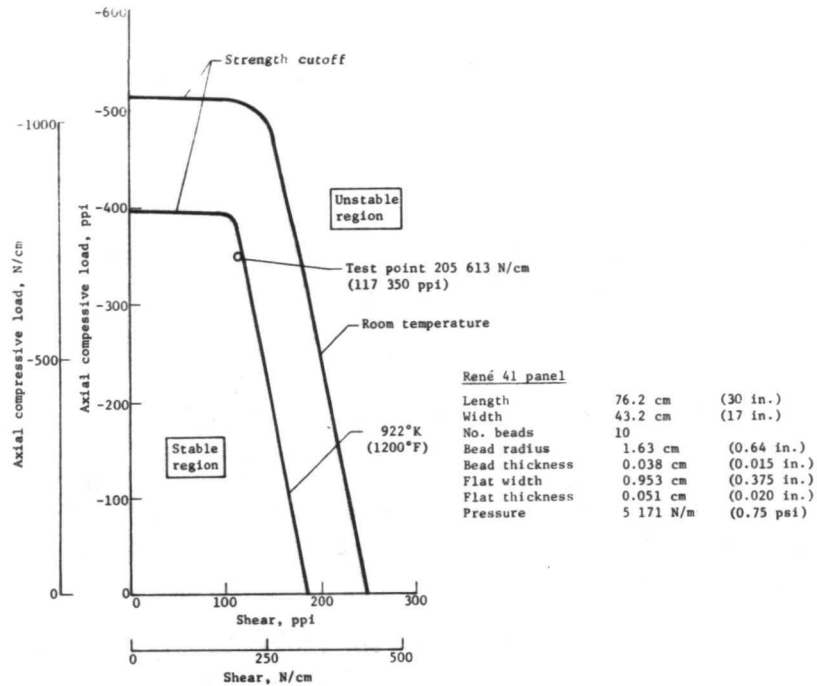


Figure A1 Interaction Curve for Test Panel Buckling

Doublers resisted wracking of the flats at bead termination due to shearing stresses. The extension of the doubler over the concave portion of the bead provided increased bending resistance as the bead became shallow. This extension with the stiffening tab formed a box for increased torsional rigidity to resist local shear deformations.

Thickness requirement was based on the assumption that the panel was pinned at both ends. For the in-plane load and internal pressure, a doubler 0.076-cm (0.030-in.) thick spot welded to both sides of the panel was adequate. Doublers were spot welded on both sides of the panel and tapered in thickness by chem-milling to provide a gradual load transition from fasteners at the flat ends to the fully beaded section. Fastener holes were located with a drill template made to match the hole pattern of the box.

APPENDIX A

DESCRIPTION OF TEST BOX AND LOAD FIXTURE

The hypersonic wing box test specimen represented state-of-the-art structures technology applied to a delta wing design. The box was fabricated from René 41, using a radiation-cooled, semimonocoque construction. This was demonstrated, analytically, to be the least weight structural system for the Mach 8 Hypersonic Research Airplane (HRA).

Wing box dimensions were 180 cm (31 in.) long by 46 cm (18 in.) wide by 25 cm (10 in.) deep. Both ends of the box were designed to distribute discrete loads into the test section as representative of a continuous structure. The test section was connected to a set of corrugated cover panels and spar extensions fastened to the end channels. One end channel had 10 holes for load rods and the other had 10 holes for the reaction rods (five each on the upper and lower surface). Shear and torque loads were applied through four vertical rods, one at each corner of a rib/spar intersection. Shear and torque loads were reacted by rods attached to the opposite end channel.

The hypersonic wing box test specimen with the test panel fastened in place is shown in figure A2. In-plane loads were applied to the end channel shown at the right of the figure. Two of the four shear and torsion rods are shown folded along the upper spar caps. The end channel at the left rear of the figure is the reaction end with attachment holes for in-plane rods, and shear and torque rods. A fitting for pressurizing the interior of the box is shown below the torque rod.

To load the box in its several load modes, an external fixture reacted the loading devices. Hydraulic actuators in series with a load cell were used to apply and measure the external loads.

A schematic of the box and loading system is given in figure A3. All actuators, load cells, and reaction rods are shown in position. Note that although 20 in-plane load and reaction points are provided (five top and bottom at each end) this series of tests used 12 of these points (three top and bottom at each end). Turnbuckles allowed rod length adjustment to assure each rod was loaded equally.

The external parts of the loading fixture were steel channels and wide flange beams. These parts were designed to provide a loading frame and to hold the infrared reflectors and quartz lamps.

APPENDIX A

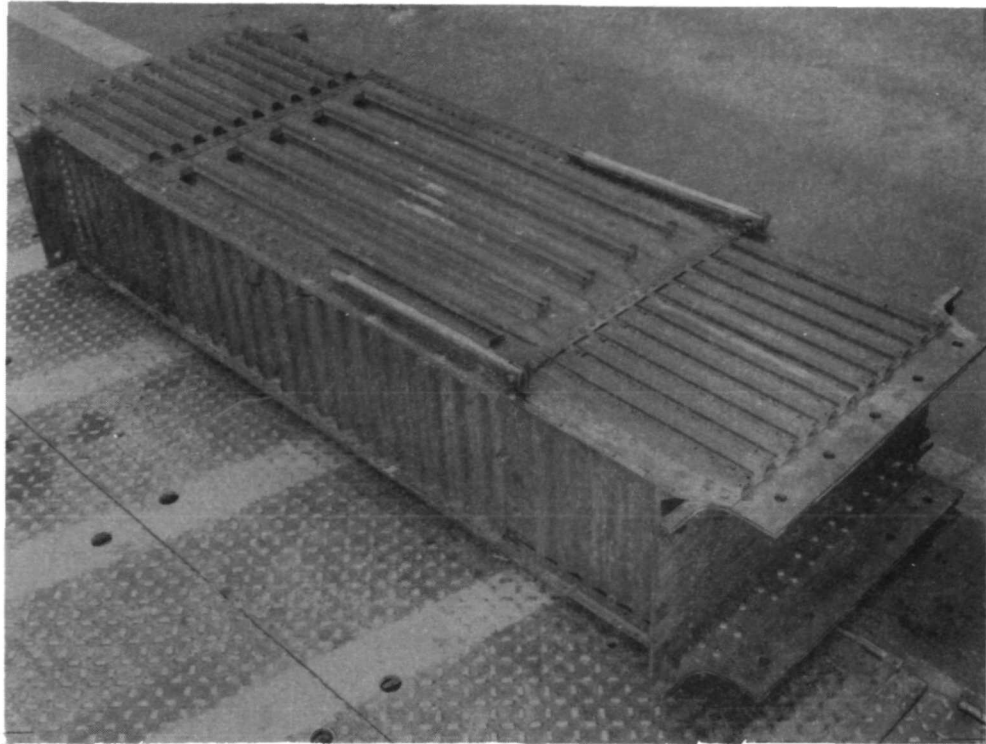


Figure A2 Hypersonic Wing Box Test Specimen with Test Panel Fastened in Place

Load and reaction rods were made from 2.54-cm (1-in.) diameter Inconel X-750 material. For the in-plane loads the upper surface was put in compression using 44.5 kN (10 kip) hydraulic actuators in series with 22.2 kN (5 kip) BLH load cells. The bottom surface was placed in tension using 44.5 kN (10 kip) actuators and BLH load cells.

Torsion loads were produced by two torque rods acting in tension and the other two in compression. The tension and compression lines used 89.0 kN (20 kip) actuators. BLH load cells for the tension lines were 11.1 kN (2.5 kip) and for the compression lines, 22.2 kN (5 kip).

To provide a pressure seal between the panel and the caps, a high temperature sealant was applied to the mating surfaces. The sealant, NAS 3310-54-2, was received in powder form, mixed with water, and cured about 422°K (300°F).

APPENDIX A

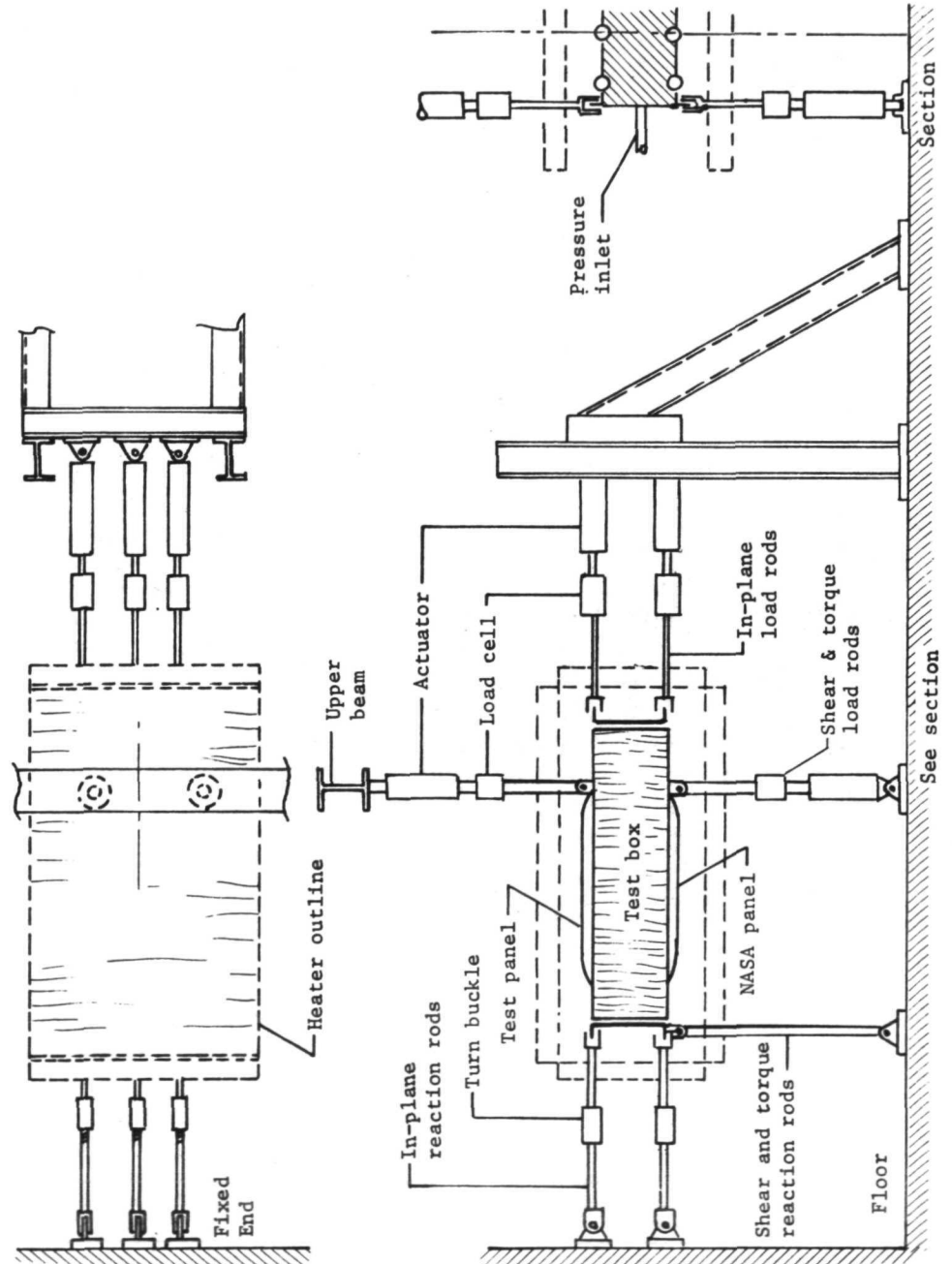


Figure A3 Test Fixture and Loading System

APPENDIX A

Panels were fastened with 104, NAS 1632 C, No. 8 screws. Over the rib caps a tie strap was placed across the end of the panel and riveted to the corrugated cover panels thereby loading the panel fasteners in double shear. Along the spar caps the fasteners were in single shear. These details are clearly illustrated in figure A2.

CALIBRATION OF BOX

Axial and shear loads for the 922°K (1200°F) test panels had been established as 613 and 205 N/cm (350 and 117 ppi), respectively, at 922°K (1200°F) combined with 5171 N/m² (0.75 psi) internal pressure. The correlation of load cell readings to the panel loads was accomplished at room temperature by instrumenting the box and the test panel with strain gages. The room temperature calibrations were used at elevated temperatures based on the fact that internal equilibrium is realized at any temperature when the system is at an isothermal steady state.

The calibration setup used a total of 20 SR-4 strain gages. Located on the test specimen were three rosette gages at the ends of the panel, three rosette gages at the center, and two axial strain gages located on the sides of the panel. Rosette gages were rectangular, three-gage 45° stars. The bottom cover panel had the same type and number of strain gages. A biaxial shear gage was located on each spar of the test fixture. Strain gages were used only during the calibration of the test box. The data from the strain gages were put through a signal conditioner and recorded on high-speed magnetic tape. The tape was used for computer reduction of data.

During the calibration, eleven 1.27 cm ($\pm 1/2$ in.) displacement transducers were placed on the test specimen and fixture. These were read and recorded manually from a digit voltmeter and also recorded on high-speed magnetic tape. The displacement transducers were placed on the panels so that overall box deflections were determined.

Geometry and configuration of the test box and test panel are given in figure A4. The test panel had 10 beads, whereas the NASA panel had eight beads. Bead thickness of the test panel was the result of stretching. Flat thickness was approximately the sheet thickness. Bead and flat thicknesses were the same for the NASA panel. Also, the flat dimensions were 0.95 and 1.27 cm (3.8 and 1/2 in.) for the test and NASA panels, respectively, and the bead angles were slightly different as shown in figure A4.

APPENDIX A

Axial Load

Before the calibration runs, each load line was pressurized twice to a maximum load of 890 N (200 lb). Loading and unloading of individual load lines insured that each was functioning. To ensure the axial load was evenly distributed between the six axial rods, each line was loaded to 1779 N (400 lb) and the turn-buckles were adjusted. When the strains, measured by the gages on the rods, were equal in all members, the load was considered to be evenly distributed across the reaction end of the test fixture.

Calibration for the panels proceeded in the following manner:

- 1) All load lines were inspected, load cells calibrated, and displacement transducers set for range and zeroed.
- 2) Axial load was applied to the upper and lower load rods, compression load on top and tension load on bottom.
- 3) At each increment of load, strain and displacement data were recorded. For Panel 1 the maximum load was 6361 N (1430 lb) per load line. Panel 2 was calibrated to 10 387 N (2335 lb) per load line.
- 4) Data were reduced and plotted to establish the loading curves.

Rosette data were analyzed on a computer providing printout for principal stresses and angle. Figure A5 is a schematic of the rosette gages identifying each of the three gages. Also shown are the principal strains, stresses, and their angle θ .

Solutions for maximum and minimum strains from the rectangular, three gage, 45° rosette are given in reference A1. Principal strains may be written as

$$\left. \begin{aligned} \epsilon_{\max} &= \frac{1}{2} (\epsilon_1 + \epsilon_3) + \sqrt{\frac{1}{2}} \left[(\epsilon_1 - \epsilon_2)^2 + (\epsilon_2 - \epsilon_3)^2 \right]^{\frac{1}{2}} \\ \epsilon_{\min} &= \frac{1}{2} (\epsilon_1 + \epsilon_3) - \sqrt{\frac{1}{2}} \left[(\epsilon_1 - \epsilon_2)^2 + (\epsilon_2 - \epsilon_3)^2 \right]^{\frac{1}{2}} \end{aligned} \right\} \quad (A1)$$

APPENDIX A

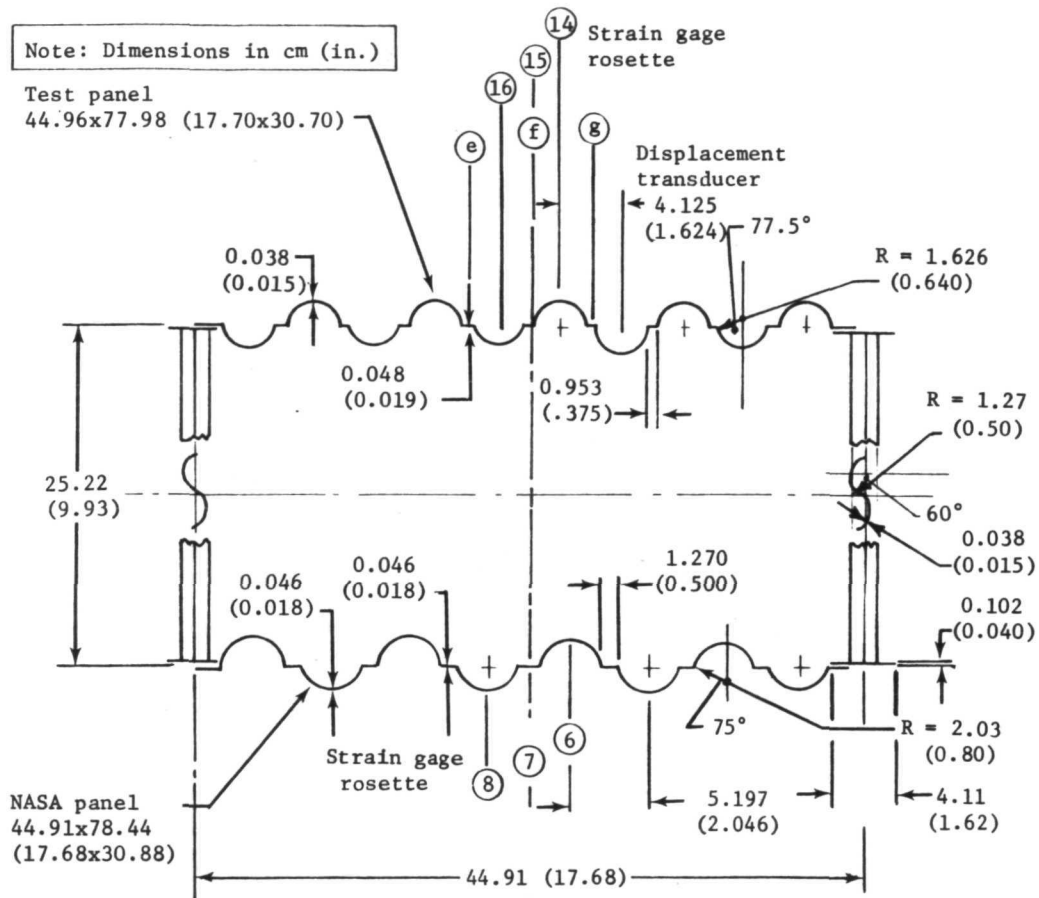


Figure A4 Section Through Centerline of Test Box, Looking Toward Reaction End

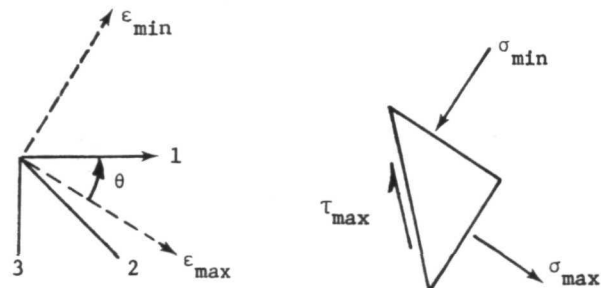


Figure A5 Rosette Strain Gage and Principal Strains and Stresses

APPENDIX A

Using the principal strains from Equation (A1), the maximum and minimum stresses are

$$\left. \begin{aligned} \sigma_{\max} &= \frac{E}{1 - \nu} 2 \left(\epsilon_{\max} + \nu \epsilon_{\min} \right) \\ \sigma_{\min} &= \frac{E}{1 - \nu} 2 \left(\nu \epsilon_{\max} + \epsilon_{\min} \right) \end{aligned} \right\} \quad (A2)$$

The maximum value of shear is obtained from the principal stresses as

$$\tau_{\max} = \frac{\sigma_{\min} - \sigma_{\max}}{2} \quad (A3)$$

The angle at which these values occur is given by the following expression.

$$\tan 2\theta = \frac{2 \epsilon_2 - \epsilon_1 - \epsilon_3}{\epsilon_1 - \epsilon_3} \quad (A4)$$

Results of the gage reduction and converting stresses to axial line loads are given in figure A6 for Panels 1 and 2. The conversion is given by the expression

$$N_Y = \sigma_{\min} \bar{t} \quad (A5)$$

For Panel 1, measurements of the panel before and after forming established \bar{t} (the average thickness of the sheet) as 0.048 cm (0.019 in.). Similar measurements made on Panel 2 set \bar{t} as 0.051 cm (0.020 in.). The angle θ was near 0° , indicating the maximum stress (line load) was nearly parallel to the longitudinal axis.

A small amount of bending of the beads is shown in figure A6 by gages 14 and 16. Summation of forces verified equilibrium for Panels 1 and 2 and the NASA panel.

Torsion Load

Shear calibration of the test box and the test panel was accomplished by applying torsion to the box. Torsion loads were applied at one end and reacted at the other end. It was established from the strain gages on the axial reaction rods that they had little or no load during the torsion calibration.

APPENDIX A

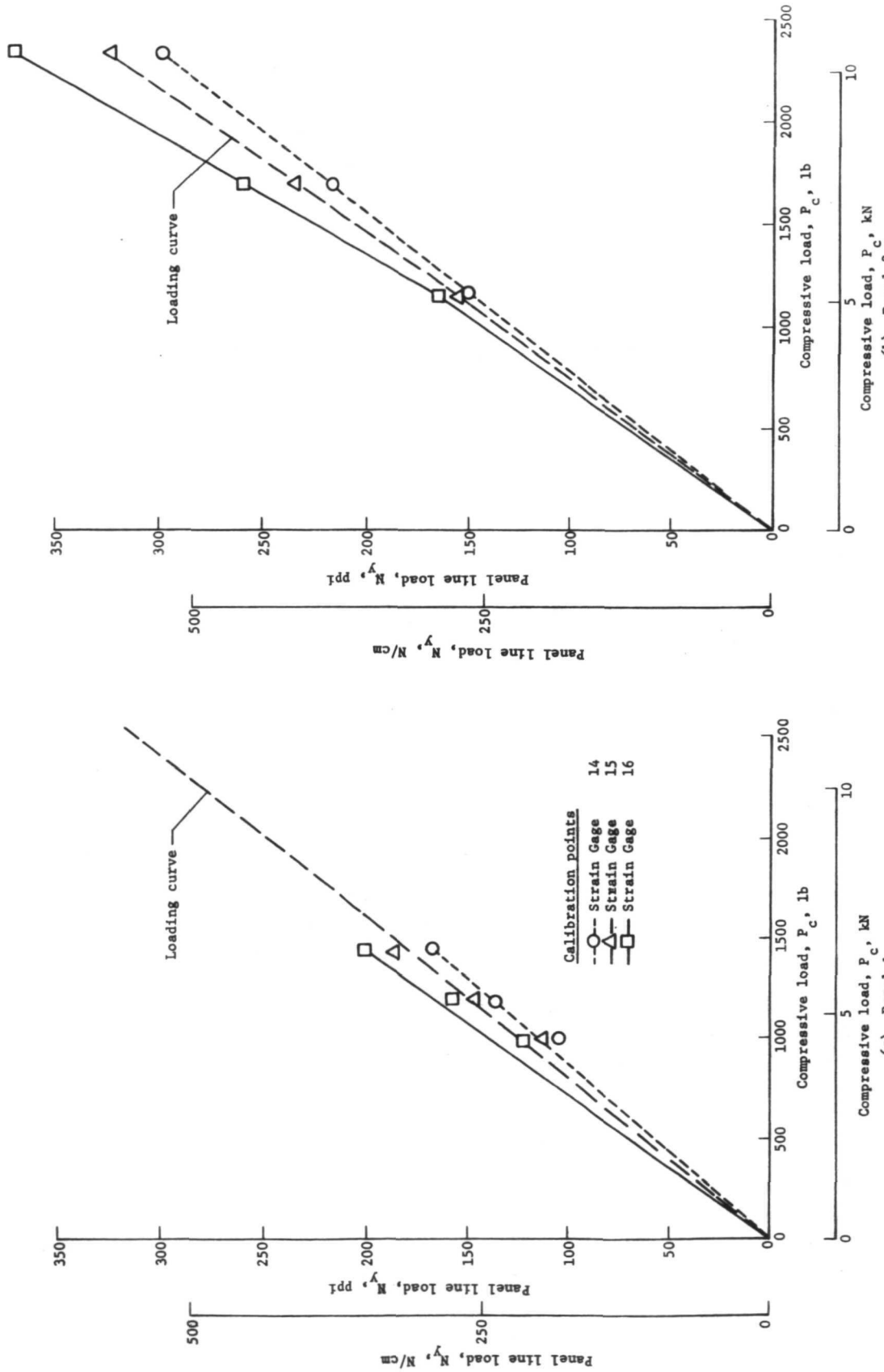


Figure A6 Calibration and Loading Curve for Axial Load

APPENDIX A

Strain gages 14, 15, and 16 were used to correlate panel shear stress (shear line load) with the torsion load. Results from the computer analysis of the rosette data are shown in figure A7 for Panels 1 and 2. During test the full torsion load was applied and the axial load applied incrementally. This test point was essentially the same in Panels 1 and 2 as shown in the figures. An equilibrium check was performed to check the external moment and the internal moment.

Similar checks apply to Panel 2. The orthotropic nature of the beaded panel noticeably modified the theoretical shear flow found in isotropic construction. For an isotropic box of these dimensions, the theoretical uniform shear flow was 212 N/cm (121 ppi) a value between the shear in the panel and web.

Deformation along the longitudinal axis was measured by three displacement transducers c, f, and i of figure A8. At maximum shear load of 205 N/cm (117 ppi) the panel exhibited an inward deformation of 0.043 cm (0.017 in.) This deflection increased from zero as the load was increased.

Combined Loads

The axial and torsion loads were applied in combination. Examination of the strain gage showed very good agreement between the values achieved by adding the strain from axial load to the strain from torsion load and comparing this to the direct output of the combined loads. The method used was to apply five equal increments up to the total load for Panel 1 and three equal steps for Panel 2.

It was demonstrated that superposition did apply and the individual calibrations were valid when used in combination.

ELEVATED TEMPERATURE INSTRUMENTATION

Following the satisfactory calibration of the panel, strain gages were removed from the panel and the test fixture and thermocouples were mounted. Quartz lamp heating arrays were installed above and below the test fixture and at both ends. Number 8, Cera Felt insulation 3.81 cm (1½ in.) thick was placed around the test fixture to avoid excessive heat loss.

APPENDIX A

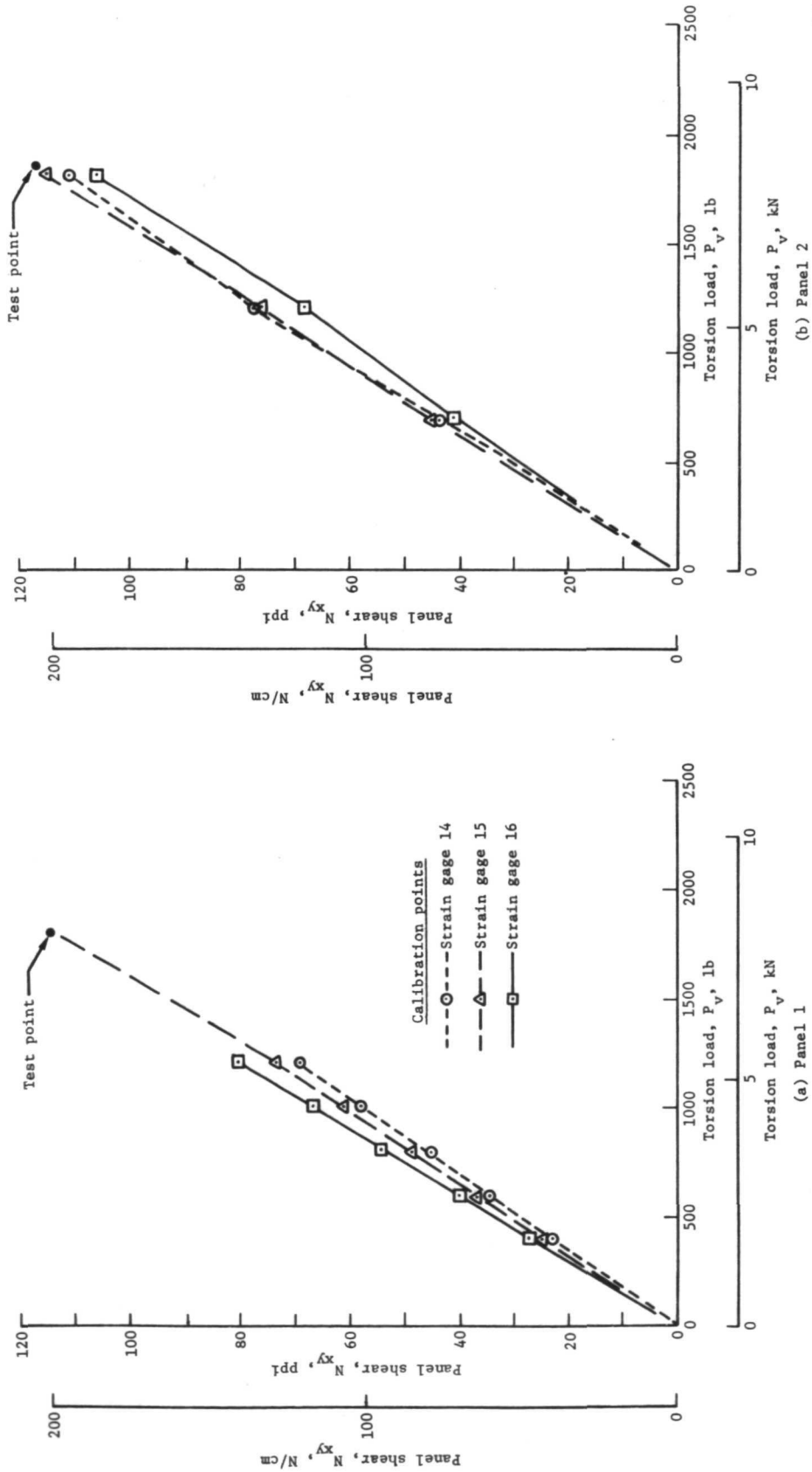


Figure A7 Shear Calibration and Test Load Point

APPENDIX A

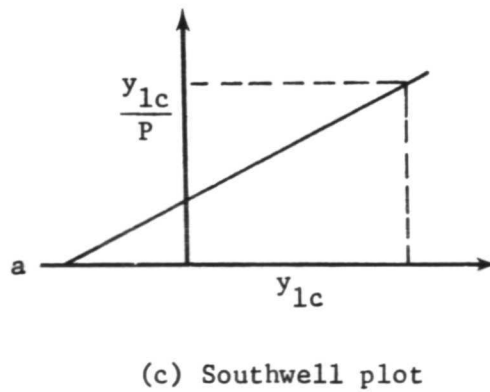
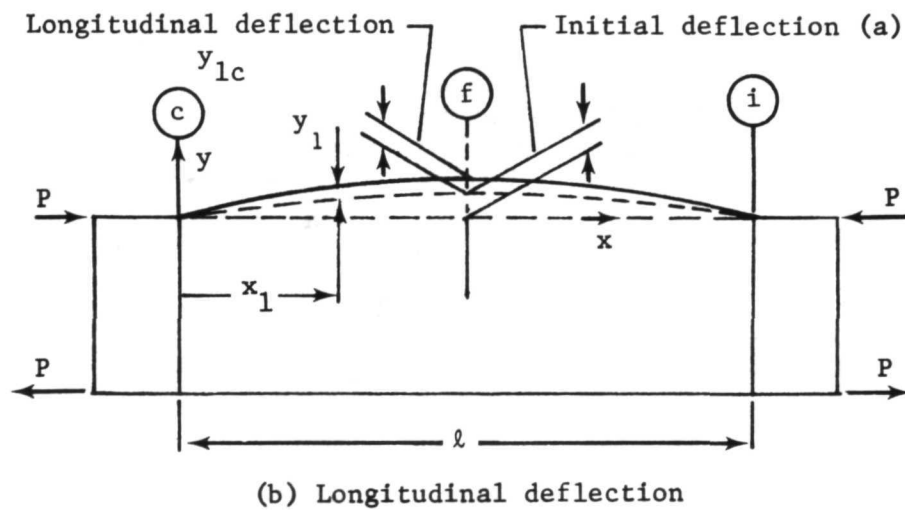
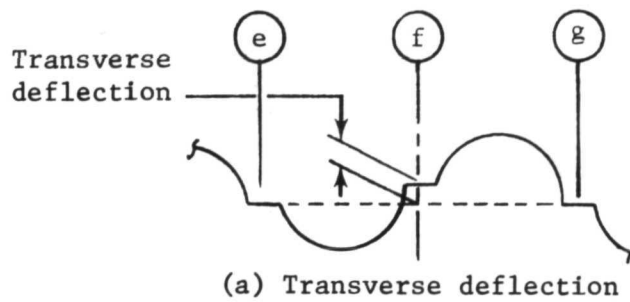


Figure A8 Deflections Measured during Test and Calibration and Southwell Plot

APPENDIX A

The test assembly was heated by the quartz lamp array to 922°K (1200°F). Temperature differences were limited to 311°K (100°F) during heating, test, and cooldown. The massive end caps responded more slowly to heating; therefore, they were used to control the overall heating. During the test, the test panel was maintained at $922 \pm 17^\circ\text{K}$ ($1200 \pm 30^\circ\text{F}$). Edges were somewhat cooler than the center.

The array was divided into nine zones controlled by 130 kVa thermac-Ignition power controllers made by R. I., Inc. Type K chromel-alumel thermocouples, 24 gage, with G/G insulation were mounted at 50 locations. Of these, 43 were used to control and monitor the temperature. Thermocouple output was recorded as temperatures on three Bristol Multipoint strip chart recorders (two 24 channel, one 10 channel).

Heating arrays for the ends of the box, were attached to the load rods to follow the box as it moved during load. It was necessary to cool the load rods by wrapping 0.64 cm ($\frac{1}{4}$ in.) copper tubing and circulating a steady flow of cold water through the tubing.

ELEVATED TEMPERATURE TESTS

Procedure

The test sequence was as follows:

- 1) Heat entire assembly to 922°K (1200°F) average time 1 hr;
- 2) Pressurize box to 5171 N/cm² (0.75 psi) above atmospheric and maintain;
- 3) Apply full torsion load and maintain;
- 4) Apply axial loads (compression on top, tension, on bottom);
- 5) Record panel displacements at each axial load level;
- 6) Plot load deflection data and make Southwell plots;
- 7) Determine maximum axial buckling load;
- 8) Remove loads and cool down.

APPENDIX A

The interior of the test fixture was pressurized with dry nitrogen to 5171 N/m^2 (0.75 psi). The high-temperature sealant helped limit excessive escape of internal pressure.

Shear was introduced in the panel by applying the torsion loads found in the calibration. The test point is given in figure A7. A constant value of 205 N/cm (117 ppi) was maintained during the test.

Compression was applied to the test panel and tension to the NASA panel by the upper and lower axial load rods. The axial panel load in Newtons per centimeter (pounds per inch) was determined by the calibration curves in figure A6. Panels were loaded in several increments and held at load while deflection data were recorded.

Three displacement transducers (e, f, and g) were located at the center of the panel and one at each end (c and i) as shown in figure A8. Due to the interference of the transducers with the support structure for the top lamps, the three center transducers were placed at an angle other than vertical. All data have been corrected for this angle. Quartz rods were used between the heated panel and the core of the deflection transducers to prevent adverse effects of heat.

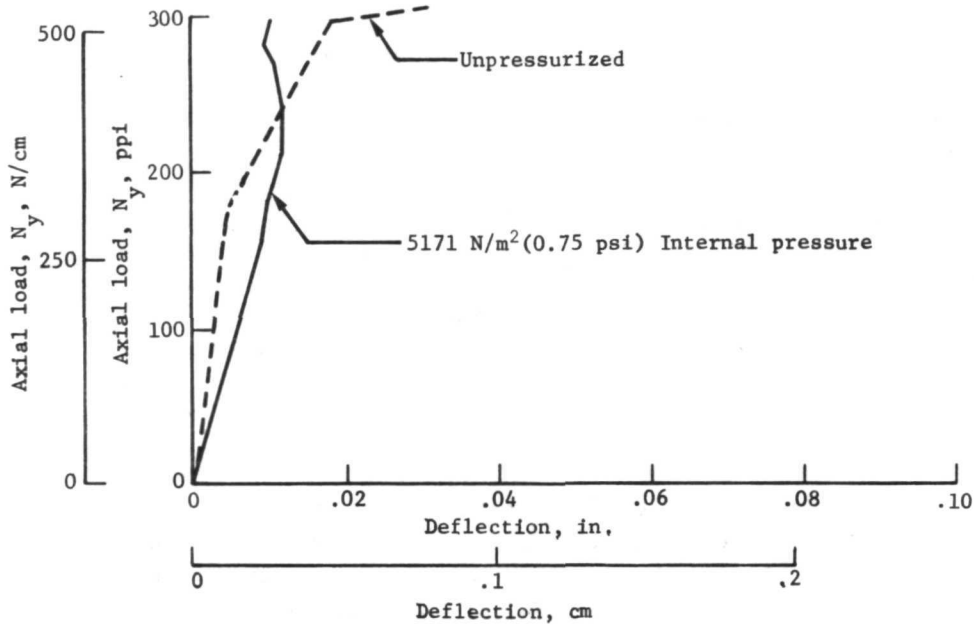
Results

Heated tests with 205 N/cm (117 ppi) shear and 5171 N/m^2 (0.75 psi) internal pressure did not indicate any signs of panel buckling. Load deflection data for Panel 1 under these conditions are shown in figure A9. Initial longitudinal deflection from the 5171 N/m^2 (0.75 psi) pressure was 0.312 cm (0.123 in.) The data show the panel with constant stiffness up to 531 N/cm (303 ppi) axial load.

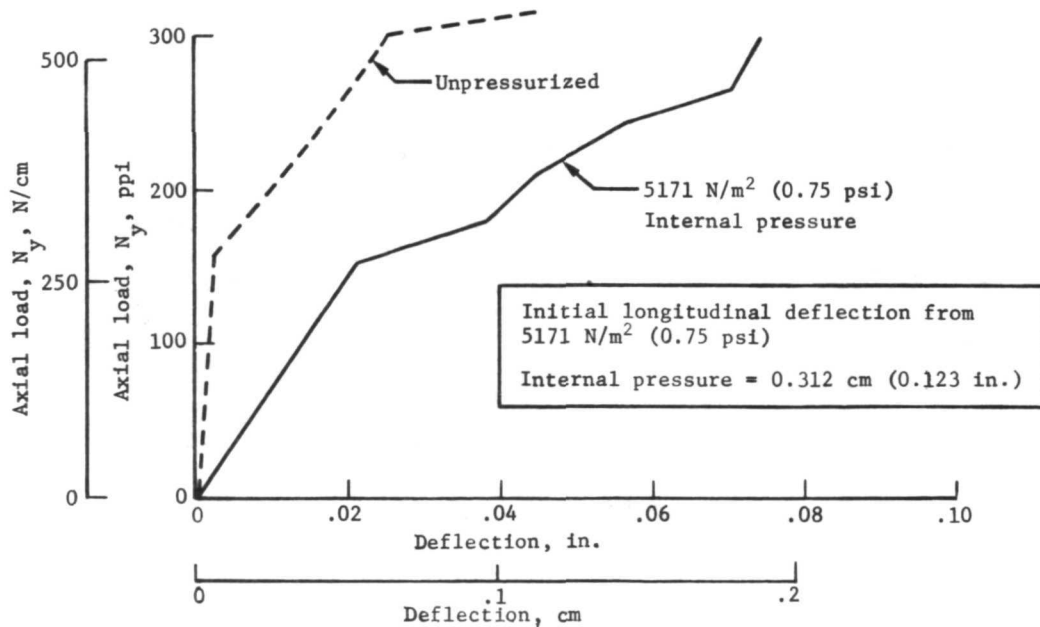
When the same test, for Panel 1, was repeated without internal pressure the load-deflection response was different as shown in figure A9. Loss of stiffness was apparent as load was increased. The test was terminated at 552 N/cm (315 ppi) axial load.

It was concluded that pressure was a stabilizing influence thereby increasing the axial load required for buckling. This effect had been observed earlier and is discussed in reference A2. Analysis of the critical loads did not include the influence of pressure on buckling but did consider pressure as affecting the strength cutoff shown in figure A1.

APPENDIX A



(a) Load-transverse deflection



(b) Load-longitudinal deflection

Figure A9 Load-Deflection for Panel 1

APPENDIX A

Similar data were obtained from the second panel test. Pressurization produced an initial deflection of 0.353 cm (0.139-in.). Load-deflection curves for pressurized Panel 2 are shown in figure A10 and indicate a panel response similar to Panel 1. Response measured for the unpressurized test also was similar to Panel 1.

Southwell Plots for Critical Loads

To avoid the possibility of damaging the test box, the panel tests were planned to provide the critical loads without failing the panels. The technique used to achieve such information was the method of Southwell (ref. A3), which has been used for buckling of orthotropic plates (ref. A4).

The method is based on the nonlinear lateral response of a compression member nearing its critical load. The deflection divided by load is plotted along the ordinate and the deflection along the abscissa as shown in figure A11. The critical load is the inverse of the slope of this line.

Using the notation of figure A8, the basic Southwell deviation is based on the initial deflection and the deflections at the center due to load. Deflection at any point x , due to load is given by

$$y_1 = \frac{\alpha}{1 - \alpha} a \sin \frac{\pi x}{\ell}, \text{ where } \alpha = \frac{P}{P_{cr}}$$

This may be written as

$$y_1 = \frac{P}{P_{cr} - P} a \sin \frac{\pi x}{\ell}$$

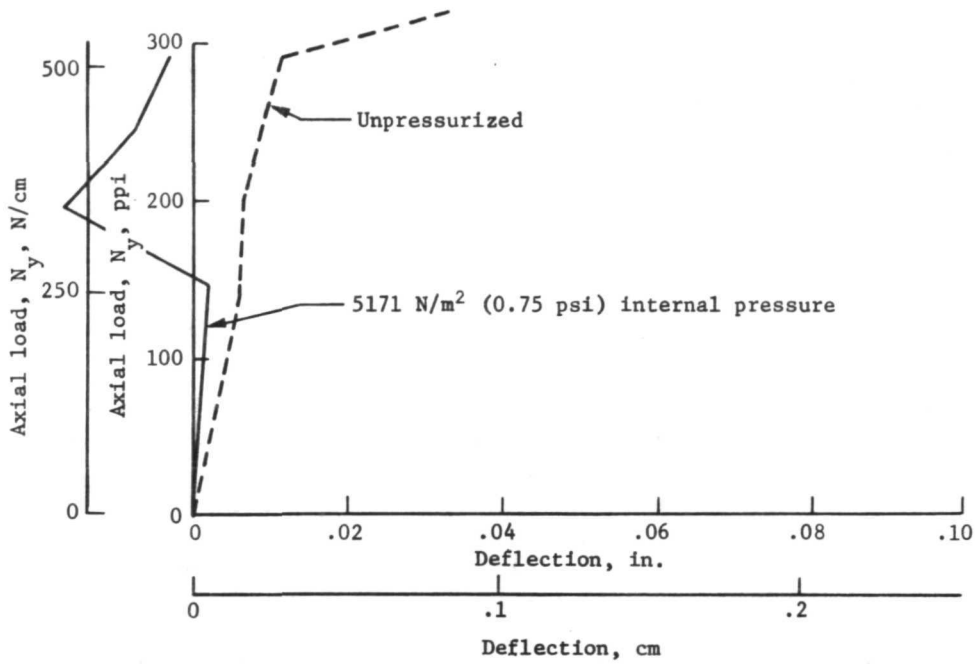
At $x = \frac{\ell}{2}$ this becomes, for the center deflection,

$$y_{1c} = \frac{P}{P_{cr} - P} a$$

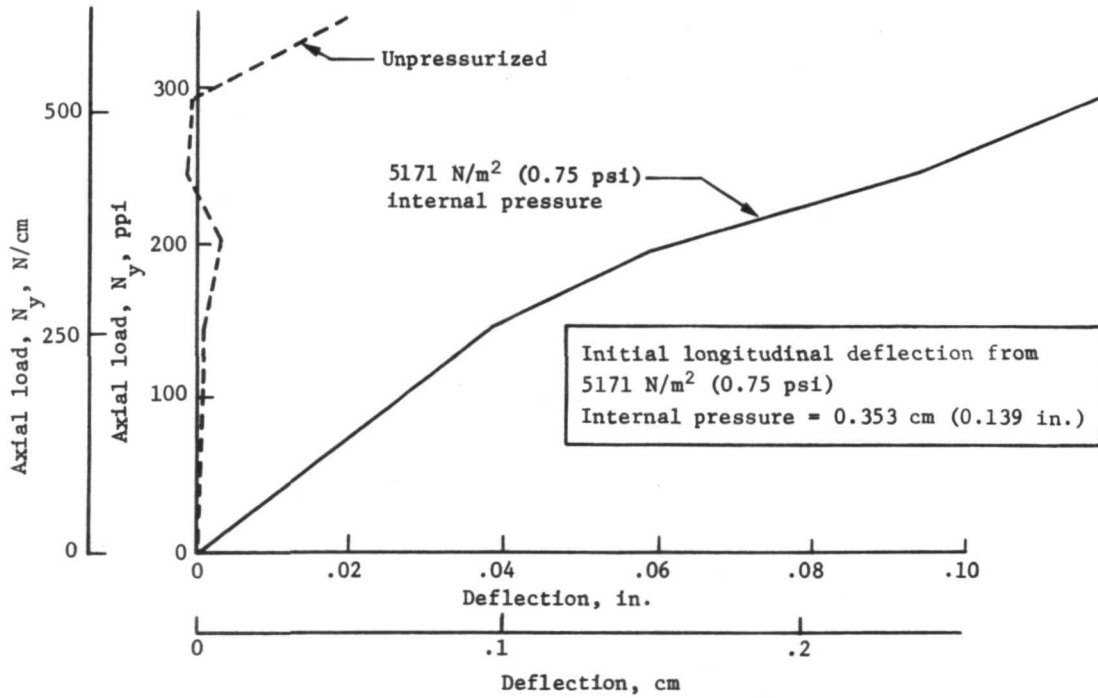
Solving for the critical load, P_{cr} , we have

$$P_{cr} = \frac{a + y_{1c}}{\frac{y_{1c}}{P}}$$

APPENDIX A

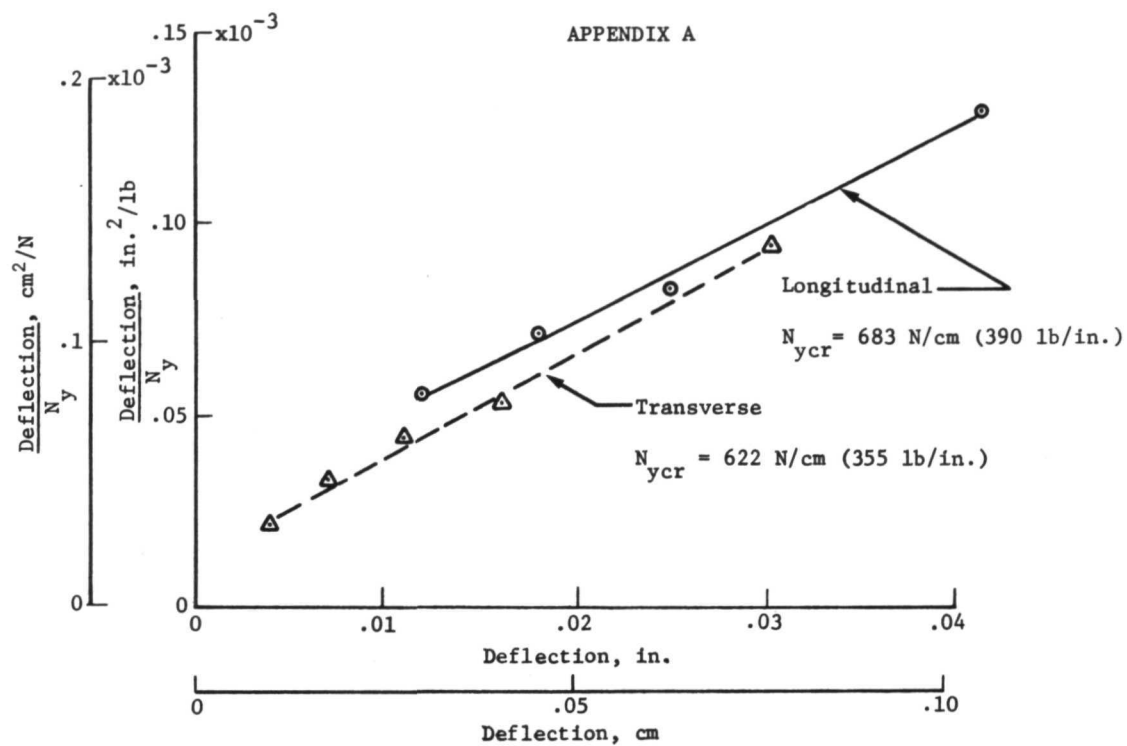


(a) Load-transverse deflection

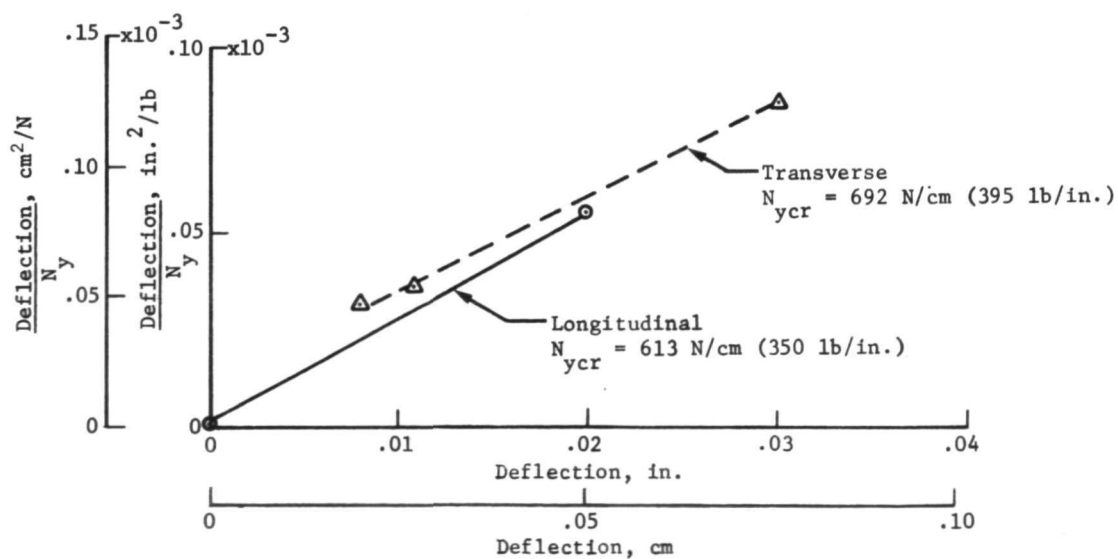


(b) Load-longitudinal deflection

Figure A10 Load-Deflection for Panel 2



(a) Panel 1



(b) Panel 2

Figure A11 Southwell Plots for Critical Loads

APPENDIX A

This defines the inverse slope of the straight line shown in the Southwell plot in figure A8(c).

Both the transverse and longitudinal deflections gave consistent data for critical loads as summarized in table AI. Data taken from pressurized panel tests did not plot as straight lines.

TABLE AI
THEORETICAL AND ACTUAL PANEL LOADS

Panel	Temperature, °K (°F)	Pressure, (psi) N/m ²	Thickness, cm (in.)		Critical load, N/cm (ppi)			Shear, N/cm (ppi)	
			Theo	Act.	Theo	Act. transv	Act. long.	Theo.	Act.
1	922 (1200)	0(0) 0(0)	0.051 (0.020)	0.048 (0.019)	613 (350)	622 (355)	683 (390)	205 (117)	205 (117)
2	922 (1200)	0(0) 0(0)	0.051 (0.020)	0.051 (0.020)	613 (350)	692 (395)	613 (350)	205 (117)	205 (117)

APPENDIX B

JOINT TESTS

CAP SHEAR AND COMPRESSION

To verify the design and fabrication procedure of welding caps to webs, a series of shear and compression tests was conducted. This construction was typical of all the ribs and spars. Tests were performed at room temperature and at 922°K (1200°F). Half of the specimens underwent a thermal soak of 1033°K (1400°F) for 15 hr before testing. This was included to determine whether thermal exposure affected the strength properties of the welded joints.

Figure B1 shows the details of the specimens. They were tested in a 667 000-N (150 000-lb) BLH universal hydraulic testing machine. Elevated tests were conducted at 1033°K (1400°F) using quartz lamps to heat the specimens. Test results are summarized in table B1.

TABLE B1
ULTIMATE SHEAR AND COMPRESSION LOADS, N (lb) ON CAPS

Test	With elevated temperature soak		Without elevated temperature soak	
	Room temperature	1033°K (1400°F)	Room temperature	1033°K (1400°F)
Shear	8 007 (1 800)	7 117 (1 600)	8 007 (1 800)	5 783 (1 300)
Compression	22 241 (5 000)	13 789 (3 100)	22 241 (5 000)	10 231 (2 300)

The 10 231-N (2300-lb) test point at 1033°K (1400°F) for compression of a cap has been used to design the caps by modifying the design equations. Deformations were measured during the tests. Response at room temperature and 1033°K (1400°F) was similar; however, the elevated temperature ultimate loads were lower. The differences in strength between room temperature and the 1033°K (1400°F) environment is apparent. There appears to be some benefit from having undergone a thermal soak for the elevated temperature tests, however, the data are too limited for a definite conclusion.



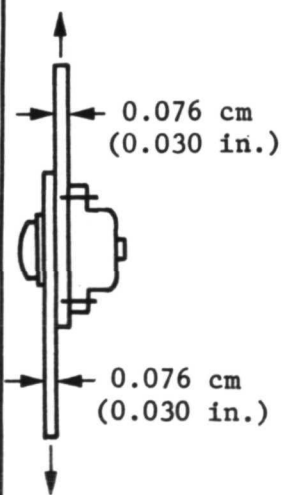
Note: Dimensions in cm (in.)

APPENDIX B

PANEL TO SPAR CAP

Single shear tests were performed on a screw connection representing the edge of the structural panel and a spar cap. Preliminary designs established the spar cap and panel thicknesses as 0.076 cm (0.030 in.), therefore, the tests were performed with these gages. Half of the tests were at room temperature and the other half were at 1033°K (1400°F). In addition, half of all specimens were subjected to a thermal soak of 1033°K (1400°F) for 15 hr. Table BII summarizes the test results and lists margins of safety for ultimate loads.

TABLE BII
ULTIMATE MARGIN OF SAFETY FOR PANEL TO SPAR CAP

	Test temperature	Spec soak	Test load, N (lb)		Ultimate	
			Yld	Ult	Design, N/screw (lb/screw)	MS
	RT	No	8229 (1850)	10 943 (2 460)	1432 (322)	6.6
	RT	No	8563 (1925)	11 490 (2 583)	1432 (322)	7.0
	RT	Yes	8118 (1825)	11 232 (2 525)	1432 (322)	6.8
	RT	Yes	8118 (1825)	10 840 (2 437)	1432 (322)	6.5
	1033°K (1400°F)	No	4448 (1000)	6 939 (1 560)	1432 (322)	3.8
	1033°K (1400°F)	No	4448 (1000)	6 917 (1 555)	1432 (322)	3.8
	1033°K (1400°F)	Yes	5004 (1125)	7006 (1 575)	1432 (322)	3.9
	1033°K (1400°F)	Yes	5115 (1150)	6 895 (1 550)	1432 (322)	3.8

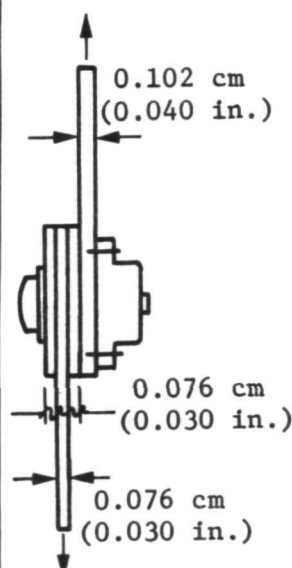
APPENDIX B

Lowest margin of safety on the ultimate load is 3.8 at 1033°K (1400°F). In the test structure the spar cap and panel are built of 0.094 cm (0.037 in.) material and the screws and nuts are (10-32) Waspaloy with René 41 nut retainers as identified in the design drawings.

PANEL TO RIB CAP

Panels were fastened to rib caps with (No. 10) screws. Tests were conducted on a multilayer specimen representing the rib cap and panel with upper and lower doublers. Initial designs indicated a rib cap thickness of 0.102 cm (0.040 in.) with panel and doublers 0.076 cm (0.030 in.) thick. The doublers were spot welded to the panel material to represent panel construction. The final design was modified to put the fasteners in double shear. This is reflected in the ultimate design loads of table BIII. This table lists the test results and ultimate margins of safety.

TABLE BIII
ULTIMATE MARGIN OF SAFETY FOR PANEL TO RIB CAP

	Test temperature	Spec soak	Test Load, N (lb)		Ultimate	
			Yld	Ult	Design, N/screw (lb/screw)	MS
	RT	No	8616 (1937)	11 232 (2 525)	4092 (982)	1.7
	RT	No	9119 (2050)	10 675 (2 400)	4092 (920)	1.6
	RT	Yes	7340 (1650)	10 765 (2420)	4092 (920)	1.6
	RT	Yes	8007 (1800)	10 587 (2 380)	4092 (920)	1.6
	1033°K (1400°F)	No	5338 (1200)	7 028 (1 580)	4092 (920)	.7
	1033°K (1400°F)	No	6116 (1375)	7 304 (1 642)	4092 (920)	.8
	1033°K (1400°F)	Yes	6228 (1400)	7 562 (1 700)	4092 (920)	.8
	1033°K (1400°F)	Yes	6116 (1375)	7 562 (1 700)	4092 (920)	.8

APPENDIX B

The sketch in table BIII shows the screw in single shear whereas the wing test structure uses a splice strap at the ribs to put the screws in double shear. The design load per screw is adjusted to single shear. Lowest margin of safety is shown to be 0.7. For the test structure the rib caps, panels, and doublers are all made of 0.094 cm (0.037 in.) René 41 nut retainers.

HEAT SHIELD CLIPS

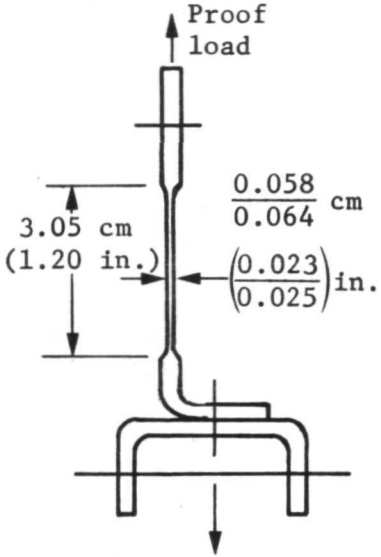
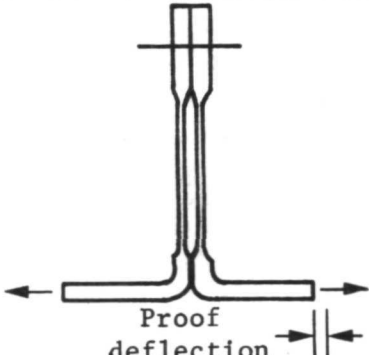
Heat shield clips were tested for the René 41 and TDNiCr heat shields to verify the strength and flexibility of the clips. Materials were the same for the clip and shield.

For René 41 the clips were Z sections with four clips per panel, each panel being approximately 50.8x43.2 cm (20x17 in.). Tension and flexure tests were performed at proof loads that were twice limit loads, and proof deflections at twice the calculated deflections. Tests on material aged at 1033°K (1400°F) for 16 hr were made at room temperature and elevated temperature. Axial load was applied at 1144°K (1600°F) and flexure at 700°K (800°F), the former to test material yielding and the latter to test clip stiffness. Table BIV is a schematic of the clip and the test arrangement. The clip was 3.81 cm (1½ in.) wide. Half of the specimens underwent a thermal soak of 1144°K (1600°F) for 16 hr. After testing, there was no permanent deformation from either the proof load or the proof deflection.

Clips of TDNiCr were made as hat sections. The TDNiCr heat shield design had three support beams; therefore, six clips (two per support beam). Tension and flexure tests on the 3.175-cm (1¼-in.) wide clips were at proof loads and deflections, defined as twice the limit values. Room temperature and elevated temperature tests were performed to verify strength and flexibility of the design. Table BV summarizes the tests at room temperature and elevated temperatures. The thermal soak, for half the specimens before test, was at 1366°K (2000°F) for 15 hr. Results of the tests showed no permanent deformations.

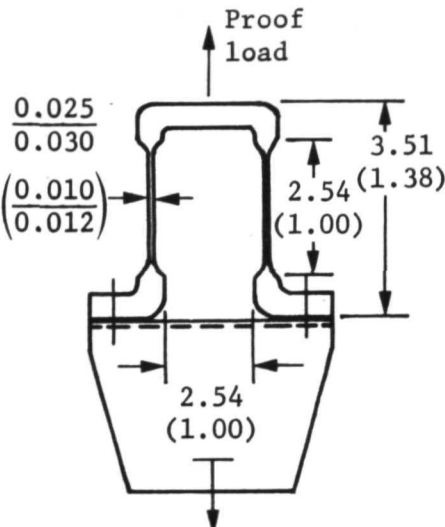
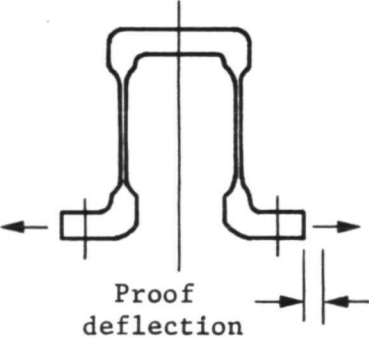
APPENDIX B

TABLE BIV
PROOF LOAD AND FLEXURE TESTS, RENÉ 41 HEAT SHIELD CLIPS

	Test temperature	Spec soak	Load, N (lb)	Deflection, cm (in.)
	RT	No	552 (124)	--
	RT	No	552 (124)	--
	RT	Yes	552 (124)	--
	RT	Yes	552 (124)	--
	1144°K (1600°F)	No	552 (124)	--
	1144°K (1600°F)	No	552 (124)	--
	1144°K (1600°F)	Yes	552 (124)	--
	1144°K (1600°F)	Yes	552 (124)	--
	RT	No	18.7 (4.2)	0.178 (0.07)
	RT	Yes	22.7 (5.1)	0.178 (0.07)
	700°K (800°F)	No	11.1 (2.5)	0.254 (0.10)
	700°K (800°F)	Yes	5.8 (1.3)	0.254 (0.10)

APPENDIX B

TABLE BV
PROOF LOADS AND FLEXURE TESTS, TDNiCr HEAT SHIELD CLIPS

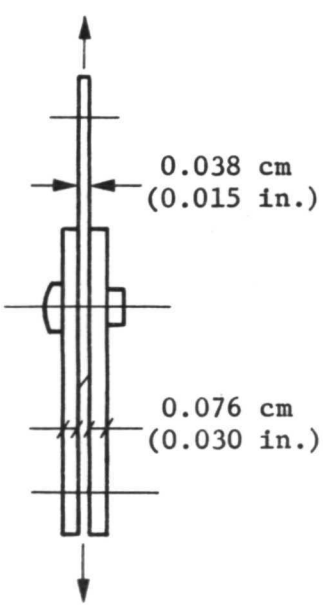
 <p>Dimensions in cm (in.)</p>	Test temperature	Spec soak	Load, N (lb)	Deflection, cm (in.)
	RT	No	334 (75)	--
	RT	No	334 (75)	--
	RT	Yes	334 (75)	--
	RT	Yes	334 (75)	--
	1366°K (2000°F)	No	334 (75)	--
	1366°K (2000°F)	No	334 (75)	--
	1366°K (2000°F)	Yes	334 (75)	--
 <p>Proof deflection</p>	RT	No	12.14 (2.73)	0.254 (0.100)
	RT	No	18.59 (4.18)	0.254 (0.100)
	RT	Yes	11.79 (2.65)	0.254 (0.100)
	RT	Yes	10.81 (2.43)	0.254 (0.100)
	727°K (850°F)	No	35.59 (8.00)	0.386 (0.152)
	727°K (850°F)	No	17.13 (3.85)	0.386 (0.152)
	727°K (850°F)	Yes	20.02 (4.50)	0.386 (0.152)
	727°K (850°F)	Yes	17.13 (3.85)	0.386 (0.152)

APPENDIX B

WEB TO WEB

Webs at each rib and spar intersection were connected with four angles thereby putting the fasteners in double shear. A series of test was conducted on a riveted connection at room temperature and at 1033°K (1400°F). The soak cycle for half of the specimens was 15 hr at 1033°K (1400°F). Before riveting, with 0.239-cm (3/32-in.) diameter HS 188 rivets, the René 41 material was aged for 16 hr. Table BVI summarizes the results of the tests.

TABLE BVI
ULTIMATE MARGIN OF SAFETY FOR WEB TO WEB CONNECTION

	Test temperature	Spec soak	Ultimate		
			Load, N (lb)	Design, N/screw (lb/screw)	MS
	RT	No	5605 (1260)	1690 (380)	2.31
	RT	No	4626 (1040)	1690 (380)	1.74
	RT	Yes	4849 (1090)	1690 (380)	1.86
	RT	Yes	5115 (1150)	1690 (380)	2.00
	1033°K (1400°F)	No	3492 (785)	1690 (380)	1.06
	1033°K (1400°F)	No	3114 (700)	1690 (380)	.84
	1033°K (1400°F)	Yes	3336 (750)	1690 (380)	.97
	1033°K (1400°F)	Yes	--	1690 (380)	--

In the wing test structure the web at the intersection was 0.048 cm (0.019 in.) thick and the angles were 0.076 cm (0.030 in.) thick. The maximum ultimate load occurred in a spar web at FS 2311.4 cm (910 in.) at BL 137.16 cm (54 in.). The rivets in the wing test structure are HS 188 and the angles are René 41.

APPENDIX B

TENSION ACROSS WELDS

Spanwise loads from structural panels were carried across the rib caps. The rib caps are welded to the rib webs, therefore, the spanwise loads from panel to panel are carried across a melt-through weld. On the test structure a splice strap is placed over the panel to put the fastener in double shear so that the load in the rib cap is half of the joint load.

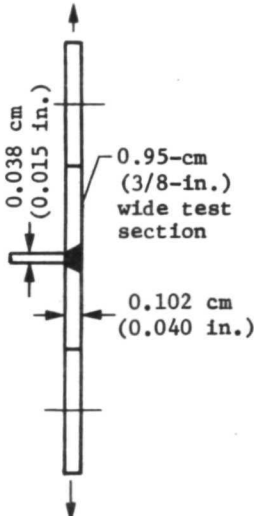
Tests were conducted on specimens made with and without filler wire in the weld. A standard tensile specimen was used to represent the cap and a T piece was welded across at the center to represent the web.

Table BVII is a summary of the test results. Specimens were welded in the annealed condition, reannealed, and aged before test. Half of the specimens were exposed to a thermal soak of 1033°K (1400°F) before testing.

For the wing test structure the cap material was 0.093 cm (0.037 in.) René 41 and the web was 0.041 cm (0.016 in.) thick. Because of the similar results found from specimens with and without filler wire, the decision was made to weld the caps to the webs using a meltthrough weld without filler wire.

APPENDIX B

TABLE BVII
ULTIMATE MARGIN OF SAFETY FOR TENSION ACROSS WELDS

	Test temperature	Spec soak	Filler wire	Test load, MN/m ² (ksi)		Ultimate	
				Yld	Ult	Design, MN/m ² (ksi)	MS
	RT	No	No	1034 (150)	1255 (182)	101 (14.6)	11.4
	RT	No	No	1034 (150)	1248 (181)	101 (14.6)	11.4
	RT	Yes	No	1062 (154)	1151 (167)	101 (14.6)	10.4
	RT	Yes	No	1041 (151)	1276 (185)	101 (14.6)	11.6
	RT	No	Yes	993 (144)	1200 (174)	101 (14.6)	10.9
	RT	No	Yes	972 (141)	1282 (186)	101 (14.6)	11.7
	RT	Yes	Yes	993 (144)	1193 (173)	101 (14.6)	10.8
	RT	Yes	Yes	965 (140)	1117 (162)	101 (14.6)	10.1
	1033°K (1400°F)	No	No	758 (110)	889 (129)	101 (14.6)	7.8
	1033°K (1400°F)	No	No	745 (108)	876 (127)	101 (14.6)	7.7
	1033°K (1400°F)	Yes	No	758 (110)	869 (126)	101 (14.6)	7.6
	1033°K (1400°F)	Yes	No	752 (109)	807 (117)	101 (14.6)	7.0
	1033°K (1400°F)	No	Yes	--	889 (129)	101 (14.6)	7.8
	1033°K (1400°F)	No	Yes	--	648 (94)	101 (14.6)	5.4
	1033°K (1400°F)	Yes	Yes	--	841 (122)	101 (14.6)	7.3
	1033°K (1400°F)	Yes	Yes	--	745 (108)	101 (14.6)	6.4

APPENDIX C

FORMING ORTHOTROPIC PANELS*

An analysis of stresses and deflections occurring during the forming of circular arc stiffeners in orthotropic panels is presented. The HYDRO-MAR-BEADING method of forming the stiffened panels is described.

Figure C1 depicts the pressure forming procedure. As the pressure opposite the circular cavity is increased, the sheet metal bends and stretches into the cylindrical cavity. For the design configuration, the circular beads are alternately on opposite sides of the sheet. A clamping force is applied to minimize leakage of the pressurized forming fluid. The air behind the bead is bled out of the cavity as shown in the figure.

Some of the panels were successfully formed in one application of pressure. Others required several operations with intermediate annealing. Some of the panels failed during forming, due to insufficient ductility. The failures generally occurred at the small radius at the end of the arc. There was local thinning of several thousandths of an inch at this point. The combined effects of the relatively sharp local bending and the overall plastic stretching caused strain concentrations and local thinning.

The sheets that were formed were annealed René 41. Several panels of 304 stainless steel were formed for checkout. Three different panel configurations--7, 8, and 10 beads--were formed.

*This work was conducted under IRAD Task Study D-54D and is reported in "Metallic Heat Shield Engineering and Manufacturing Development Final Report," D73-48714-001, April 1973, by H. H. Hotchkiss (ref. C1).

APPENDIX C

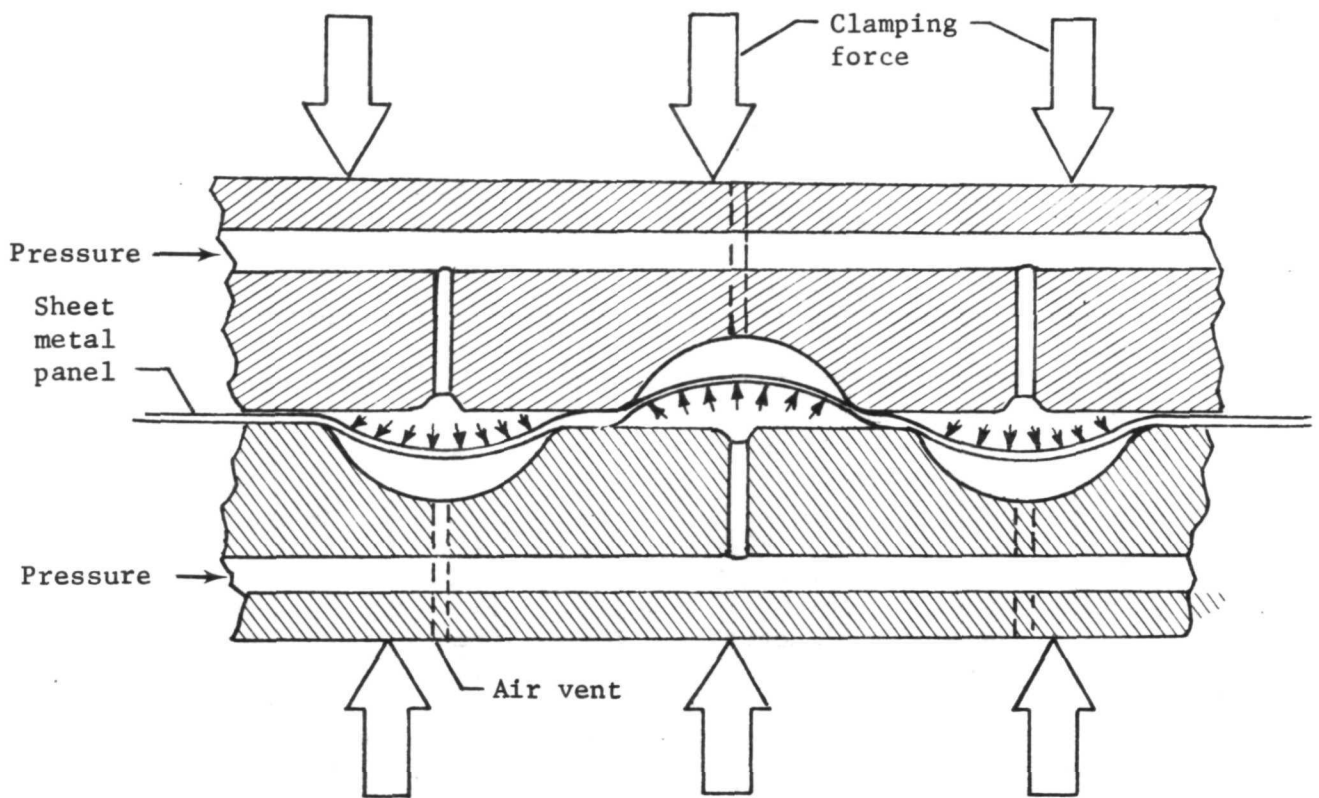


Figure C1 Pressure Forming Beaded Panel

LIST OF SYMBOLS

b	half of chord of arc
d	depth of partially formed bead
d_f	full depth of bead
l	length after straining
l_o	initial length
p	forming pressure
R	radius of partially formed bead

APPENDIX C

R_f	radius of fully formed bead
t	thickness of bead
t_o	thickness before forming
ϵ	strain
θ	half-angle of partially formed bead
θ_f	half-angle of fully formed bead
σ	stress

The analysis provides a method for predicting the pressures required for forming. The equations are to be used with a stress-strain curve, the final bead radius, depth, and metal thickness.

The method assumes that uniform thinning occurs in the pressure-formed circular arcs. This relates the radius, width of bead, initial thickness, and depth of bead to the strain in the formed beads. The equilibrium relationship is the tangential force and radial pressure in a thin circular cylinder.

The geometries of the undeformed sheet metal, the partially formed bead, and the fully deformed bead are shown in figure C2.

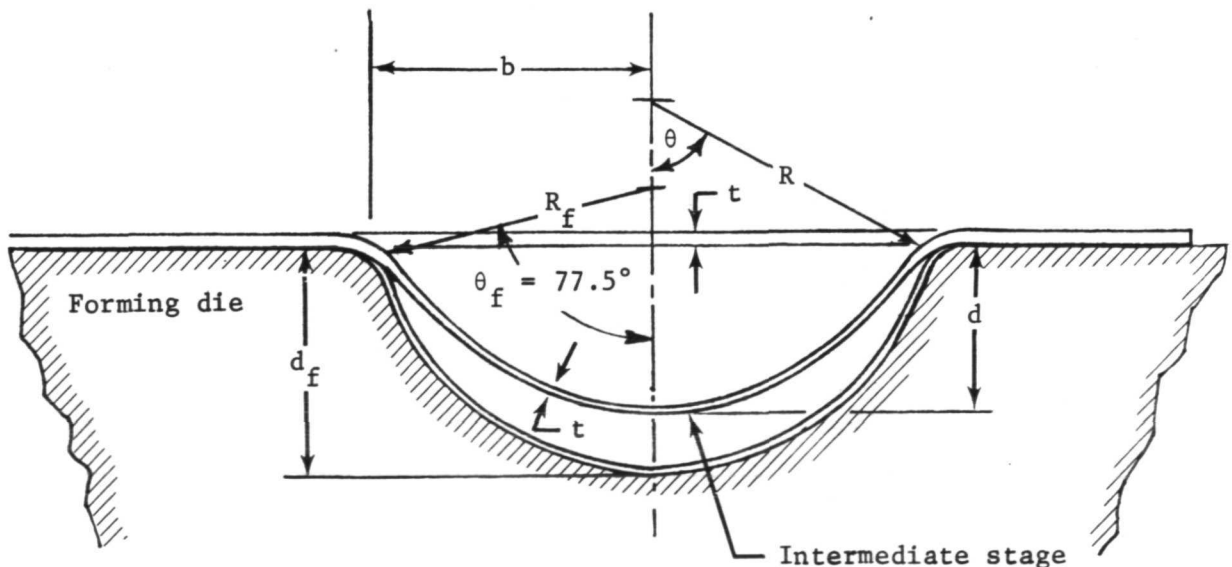


Figure C2 Geometry of Forming Die and the Sheet

APPENDIX C

Tangential stress in the circular arc is assumed to be constant around the arc and related to the forming pressure according to the thin-wall membrane equilibrium expression

$$\sigma = p \frac{R}{t} \quad (C1)$$

The radius and the thickness of the bead decrease as the pressure and the depth of forming increase. The initial inelastic deformations and stresses are for a uniformly loaded, clamped flat plate. As deflections become large, the membrane action proceeds with increasing pressure. The metal becomes thinner and the bead depth approaches the full depth of the die, as shown in figure C2.

The strain in the circular arc is related to the initial thickness and to the reduced thickness by assuming that the volume of the metal is constant regardless of the amount of straining. The strain is expressed as

$$\epsilon = \frac{t_o}{t} - 1 \quad (C2)$$

Ratios $\frac{R}{t}$ and $\frac{t_o}{t}$ are obtained for equations (C1) and (C2) by the following relationships between the variables shown in figure (C2).

$$R = \frac{b^2 + d^2}{2d} \quad (C3)$$

The condition of constant volume provides the relationship between the initial thickness and the formed thickness, so that from equation (C3) we have

$$\frac{t}{t_o} = \frac{b}{R\theta} = \frac{2bd}{(b^2 + d^2) \sin^{-1} \left(\frac{2bd}{b^2 + d^2} \right)} \quad (C4)$$

The expression for $\frac{R}{t}$ is obtained from equations (C3) and (C4) as

$$\frac{R}{t} = \frac{(b^2 + d^2)^2 \sin^{-1} \left(\frac{2bd}{b^2 + d^2} \right)}{4t_o b d^2} \quad (C5)$$

APPENDIX C

The equation for strain results from the combination of equations (C2) and (C4), and is

$$\epsilon = \frac{(b^2 + d^2) \sin^{-1} \left(\frac{2bd}{b^2 + d^2} \right)}{2bd} - 1 \quad (C6)$$

True stress is calculated in terms of measured values of t_o , b , d , and pressure by means of the equilibrium equation (C1) and $\frac{R}{t}$ from equation (C5) as

$$\sigma = p \left\{ \frac{(b^2 + d^2)^2 \sin^{-1} \left(\frac{2bd}{b^2 + d^2} \right)}{4t_o b d^2} \right\} \quad (C7)$$

Figure C3 is constructed from values of stress and strain calculated from the measured geometric and pressure quantities in equations (C6) and (C7). Data from more than 50 points define three areas of forming. One area shows partial forming of as-received (annealed condition) René 41. Another area shows failed panels resulting from one step forming of as-received material. The third area is the final forming of partially formed panels after they had been reannealed to remove the effects of strain-hardening.

Some bead geometries and panel thicknesses in different dies having the same half angle of 77.5° were formed full depth without need for an intermediate anneal, and others required annealing, as shown in figure C3.

Stresses calculated by equation (C7) are true stresses based on the actual reduced thickness. The strain as calculated by equation (C6) is the conventional strain based on comparison of the final to the initial thickness or length. The procedure used in converting from conventional stress to true stress is given by Nadai (ref. C2).

$$\text{True Stress} = (1 + \epsilon) \times \text{Conventional Stress} \quad (C8)$$

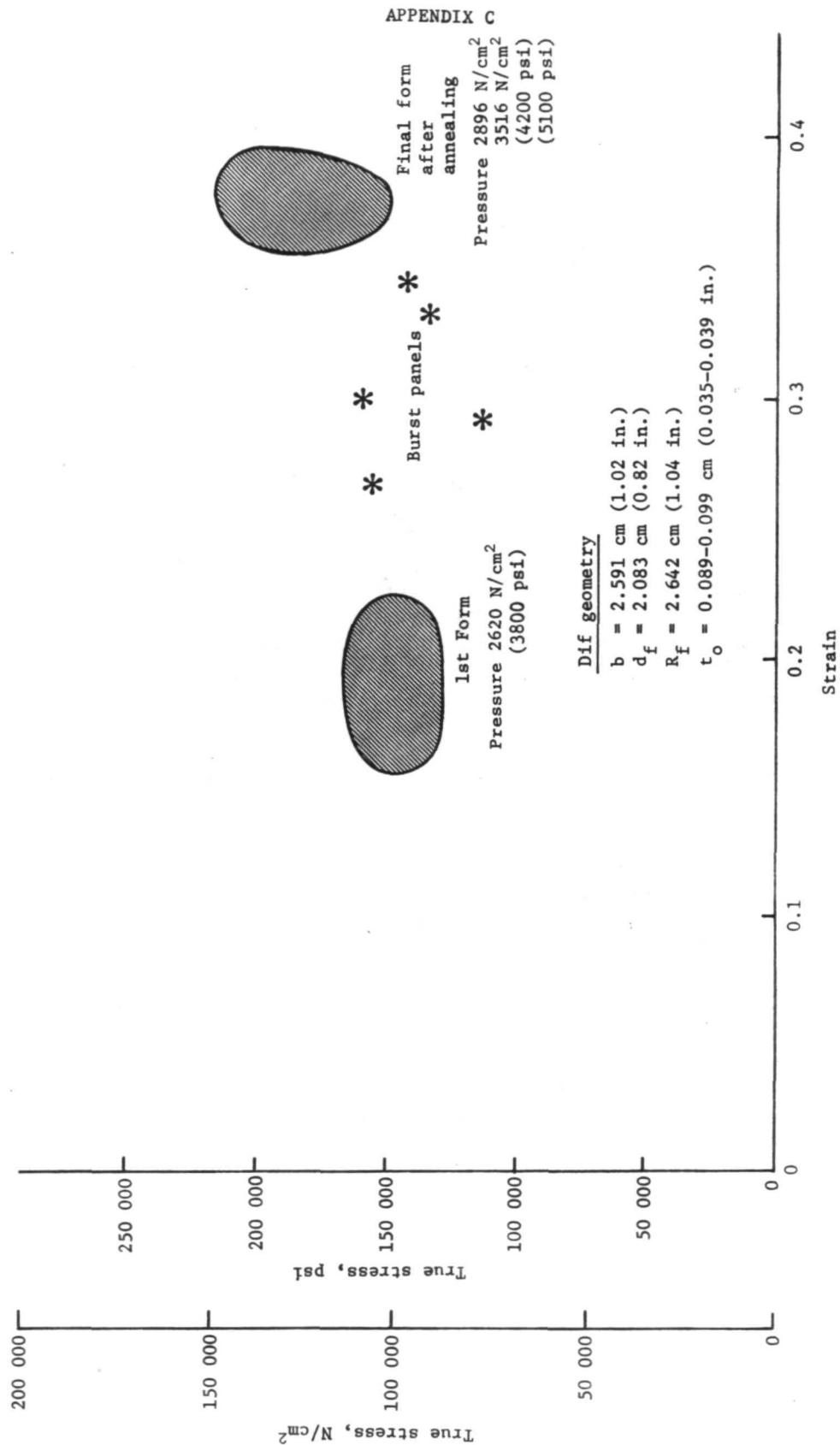


Figure C3 Calculated Stress versus Strain, Seven-Bead Annealed René 41 Panels

APPENDIX C

These procedures can be used as a means of predicting the pressure required for the formation of beads of specified radii and depth from sheet metals of various initial thicknesses. The following steps are suggested:

- 1) Plot true stress versus strain by use of equation (C8) from conventional stress-strain data for annealed material;
- 2) Calculate the strains for the selected bead configuration, by means of equation (C6);
- 3) Select the true stress, corresponding to the calculated strain, from the true stress-strain curve;
- 4) Calculate the required pressure from equation (C7).

Where stress-strain data are available, the results of the predictions should be compared with the actual results. Such comparisons will provide a measurement of the validity of this method and will suggest any need for improvement.

APPENDIX D

NEW TECHNOLOGY

New Technology Disclosures submitted under Contract NAS4-1845:

<u>Report No.</u>	<u>Title</u>	<u>Innovators</u>
286	Calculation of Effective Mechanical Properties of Beaded Panels	D. H. Seitz
396	Cast in Place Inserts to Make Variable Die Configurations for Beaded Panels	F. A. Penning
400	Computer Program (OPTBEAD) for Optimum Design	H. Hotchkiss D. H. Seitz
401	Modification of Computer Program for the Design of Beaded Panels, to Provide Interaction Curves for Combined Loading	M. O. Dressel
405	Porta Punch	W. P. Coppfer
406	Sine Wave Web Forming of Superalloy Rene' 41	M. D. Howard

REFERENCES

1. Plank, P. P.; et al: Hypersonic Cruise Vehicle Wing Structure Evaluation. NASA CR-1568, May 1970.
2. Plank, P. P.; et al.: Substantiation Data for Hypersonic Cruise Vehicle Wing Structure Evaluation. NASA CR-66897 (Vols. I through III), February 1970.
3. Anon.: Military Standardization Handbook, Metallic Materials and Elements for Aerospace Vehicle Structures. MIL-HDBK-5B, Department of Defense, September 1, 1971.
4. Davis, J. W.: Advanced Design Bulletin. M&P 100, McDonnell Douglas Astronautics Company, July 1970.
5. Anon.: René 41 Technical Bulletin. Cann-Muskegon Corporation.
6. Anon.: Thermal Insulation. Technical Bulletins, Johns-Manville Aerospace Products.
7. Schmitt, D. A.: Users Manual for FD330 Aerodynamic Heating Program. T-70-48871-003, Martin Marietta Corporation, Denver, Colorado, December 1970.
8. Anon.: Aerodynamic and Rocket-Exhaust Heating during Launch and Ascent, NASA Space Vehicle Design Criteria (Structures). NASA SP-8029, May 1969.
9. Anon.: Thermal Panel Report to the Aerothermodynamic/Configurations Working Group - Heat Transfer Methodology for Space Shuttle Studies (Preliminary). May 1971.
10. Bertram, M. H.; and Everhart, P. E.: An Experimental Study of the Pressure and Heat-Transfer Distribution on a 70° Sweep Slab Delta Wing in Hypersonic Flow. NASA TR R-153, 1963.
11. Munary, W. M., Jr.; and Stallings, R. L., Jr.: Heat Transfer and Pressure Distributions on 60° and 70° Swept Delta Wings Having Turbulent Boundary Layers. NASA TN D-3644, October 1966.
12. Anon.: Analytical Methods in Aircraft Aerodynamics. NASA SP-228, 1970.

13. Whitehead, A. H., Jr.; and Dunavant, J. C.: A Study of Pressure and Heat Transfer Over an 80° Sweep Slab Delta Wing in Hypersonic Flow. NASA TN D-2708, March 1965.
14. Hanner, O. M., Jr.: Heat Transfer Data Analysis of LRC Thermal Mapping Test Ascent Configurations. IM-I-MMC-AERO-5014, Martin Marietta Corporation, Denver, Colorado, March 26, 1971.
15. Brogan, D. A.; and Guard, F. L.: Substantiation Data for Hypersonic Cruise Vehicle-Wing Structural Evaluation (Vol. 1). NASA CR-66897-1, February 15, 1970.
16. Banner, R. D.; Kuhl, A. E.; and Quinn, R. D.: Preliminary Results of Aerodynamic Heating Studies on the X-15 Airplane. NASA TM X-638, March 1962.
17. Nagel, A. L.; et al.: Investigation of Boundary Layer Transition in Hypersonic Flow at Angle of Attack. AFFDL-TR-122, August 1966.
18. Masaki, M.; and Yakura, J.: Transitional Boundary Layer Considerations for the Heating Analysis of Lifting Reentry Vehicles. AIAA Paper 68-1155, 1968.
19. Anon.: SAE Aerospace Thermodynamics Manual, Society of Automotive Engineers, Inc., Committee A-9, Aerospace Environmental Control Systems, February 1960.
20. Lemley, C. E.: Design Criteria for the Prediction and Prevention of Panel Flutter (Vols. I and II). AFFDL-TR-67-140, August 1968.
21. Bohon, H. L.; Anderson, M. S.; and Heard, W. L., Jr.: Flutter Design of Stiffened-Skin Panels for Hypersonic Aircraft. NASA TN D-555, December 1969.
22. Bohon, H. L.; and Anderson, M. S.: Role of Boundary Conditions on Flutter of Orthotropic Panels. AIAA J., Vol. 4, No. 7, July 1966.
23. Bohon, H. L.; and Shove, C. P.: Application of Recent Panel Flutter Research to the Space Shuttle, Part II - Influence of Edgeclips and Flow Vngularity. NASA TM X-2274, Vol. III, April 1971.

- A1. Hetenyi, M.: Handbook of Experimental Stress Analysis. John Wiley & Sons, Inc., 1950.
- A2. Gerard, G.; and Becker, H.: Handbook of Structural Stability, Part I - Buckling of Flat Plates. NACA TN 3781, July 1957.
- A3. Southwell, R. V.: On the Analysis of Experimental Observations of Elastic Stability. Proc. Roy. Soc. (London), Series A, sol. 135, 1932, pp. 601-616.
- A4. Kicher, T. P.; and Mandell, J. F.: A Study of the Buckling of Laminated Composite Plates. AIAA J., Vol. 9, No. 4, April 1971, pp. 605-613.
- C1. Hotchkiss, H. H.: Heat Shield Engineering and Manufacturing Development, Final Report. D73-48714-001, Martin Marietta Corporation, Denver, Colorado, April 1973.
- C2. Nadai, A.: Theory of Flow and Fracture of Solids (Second Edition). McGraw-Hill Book Company, Inc., 1950.